Centro de Investigación y de Estudios Avanzados del Instituto Politécnico Nacional

Departamento de Física Aplicada

"Procesos de Transporte de Carga y Recombinación en Celdas Solares Sensibilizadas con Tinte: Estudio a partir de Técnicas de Estado Estacionario y de Pequeña Perturbación."

Tesis que presenta

M. en C. Rodrigo García Rodríguez

Para obtener el grado de

Doctor en Ciencias

en Fisicoquímica

Director de tesis: Dr. Gerko Oskam

Mérida, Yucatán, México. Octubre 2016.

Centro de Investigación y de Estudios Avanzados del Instituto Politécnico Nacional

Applied Physics Department

"Charge Transport and Recombination Processes in Dye-Sensitized Solar Cells: Insight from Steady-State and Small Perturbation Techniques"

Thesis presented by

M. Sc. Rodrigo García Rodríguez

To obtain the degree of

Doctor of Science

in Physical Chemistry

Thesis Director: Dr. Gerko Oskam

Mérida, Yucatán, México. October 2016.

Agradecimientos

A Dios, antes que nadie, por permitirme llevar una vida plena, llena de aprendizaje.

A mis padres, por ser mi motivación, mi ejemplo y mi orgullo. A ustedes, más que a nadie, dedico este trabajo.

A mi hermano José Luis, por ser un ejemplo de superación, de empeño y dedicación.

A mi hermano Raúl, por seguir cuidando de mí todavía.

A Karen, por todo su amor, paciencia y comprensión.

A toda mi familia y amigos, por todo el apoyo, el cariño y la motivación.

A todo el grupo de nanomateriales del CINVESTAV Mérida, por las amistades y el aprendizaje que he encontrado ahí.

Al Dr. Gerrit Boschloo, de la Universidad de Uppsala y a todo su grupo de investigación, quienes me brindaron mucho aprendizaje, apoyo y también amistad.

A los doctores Juan Anta y Julio Villanueva, de quiénes he aprendido mucho y siempre han mostrado la mejor disposición y la más profunda paciencia para enseñar.

A mis sinodales, Dr. Juan José Alvarado Gil, Dr. Máximo Pech Canul, Dr. Trystan Watson y al Dr. Humberto Mandujano Ramírez, por sus valiosos comentarios y observaciones a este trabajo.

Al Dr. Gerko Oskam, de quién nunca ha faltado apoyo y ha sido siempre no sólo un excelente asesor, pero también un gran consejero.

Al CINVESTAV Mérida, por ser mi segundo hogar y por haberme brindado la formación académica necesaria para, eventualmente, convertirme en un investigador nacional.

Al Consejo Nacional de Ciencia y Tecnología (CONACyT), la Secretaría de Energía (SENER) y al Instituto de Energías Renovables de la Universidad Nacional Autónoma de México (IER-UNAM) por el financiamiento a través del Centro Mexicano de Innovación en Energía Solar (CeMIE-Sol), Proyecto P-27: "Desarrollo y fabricación de módulos de celdas solares de TiO2 sensibilizadas con colorante (DSC) y puntos cuánticos (QDs), y de orgánicas fotovoltaicas (OPVs)".

A CONACyT por el financiamiento a través de la beca de ciencia básica CB-2012-178510, así como por mi beca de 4 años de doctorado y la beca adicional de un año durante mi estancia internacional en la Universidad de Uppsala, en Uppsala, Suecia.

A todos ustedes, de corazón, gracias.

ABSTRACT

Among renewable energy technologies, solar energy has been one of the most investigated energy sources over the past decades. High cost of traditional photovoltaics has delayed a widespread implementation of this technology, especially in developing countries such as Mexico, which possesses an outstanding potential for solar energy production. Dye-sensitized solar cells (DSCs) have emerged as one of the most promising solar cell technologies since they are easy to fabricate, do not require expensive materials and have large design opportunities. However, dye-sensitized solar cells are very complex electrochemical systems, and in order to further develop this technology, the mechanisms that govern the internal processes in the dye-sensitized solar cells have to be completely elucidated. In this work, steady-state and small perturbation techniques are employed in a variety of DSC configurations in order to obtain a better understanding of charge transport and recombination processes.

One of the factors that affect DSC performance is the thickness of the nanostructured, mesoporous TiO_2 film; a thicker TiO_2 film allows for more dye to be adsorbed, increasing the light harvesting efficiency, but at the same time it will increase the number of recombination sites. The influence of the thickness of the nanostructured, mesoporous TiO_2 film on several parameters determining the performance of a dye-sensitized solar cell is investigated both experimentally and theoretically, paying special attention to the effect of the exchange current density in the dark. Using a continuity equation model for the total electron density, a relationship between the exchange current density in the dark and the recombination time constant and electron density in the dark is analytically derived and

corroborated experimentally, and the values for the exchange current density in the dark determined by steady-state and small perturbation techniques are compared. An evaluation of the influence on the optimal film thickness of the exchange current density, the solar cell ideality factor, and the effective absorption coefficient is presented. The results show that the exchange current density in the dark is proportional to the TiO_2 film thickness although the effective absorption coefficient is the parameter that ultimately defines the ideal thickness. The importance of the exchange current density in the dark on the determination of the current–voltage characteristics is highlighted, showing that an important improvement of the cell performance can be achieved by decreasing values of the total series resistance and the exchange current density in the dark. Differences in the value obtained for the exchange current density show the fundamental differences in recombination processes under illumination and in the dark.

Cobalt redox couples represent an interesting alternative to the more commonly used iodide/triiodide redox couples, since they possess a more positive redox potential which may increase the maximum photovoltage a DSC can achieve. However, the kinetics of recombination for these redox couples are usually very fast since the reaction involves only one electron. A study of the performance and charge recombination with steady-state and small perturbation techniques for DSCs with a Z-907 ruthenium dye and I^-/I_3^- and $[Co(bpy)_3]^{2+/3+}$ redox illustrates, however, that the ruthenium dye is not an adequate sensitizer for DSCs when $[Co(bpy)_3]^{2+/3+}$ redox couples are present, since recombination proved to be very fast for this system. On the other hand, Z-907 is an adequate sensitizer when the recombination reaction has slower kinetics, as in the case for the iodide/triiodide redox couple.

DSCs with copper-based redox couples have shown open circuit potentials above 0.9 V and thus are emerging as real alternative redox mediators in DSCs. In this work, a copper-based electrolyte solution is employed and studied for DSCs. A study of the mass transport of the redox couple via transient photocurrent and cyclic voltammetry measurements is reported and the influence of the distance between electrodes on the performance of the copper-based solar cells is studied with steady-state and electrochemical impedance spectroscopy measurements. The results show that the diffusion coefficient for this copper redox couple is lower than for cobalt and iodide pairs, and that mass transport in the bulk may be a limiting factor for this DSC configuration. It is also shown that reducing the distance between electrodes decreases mass transport limitation and a sealed cell configuration with the lowest possible separation between electrodes is presented. Impedance analysis show an inductive behavior at low frequencies for this configuration, probably associated with direct interaction between electrons in the TiO_2 mesoporous layer and the polymer counter electrode, and an equivalent circuit to model this DSC configuration is proposed. The best cells with the new copper-based redox couples had an 8.2% efficiency, with an open circuit voltage of 1.01 V, a short circuit current density above 10 mA/cm^2 and a Fill Factor close to 0.75.

The last part of this work is dedicated to the description of the elaboration of high efficiency solid-state DSCs, using a mesoporous layer of TiO_2, the organic dye LEG 4 and spiro-OMeTAD as hole conductor. An efficiency of 6.4% has been achieved for this interesting and practical design

RESUMEN

De entre las diferentes energías renovables, la energía solar ha sido una de las fuentes de energía más investigada durante las últimas décadas. El elevado costo de los dispositivos fotovoltaicos tradicionales ha impedido una mayor implementación de esta tecnología, especialmente en países en vías de desarrollo como México, que particularmente posee un destacado potencial para la producción de energía solar. Las celdas solares sensibilizadas con tinte, (DSCs por sus siglas en inglés, o celdas dye) han emergido como una de las tecnologías solares más prometedoras debido a que son fáciles de fabricar, no requieren materiales muy costosos y las amplias posibilidades de diseño que ofrecen. Sin embargo, las celdas dye son sistemas electroquímicos muy complejos y, con mira en un desarrollo amplio de esta tecnología, los mecanismos que gobiernan los procesos internos en las celdas dye deben ser entendidos ampliamente. En este trabajo se utilizan técnicas de estado estacionario y de pequeña perturbación sobre una variedad de configuraciones de celdas dye con el objetivo de conseguir comprender mejor los procesos de transferencia de carga y de recombinación.

Uno de los factores que afectan el desempeño de las celdas dye es el espesor de la película mesoporosa de TiO_2; un mayor espesor en esta película permite adsorber una mayor cantidad de tinte, incrementando la eficiencia de absorción de luz, pero al mismo tiempo el número de sitios de recombinación se incrementará también. La influencia del espesor de la película nanoestructurada, mesoporosa de TiO_2 en diferentes parámetros de la celda solar es investigada tanto teórica como experimentalmente, poniendo especial atención al efecto de la densidad de corriente de intercambio en el oscuro. Utilizando un modelo basado en la ecuación de continuidad en función de la densidad electrónica total, la relación entre la

densidad de corriente de intercambio en el oscuro, la constante de recombinación y la densidad electrónica en el oscuro es analíticamente determinada y corroborada experimentalmente, y se compara con los valores para la densidad de corriente de intercambio en el oscuro determinados por medio de mediciones de estado estacionario y pequeña perturbación. Se presenta, también, un estudio sobre la influencia de la densidad de corriente de intercambio en el oscuro, el factor de idealidad y el coeficiente de absorción efectivo de la celda en la determinación del espesor óptimo de la película mesoporosa de TiO_2. Los resultados muestran que la densidad de corriente de intercambio en el oscuro es proporcional al espesor de la película mesoporosa de TiO_2, pero que el coeficiente de absorción efectivo de la celda es el parámetro que realmente determina el espesor ideal de la película mesoporosa de TiO_2. Se resalta la importancia de la densidad de corriente de intercambio en el oscuro para la determinación de los parámetros de la curva corriente-voltaje, mostrando que un importante incremento en el desempeño de la celda se puede lograr disminuyendo los valores de la resistencia en serie total y la densidad de corriente de intercambio en el oscuro. Las diferencias en el valor de este parámetro bajo condiciones de iluminación y en el oscuro muestran las diferencias fundamentales en los procesos de recombinación bajo iluminación y en el oscuro.

Los pares redox de cobalto representan una alternativa interesante a los pares de yoduro/tri-yoduro, ya que poseen un potencial redox más positivo, lo que puede ayudar a incrementar el voltaje final en una celda dye. Sin embargo, la cinética de recombinación para estos pares es, usualmente, muy rápida debido a que la reacción involucra únicamente un electrón. Por otra parte, los tintes de rutenio no han conseguido hacer una transición exitosa hacia los pares redox alternativos, pues las celdas dye con tinte de rutenio y par de cobalto suelen presentar

alta recombinación. En este trabajo se presenta un estudio del desempeño y la recombinación de carga para celdas dye con tinte de rutenio Z-907 y pares de I^-/I_3^- y $[Co(bpy)_3]^{2+/3+}$, mediante técnicas de estado estacionario y pequeña perturbación. Los resultados muestran que el tinte de rutenio no es un tinte adecuado para celdas con $[Co(bpy)_3]^{2+/3+}$ como par redox, debido a que la recombinación es muy grande. Al mismo tiempo, el tinte de rutenio es adecuado para celdas dye con el par de I^-/I_3^-, debido a que la cinética de recombinación de este par es más lenta.

Se ha reportado que es posible desarrollar celdas dye con pares redox basados en cobre capaces de presentar voltajes por encima de los 0.9 V y así, han emergido como una alternativa real para su aplicación en celdas dye. En este trabajo, una solución electrolítica con un par redox basado en cobre es empleada y estudiada en la celda dye. Se realizó un estudio del transporte de masa del par redox mediante transientes de fotocorriente y voltametría cíclica. La influencia de la distancia entre los electrodos en el desempeño de la celda dye con pares de cobre es analizada mediante mediciones de estado estacionario e impedancia electroquímica. Los resultados muestran que el coeficiente de difusión para este par de cobre es menor que el reportado para pares de cobalto y de yoduro, y que el transporte de masa para este par puede representar un factor que limite el desempeño de las celdas solares. Se demuestra, también, que al reducir la distancia entre los electrodos, el efecto del transporte de masa disminuye y se propone una configuración de una celda sellada con la menor distancia posible entre los electrodos. Mediante los análisis de impedancia se observa un comportamiento inductivo a bajas frecuencias para esta configuración, probablemente asociado con interacción directa ente los electrones en la capa mesoporosa de TiO_2 y el contra electrodo. Un circuito eléctrico equivalente es propuesto para modelar esta configuración.

Las mejores celdas con el nuevo par redox basado en cobre presentaron eficiencias del 8.2%, con valores de circuito abierto de 1.01 V, densidades de corriente de corto circuito por encima de los 10 mA/cm^2 y factores de llenado cercanos a 0.75.

La última parte de este trabajo está dedicada a la descripción del proceso de elaboración de celdas solares sensibilizadas con tinte de estado sólido de alta eficiencia, utilizando una película mesoporosa de TiO_2, el tinte orgánico LEG 4 y spiro-OMeTAD como conductor de huecos, obteniendo una eficiencia del 6.4% para celdas con este interesante y práctico diseño.

TABLE OF CONTENTS

INDEX OF TABLES

INDEX OF FIGURES

INTRODUCTION

Due to the intervention of mankind, global climate change is faster than ever before. Overwhelming scientific evidence shows that emission of greenhouse gases is the main responsible of this effect. The main source of energy currently consists of fossil fuels, and it has been pointed out that a transition from fossil fuels to renewable energy sources is necessary to start reducing the concentration of greenhouse gases in the atmosphere. Solar energy is the most promising source of renewable energy due to its abundance on the surface of the Earth. However, the currently available commercial devices are still very expensive, making them unreachable for the average person, especially in developing countries such as Mexico. One of the most investigated topics around the world is focusing to solve this problem; how to make solar cells more efficient and affordable. International efforts all over the world have led to development of new generations of solar cells. Third generation solar cells, currently under development, are based on relatively abundant and affordable materials capable of delivering competitive efficiencies and prices to those offered by currently available solar cells. However, the task has proven to be an important challenge, due to the complexity of some of these third generation solar cells.

Among these devices, dye-sensitized solar cells (DSCs) represent a promising system that has already achieved efficiencies above 10%. However, the dye solar cell device is a complex system, composed of several materials simultaneously interacting, and in order to propose improvements in the device structure and alternative materials, a better understanding of the system is required. Several characterization techniques have been developed with this goal in mind and a wide set of techniques are currently available.

In this work, a detailed study of several components of the DSC is performed, applying steady-state and small perturbation techniques to gain insight into the mechanisms of charge transfer and recombination inside the DSCs, showing the differences in the analysis and interpretation of results, depending of the system under study. **In chapter 1,** a brief introduction on climate change and renewable energies is presented, with special focus on solar power generation. Electricity generation in Mexico is described, showing the potential of solar power implementation. Particularly, DSCs may represent a real alternative as solar cell technology and in **chapter 2,** a detailed description of the DSCs is given, highlighting the role of each of its components in the final performance of the devices. A brief introduction to solid-state DSCs is also presented. In order to unravel the intricate mechanisms that dominates the internal processes inside DSCs, different characterization techniques are employed and, in **chapter 3,** the fundamental principles behind them are described, along with a description of the information obtained. Using some of these characterization techniques, different components of the DSCs are employed. The use of cobalt alternative redox couples together with ruthenium sensitizers is studied in **chapter 4,** and compared with traditional iodide/triiodide redox couples. A study on the DSCs performance and charge recombination processes is performed with steady-state and small perturbation techniques, highlighting also the importance of a blocking layer. **In chapter 5,** the influence of the thickness of the nanostructured, mesoporous TiO_2 film on several parameters determining the performance of a dye-sensitized solar cell is investigated both experimentally and theoretically. The effect of the exchange current density in the dark is highlighted, and a comparison between the values obtained by steady state measurements with values extracted from small perturbation techniques is made. The influence of exchange current density, the solar cell ideality factor, and the effective absorption coefficient of the cell on the optimal

film thickness is also studied. Mass transport studies are performed for copper-based DSCs in **chapter 6**, investigating, also, the influence of the distance between electrodes on the performance of the solar cells. A sealed cell configuration with the lowest possible separation between electrodes is proposed and studied with impedance spectroscopy. Solid-state DSCs are an alternative design for standard DSCs that should present higher stability, and a large part of the mechanisms that govern the behavior of DSCs are also present for these solid-state solar cells. **In chapter 7** a detailed description on the elaboration of solid-state DSCs is presented, along with characterization using current-voltage measurements and impedance spectroscopy.

CHAPTER 1

On the global energy scenario and climate change

Since about 1850, global use of fossil fuels (coal, oil and gas) has become the most used energy supply for mankind. However, the rapid rise in fossil fuel combustion has produced a corresponding rapid growth in carbon dioxide (CO_2) emissions (Figure 1.1).

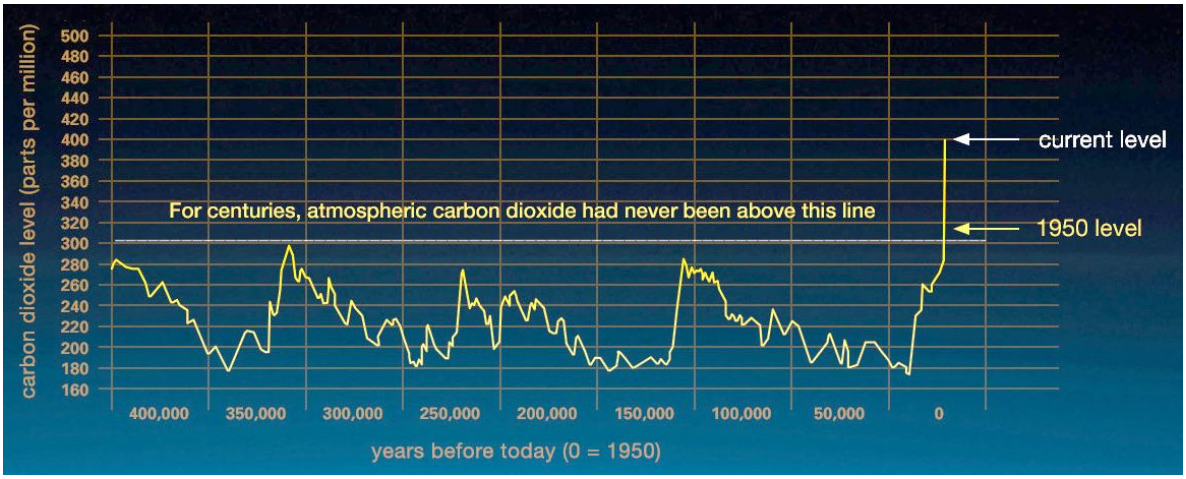

Figure 1.1. Evolution of CO_2 level (in ppm) over time. The data was obtained from comparison of atmospheric samples contained in ice cores and recent direct measurements[1].

When solar radiation reaches the Earth, some of this radiation is absorbed in the atmosphere, and some reaches the Earth's surface and is re-radiated back to space. Additionally, the Earth's heated surface emits infrared radiation. Greenhouse gases (GHG), trap some of this radiation and re-emit it back to the atmosphere and the Earth's surface in the form of long wavelength radiation. This effect is known as the "greenhouse effect". Some of the gases that

contribute to this effect include water vapor, CO_2, methane (CH_4) and nitrous oxide (N_2O). Most of the observed increase in global average temperature since the mid-20th century is very likely (>90% assessed probability of occurrence) due to the observed increase in CO_2 and greenhouse gases emissions[2]. This increase in global average temperature has enormous effects on the planet. Global warming causes polar ice sheets and glaciers to melt. It also warms up the water in the ocean, and when the water is warmed, it expands. The combination of these changes is causing sea levels to rise, resulting in flooding and erosion of coastal and low lying areas, threatening dense coastal populations and destroying ecosystems such as mangroves and wetlands that protect coasts against storms. Sea level rise will not stop in 2100 because the oceans take a very long time to respond to warmer conditions at the Earth's surface. Ocean waters will therefore continue to warm and sea levels will continue to rise for many centuries at rates equal to or higher than that of the current century[1,3,4]. Higher temperatures increase the amount of moisture that evaporates from land and water, leading to drought in many areas. Lands affected by drought are more vulnerable to flooding once rain falls. As temperatures rise globally, droughts will become more frequent and more severe, with potentially devastating consequences for agriculture, water supply and human health. High temperatures and dry conditions also increase the likelihood of forest fires[3,5]. Rising temperatures are changing weather and vegetation patterns across the globe, forcing animal species to migrate to new, cooler areas in order to survive. The rapid nature of climate change is likely to exceed the ability of many species to migrate or adjust. Experts predict that one-fourth of Earth's species will be headed for extinction by 2050 if the warming trend continues at its current pace[3,4]. In the absence of additional climate policies, the Intergovernmental Panel on Climate Change (IPCC) project that the global average temperature will rise between 1.1°C and 6.4°C over this century (Figure 1.2). This range of

uncertainty arises from uncertainty about the amount of GHGs that will be emitted in the future, and from uncertainty about the climate sensitivity. The Cancun Agreements (2010) call for limiting the global average temperature rise to no more than 2°C above pre-industrial values, and agrees to consider a goal of 1.5°C. In order to be confident of achieving an equilibrium temperature increase of only 2°C to 2.4°C, atmospheric GHG concentrations would need to be in the range of 445 to 490 ppm *CO_2eq*.

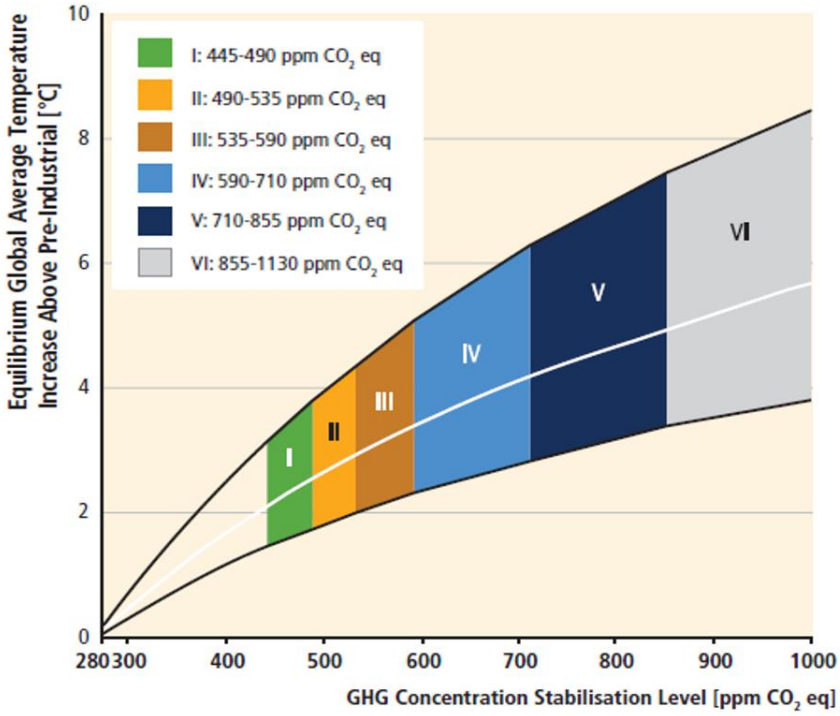

Figure 1.2. Relationship between the concentration of CO_2eq and the likely equilibrium global average temperature. Six different scenarios are depicted. Temperature above pre-industrial values refers to the average temperature prior to industrial revolution; it is represented with a value of, approximately, 280 ppm CO_2eq[2].

Renewable energy supply sources are an effective way of lowering CO_2 emissions because they have low *carbon intensity* with emissions per unit of energy output typically 1 to 10% that of fossil fuels.

1.1 Renewable Energies

Renewable energy (RE) is any form of energy from solar, geophysical or biological sources that is replenished by natural processes at a rate that equals or exceeds its rate of use[2]. RE is obtained from the continuing or repetitive flows of energy occurring in the natural environment and includes resources such as biomass, solar energy, geothermal heat, hydropower and wind energy. Fossil fuels (coal, oil, natural gas) do not fall under this definition, as they are not replenished within a time frame that is short relative to their rate of utilization[2]. According to data from the International Panel on Climate Change[2], *life-cycle global warming* emissions associated with renewable energy, including manufacturing, installation, operation, maintenance, dismantling and decommissioning, are minimal (Figure 1.3). Compared with natural gas, which emits between 270 and 900 grams of carbon dioxide equivalent per kilowatt-hour (CO_2eq/kWh), and coal, which emits between 630 and 1630 grams of CO_2eq/kWh, wind emits only 9 to 18 grams of CO_2eq/kWh, solar 30 to 90, geothermal 45 to 90, and hydroelectric between 45 and 225. Renewable electricity generation from biomass can have a wide range of global warming emissions depending on the resource and how it is harvested. Sustainably sourced biomass has a low emissions footprint, while unsustainable sources of biomass can generate significant global warming emissions[2].

The present annual worldwide electricity consumption rate is 12 TW and is expected to double to 24 TW by 2050. Therefore, there is an urgent need to reduce our dependence on fossil fuels by augmenting it with supplies from cleaner, renewable sources of energy.

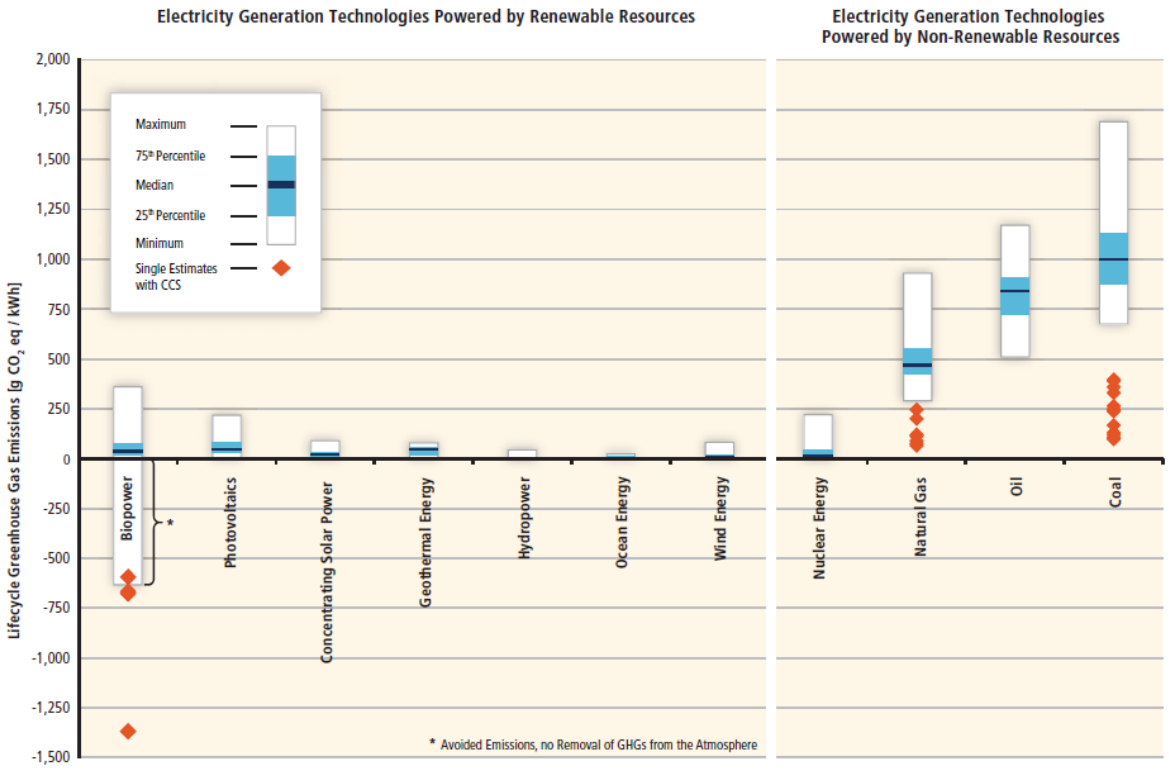

Figure 1.3 Estimates of lifecycle GHG emissions (g CO_2eq/kWh) for broad categories of electricity generation technologies. Land use-related net changes in carbon stocks and land management impacts are excluded; negative estimates for biopower are based on assumptions about avoided emissions from residues and wastes in landfill disposals and co-products. CCS: *Carbon capture and storage*[2].

Renewable energy contributes only 22% of the global electricity production. The remaining 78% is provided by non-renewable energy, which includes coal, natural gas and nuclear. Between renewable energies, hydro provides a major share of 16.6%, followed by 3.2% by wind, 1.4% by biomass, 0.5% by solar photovoltaics (PV) and 0.4% by geothermal[6]. The theoretical potential of RE is much larger than all of the energy that is used by all the economies on Earth. The technical potential for solar energy is the highest among the RE sources[2]. As well as having a large potential to mitigate climate change, renewable energies can provide wider benefits. RE may, if implemented properly, contribute to social and economic development, energy access, a secure energy supply, and reducing negative

impacts on the environment and health. The implementation of a specific RE will depend on the natural resources available and the economic feasibility for their proper exploitation. Each country has to find the best way to implement RE into their energetic production taking into consideration these factors. In this way, countries like Iceland have managed to produce 99% of their electricity form hydro and geothermal power. Norway produces more hydroelectricity than it needs and exports its surplus to the rest of Europe. Brazil, New Zealand and Canada also have a high share of hydroelectricity in total electricity: 80, 65 and 60%, respectively[7]. Brazil relies heavily on and is the second-largest producer of bioethanol, which it produces from sugarcane[2,7]. Morocco has taken advantages of their geographic location and has installed a massive solar power plant in the Sahara Desert, which will become the largest solar power production facility in the world[8]. RE has featured prominently in the United Nations agenda on environment and development through various initiatives and actions. The International Energy Agency (IEA)[7] has provided a forum for discussing energy issues among the Organization for Economic Co-operation and Development (OECD) countries, and provides annual reports on all forms of energy including RE. REN 21[9], a nongovernmental organization, compiles recent data on RE resources based upon industrial and governmental reports. A new international organization, the International Renewable Energy Agency (IRENA)[10], was also established in 2009 and has 149 member countries (Mexico included)[2].

1.2 Solar energy and solar cells

Solar energy has the largest potential among RE sources to satisfy the future global need for energy. The sun provides the earth in one hour with as much energy as all mankind uses in one year[6]. From the 1.7×10^5 TW of solar power that strikes the earth's surface, a practical

terrestrial global solar potential value is estimated to be about 600 TW. Thus, using 10% efficient solar farms, about 60 TW of power could be supplied[11]. The solar resource is virtually inexhaustible, and it is available and able to be used in all countries and regions of the world[2]. Solar energy technologies harness the solar irradiance to produce thermal energy (solar heating) or electricity using photovoltaics or concentrating solar power (CSP) (Figure 1.4).

a) Solar heating

In a solar heating system, the solar collector absorbs solar irradiance to heat a carrier fluid (e.g., water, air) to transfer that heat to a well-insulated storage tank, where it can be used when needed. Its design is influenced by the system in which it will operate and by the climatic conditions of the installation location[2].

b) Concentrating solar power

In trough concentrators, long rows of parabolic reflectors concentrate the solar irradiance onto a heat collection element (HCE) mounted along the reflector's focal line. The HCE comprises a steel inner pipe (coated with a solar-selective surface) and a glass outer tube, with an evacuated space in between. Heat-transfer oil is circulated through the steel pipe and heated to about 390 °C. The hot oil from numerous rows of troughs is passed through a heat exchanger to generate steam for a conventional steam turbine generator[2].

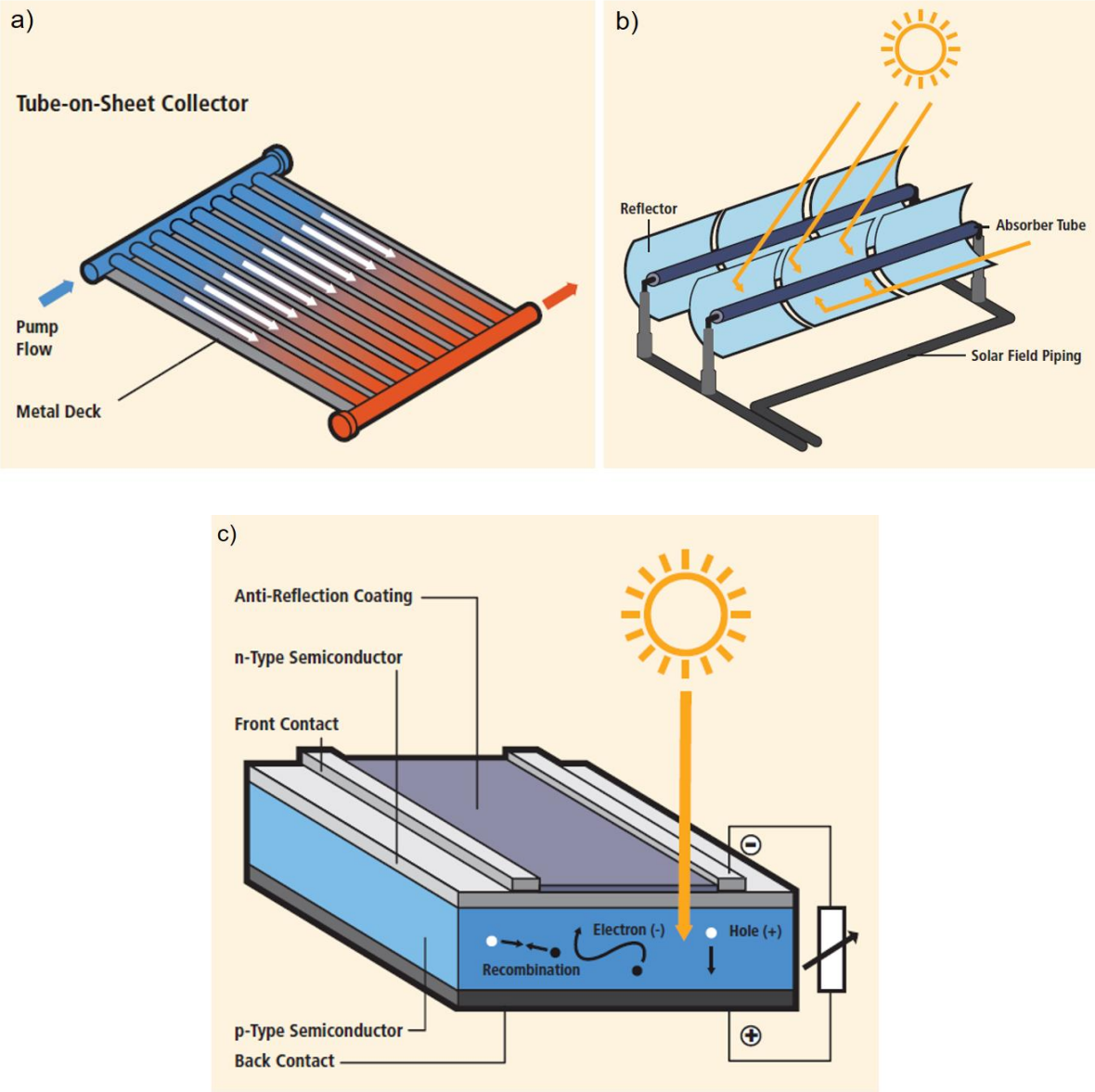

Figure 1.4. Schematic diagram of (**a**) Solar heating system, (**b**) Trough concentrator and (**c**) Single-junction photovoltaic device[2].

c) Photovoltaics

In currently commercially available photovoltaics, light shining on a semiconductor generates electron-hole pairs that are separated spatially by an internal electric field on either side of an interface known as a p-n junction. This creates negative charges on one side of the interface and positive charges on the other side. This resulting charge separation creates a

voltage. When the two sides of the illuminated cell are connected to a load, current flows from one side of the device via the load to the other side of the cell[2]. Single junction solar cells have a maximum theoretical efficiency of around 31%, known as the Shockley-Queisser limit[11,12].

Solar energy is one of the fastest growing renewable energy technologies; the global total of solar PV was roughly 67 GW at the end of 2011, to be compared with just 1.5 GW in 2000. However, this is still an insignificant figure compared to the energy from sources like coal, nuclear and natural gas, since solar photovoltaics share an amount of 0.5% in the global electricity production[6]. Once installed, the maintenance cost of solar plants is very low. Solar technologies can also improve the health and livelihood opportunities for many of the world's poorest populations. Solar home systems and PV-powered community grids can provide economically favorable electricity to many areas for which connection to a main grid is impractical, such as in remote regions. Solar home systems can also power televisions, radios and cellular telephones, resulting in increased access to information and distance education opportunities[2]. However, solar technologies face some challenges for global deployment. Solar power plants require more land than other power plants for the same amount of power produced. The disposal of solar cells at the end of their life time has also to be considered. Some materials used in solar cells may contaminate the soil and environment. The initial installation cost for solar power is high. The cost per kWh of electricity produced by solar power is still higher than conventional sources, like coal and nuclear[2,6]. Extensive research is ongoing all over the world, to improve this technology and make it available to the common man[6]. Emerging PV technologies are still under development and in laboratory or pilot stage, but could become commercially viable within the next decades. They are based on very low-

cost materials and/or processes and include technologies such as dye-sensitized solar cells, organic solar cells and low-cost versions of existing inorganic thin-film technologies[2].

1.3 Renewable energies in Mexico

Mexico produced a total of 278,156.65 GWh of electricity in 2015, with an electrical consumption per habitant of 2,055.59 kWh[13]. The majority of the conventional energy in Mexico comes from oil and natural gas, where natural gas is increasingly replacing oil in power generation. However, Mexico is a net importer of natural gas, mainly from the US. Mexico is also a significant crude oil exporter, the third largest in America, but at the same time, is a net importer of refined petroleum products[14]. Mexico's total energetic production in 2015 came mostly from petroleum, natural gas, coal and nuclear (81.24%), obtaining only 18.76% of its energy from renewable sources (Figure 1.5).

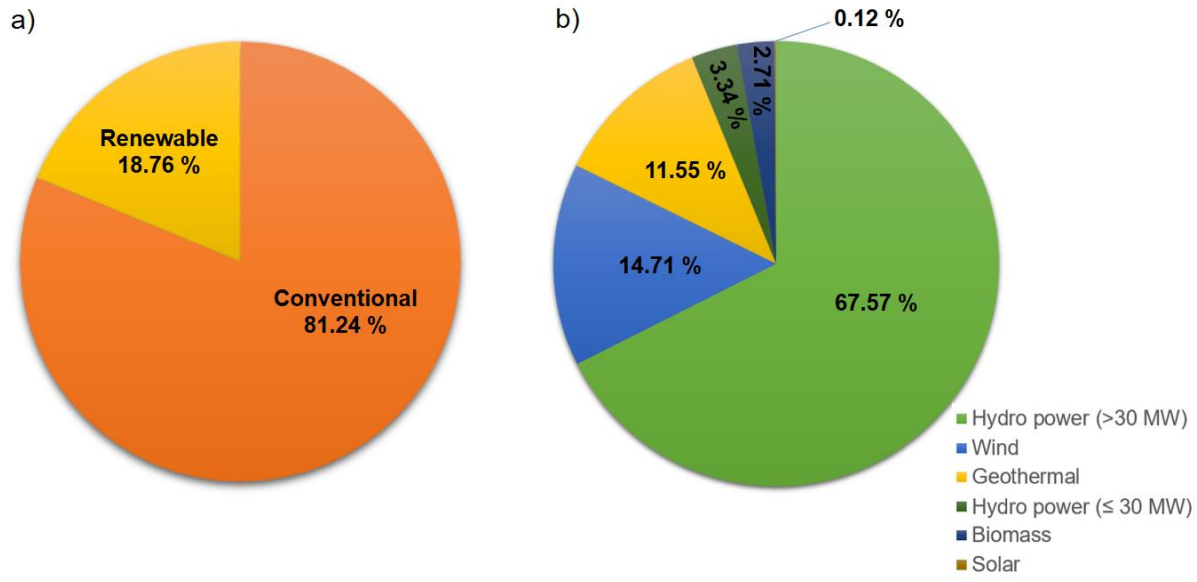

Figure 1.5. Electrical power generation in Mexico: (**a**) Conventional vs. Renewable and (**b**) Contribution of each renewable energy. Electrical power generation from July 1st 2014 to June 30th 2015[15].

The majority of the renewable energy produced in Mexico comes from hydro power, followed by wind and geothermal power. Solar power represents less than 1% of the total renewable energy produced. Due to its geographical position, territorial extension and natural resources, Mexico possesses an outstanding potential for the implementation of renewable energy as primary source. In Table 1.1, a comparison between the total electricity produced and the potential electrical production by renewable sources is presented.

Table 1.1. Current and potential electrical generation per renewable energy[15].

Current electrical generation per renewable energy (GWh/y)					
	Geothermal	**Hydro**	**Wind**	**Solar**	**Biomass**
TOTAL	6,027.00	36,991.00	7,676.00	62.00	1,414.00
Potential electrical generation per renewable energy (GWh/y)					
Proved	2,355.00	4,796.00	19,805.00	16,351.00	2,396.00
Probable	45,207.00	23,028.00	-	-	391.00
Possible	52,013.00	44,180.00	87,600.00	6,500,000.00	11,485.00

In Table 1.1, "proved potential" represents the electricity production that counts with enough technical and economic studies to account for its viability. "Probable potential" represents the electricity production that counts with direct and indirect field studies but no technical or economic studies have been performed to prove its viability. "Possible potential" represents the theoretical potential of installation capacity and electricity generation according to indirect studies, without field, technical nor economic studies to account for its viability[15]. The National Energy Strategy outlined by the Energy Bureau (SENER) and the Works and Investment Program of the Electricity Sector (POISE) set up by the Federal Electricity

Commission (CFE) set a goal to generate 35% of electricity from non-fossil sources by 2024[14]. According to Table 1.1, wind and solar power will have to play a primary role in order to achieve such a goal. Several wind projects are in development in Mexico's Baja California and in southern Mexico with the aim of boosting Mexico's wind generation capacity to 12 GW by 2020. Mexico is poised to become one of the world's fastest-growing wind energy producers[14]. Mexico has 1005 MW of geothermal capacity, making the country fourth in terms of global geothermal capacity, only behind US (3442), Philipines (1968) and Indonesia (1339)[14]. However, solar power still remains as the most promising opportunity for energy production in Mexico.

1.3.1 Solar energy "opportunities" in Mexico

According to Table 1.1 and Figure 1.6, Mexico has an impressive potential to exploit solar power. It has been roughly estimated that, due to the high amount of solar radiation that reaches Mexico's surface every day (Figure 1.6), it will potentially be able to generate up to 6,500,000 GWh/y[13,15]. This impressive quantity is more than enough to cover the entire energy needs of the country, with an outstanding surplus of around 6,200,000 GWh/y. It is more than 23 times the total amount of energy currently produced by all the sources added together. Figure 1.6 shows that all the Mexican territory is potentially suitable for harvesting solar energy, receiving an average of 6-7 kWh/m^2d.

In Mexico, solar power is the renewable energy with the highest potential, over 74 times the potential of wind power, which is the second most promising technology, but in spite of that, solar power still remains as the least exploited renewable energy, producing only 62 GWh/y, which are provided by the only eight solar power plants currently installed in Mexico's

territory (Table 1.2). However, the number of locations of proved potential energy production overshadows the current amount of solar power plants (Figure 1.7).

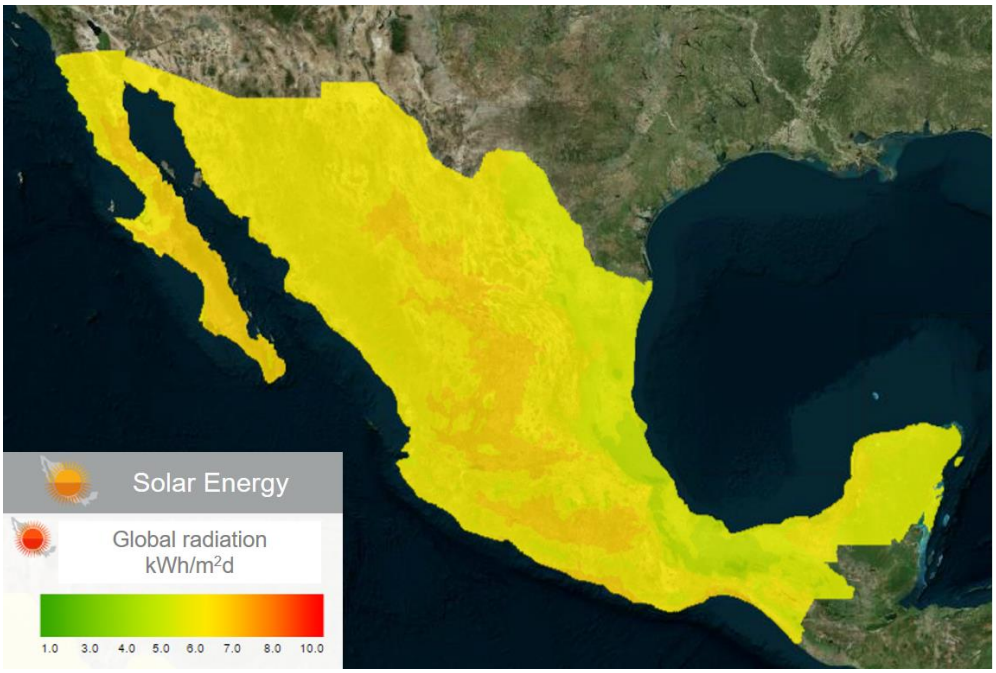

Figure 1.6. Average global radiation per day in Mexico's surface (kWh/m^{2}d)[15].

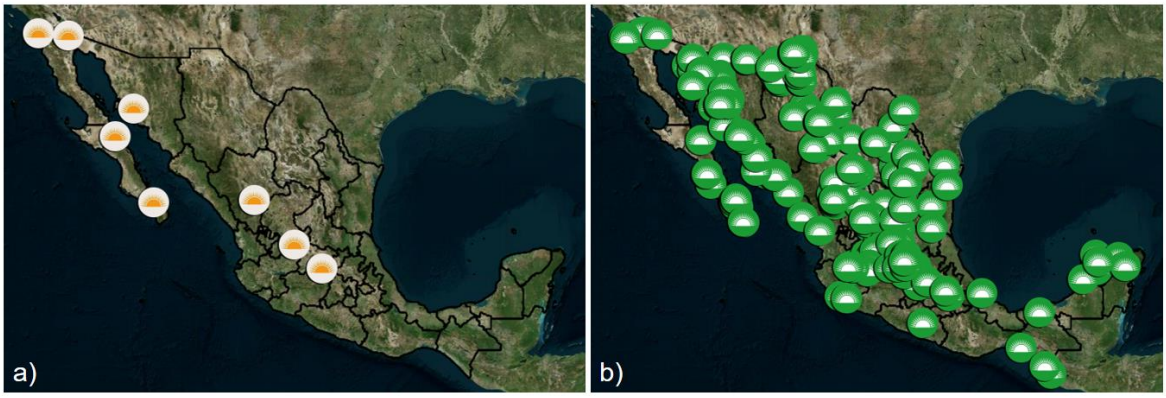

Figure 1.7. (**a**). Installed solar power plants. (**b**) Potential locations to install solar power plants. Data updated until June 30th, 2015[15].

The comparison between images in Figure 1.7 depicts clearly the amount of opportunities to exploit solar power in Mexico. Actually, there are projects in all the proved locations to install solar power, either as photovoltaics or as thermosolar energy. Some of these locations are already under construction. When finished, the projected amount of energy they will produce will be around 16,351.4 GWh/y, which is over 250 times the amount of solar power currently produced.

Table 1.2. Current solar power plants installed in Mexico[15].

Federal entity	*Installation*	*Capital*	*Type*	*Power generated (GWh/y)*
Aguascalientes	Autoabastecimiento removable	Private		1.66
Baja California	Cerro Prieto	CFE		10.83
	PLAMEX	Private		1.76
Baja California Sur	Santa Rosalía	CFE		2.07
	Servicios comerciales de Energía		Photovoltaic	30.43
Durango	Tai Durango Uno	Private		14.58
Guanajuato	Generador Solar Apaseo			0
Sonora	Coppel			0.66

Although it sounds promising and shows that Mexico is definitively moving towards renewable and, particularly, solar power, the total amount of projected production will only account for 5.9% of the total amount of energy produced today.

1.3 Terminology of Chapter 1

Carbon Capture and Storage: Process of capturing waste CO_2 from large point sources, such as fossil fuel power plants, transporting it to a storage site, and depositing it where it will not enter the atmosphere, normally an underground geological formation[16].

Carbon intensity: The carbon intensity is a quantity that expresses how many tonnes of CO_2 are emitted for each unit of energy supplied[7].

CO_2eq: A carbon dioxide equivalent, CO_2eq, is a measure to express the impact of each different greenhouse gas in terms of the amount of CO_2 that would create the same amount of warming[17].

Global radiation: Total short-wave radiation from the sky falling onto a horizontal surface on the ground. It includes both the direct solar radiation and the diffuse radiation resulting from reflected or scattered sunlight[18].

Global warming potential (GWP): Relative measure of how much heat a greenhouse gas traps in the atmosphere. It compares the amount of heat trapped by a certain mass of the gas in question to the amount of heat trapped by a similar mass of carbon dioxide. A GWP is calculated over a specific time interval, commonly 20, 100 or 500 years[14].

Life-cycle greenhouse gas emissions: Life-cycle assessment of each energy source, presenting the findings in units of global warming potential per unit of electrical energy generated by that source These assessments attempt to cover the full life of the source, from material and fuel mining through construction to operation and waste management[19].

CHAPTER 2

Third generation solar cells

The annual production of solar photovoltaic energy is currently dominated by silicon modules. These devices belong to the first generation of solar cells and represented 85% of the commercial solar cells available in 2009. However, despite their high efficiency, this generation of solar cells requires high manufacturing costs and high purity materials[20]. Second generation solar cells take advantage of the thin film technology, replacing the use of silicon by other semiconductors, such as cadmium telluride (CdTe) or copper indium/gallium selenide (CIS/CIGS). This type of technology allows a reduction in the manufactory costs, however, it has some drawbacks such as the use of toxic materials and a lower efficiency compared with silicon solar cells. In the third generation of solar cells wide band-gap semiconductors are employed, such as TiO_2, ZnO, SnO_2, and some others. The third generation solar cells aim for a low-cost and high performance using nanomaterials. The working principle and manufacturing technologies vary greatly from Si solar cells. Though third generation solar cells have not reached the practical efficiency levels of Si solar cells, they possess great potential with the use of nanotechnology[6]. Dye-sensitized solar cells (DSCs) and solid-state dye-sensitized solar cells (ssDSCs) fall into this category.

2.1 Dye-sensitized solar cells

In 1991 Brian O'Regan and Michael Grätzel presented the dye-sensitized solar cell, a new type of solar cell configuration made of readily available materials with an overall efficiency of 7.1%[21]. Dye-sensitized solar cells are a promising photovoltaic concept for a number of

reasons. It does not require high purity materials, promise significantly lower processing costs than existing technologies for other solar cells, are easy to fabricate, offer design opportunities such as transparency and multicolor options and present a short energy payback time (<1 year)[6,11,20,22–26]. The highest certified efficiency for these cells is 11.9 ± 0.4% for a single cell (1 cm^2), 10.7 ± 0.4% for a minimodule (7 serial cells, 26.6 cm^2) and 8.8 ± 0.3% for a submodule (26 serial cells, 398.8 cm^2), all made by the Sharp company[27], although efficiencies above 14% for a single small cell (0.1 cm^2) have been recently reported by Kakiage *et al*[28].

The DSC consists of a transparent conductive oxide (TCO) on which a layer of a nanostructured, mesoporous semiconductor, usually TiO_2, is deposited. The semiconductor does not absorb visible light so it has to be sensitized with a dye, typically an organometallic ruthenium complex, although it is common to use purely organic dyes instead[29–33]. The counter electrode consists of another TCO with an electrocatalyst deposited on the surface. The working and counter electrode are sealed together with a thermoplastic polymer (30-60 μm thick) and the cell is filled with an electrolyte solution based on an organic, low viscosity solvent and a redox couple, typically iodide/triiodide, although nowadays it is common to use alternative redox couples[22,30–43]. A schematic representation of a DSC is displayed in Figure 2.1. When the cell is illuminated, the dye absorbs part of the light and is brought into an excited state, S^* (1). The excited state of the dye then injects an electron into the semiconductor layer (2) and the electron travels through the mesoporous network until it's collected in the TCO (3). The now oxidized dye molecule, S^+, is regenerated via the reduced component of the redox couple in the electrolyte solution (4). The oxidized component of the

redox couple diffuses to the counter electrode (5) where it is reduced to maintain an equilibrium concentration and closes the circuit (6).

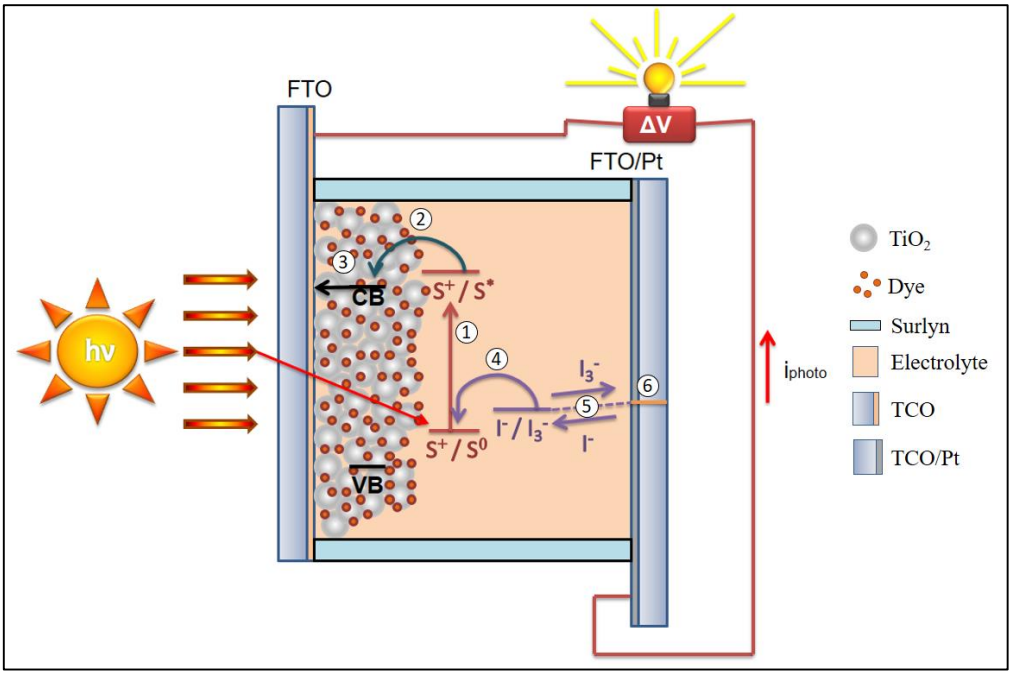

Figure 2.1. Energetic representation of the processes occurring in a DSC[24]. The main components of the DSC are highlighted.

However, the photogenerated electrons can recombine with different components of the DSC. A scheme with the different recombination pathways is presented in Figure 2.2. The main transport and recombination processes and their associated time constants are displayed in Table 2.1.

The kinetics of the internal processes of a DSC determine its performance. If the injection from the excited dye to the mesoporous layer is not fast enough, the excited dye molecule will return to its ground state and no electronic injection from the dye to the TiO_2 mesoporous layer will occur (7). The injected electrons in the mesoporous layer have two main recombination pathways: the electrons can recombine directly with the oxidized dye

molecule (8) or they can recombine with the oxidized component of the redox couple (9). Regeneration of the dye must occur faster than recombination with oxidized dye molecules in order to prevent the former.

Table 2.1. Transport and recombination reactions in a DSC with their respective time constants. The time constants were summarized in the work of Hagfeldt *et al*[11], assuming a ruthenium sensitizer and the I^-/I_3^- redox couple.

(1)	Photoexcitation	$S^0 + h\nu \rightarrow S^*$
(2)	Electron injection ($\approx 10^{-11}$s)	$S^* \rightarrow S^+ + e^-(TiO_2)$
(3)	Electronic transport ($\approx 10^{-3}$s)	$e^-(TiO_2) \rightarrow e^-(TCO)$
(4)	Dye regeneration ($\approx 10^{-6}$s)	$2S^+ + 3I^- \rightarrow 2S^0 + I_3^-$
(5 and 6)	Diffusion and regeneration of the redox couple	$I_3^- + 2e^-(Counter\ electrode) \rightarrow I^-$
(7)	Relaxation ($\approx 10^{-8}$s)	$S^* \rightarrow S^0 + h\nu$
(8)	Recombination with the dye ($\approx 10^{-4}$s)	$S^+ + e^-(TiO_2) \rightarrow S^0$
(9)	Recombination with the redox couple ($\approx 10^{-2}$s)	$2e^-(TiO_2) + I_3^- \rightarrow 3I^-$
(10)	Recombination from the bare FTO	$2e^-(TCO) + I_3^- \rightarrow 3I^-$

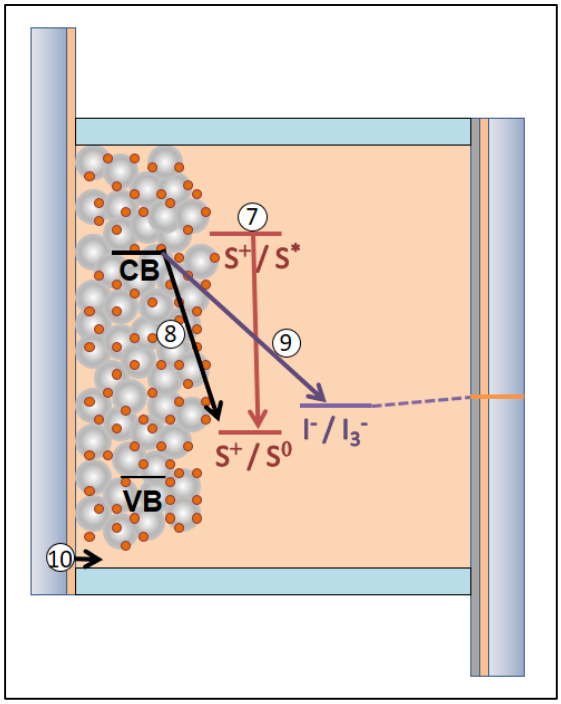

Figure 2.2. Recombination pathways in a DSC.

Due to the similar value of time constants between transport through the mesoporous layer and recombination between the electrons in the mesoporous layer and the redox couple in the electrolyte solution, this process represents the main charge loss in a DSC, especially near the open circuit potential. Finally, the electrons that reach the TCO could still recombine with the electrolyte solution (10). This last recombination pathway is particularly important at low potential values. A blocking layer should prevent this recombination to happen. There are several components in a DSC and the pathway to improve its performance and stability relies in a complete understanding of the processes inside the cell and the role each of these components have in them.

2.1.1 Working electrode substrate

The working electrode substrate in a DSC should be transparent so most of the light can penetrate into the mesoporous layer and also has to be a good electrical conductor, such that

the electrons that reach the working electrode can be collected. Working electrodes are usually made of glass with a layer of a transparent conductive oxide. Indium tin oxide (ITO) and fluorine-doped tin oxide (FTO) are usually employed. Although ITO has a higher transmittance at the same electrical conductivity as compared to FTO, its sheet resistance increases with higher temperatures[44]. Additionally, indium is a rare and expensive metal. Hence, FTO is mostly preferred. Plastic has been widely studied as an alternative to produce flexible substrates. This allows producing flexible DSCs, that can be widely used in many applications. However, a plastic substrate is thermally unstable during the sintering processes of the mesoporous layer[6].

2.1.2 Compact layer

A mesoporous TiO_2 film can lead to the formation of some voids between the TiO_2 nanoparticles and the FTO glass interface. The existence of these voids in the photoelectrode makes it possible for the electrolyte or hole conductor to permeate through the mesoporous layer and make contact directly with the conductive substrate, inducing recombination and decreasing the overall performance of the device. Therefore, controlling the interface between the FTO and nanocrystalline TiO_2 layers is essential for the formation of efficient DSCs[45]. The primary method to decrease reduction of electrolyte at the TCO surface is TCO surface passivation. A thin and compact TiO_2 film between the FTO and mesoporous TiO_2 layer has been extensively used as effective passivation layer (or hole blocking layer) in the DSC due to its high transparency, chemical stability, and suitable work function with FTO and nanocrystalline TiO_2 layer[46]. The presence of the compact layer increases DSCs performance by reducing electrical loss from recombination at the TCO-electrolyte. In addition to increasing the shunt resistance of the device, implementation of the blocking layer

has the added benefit of decreasing the series resistance by improving the electrical contact between the TiO_2 photoelectrode and the TCO surface[45,47–53]. In solid-state DSCs, it has been demonstrated that the FTO substrates must be covered by a thin blocking layer of titanium dioxide in order to prevent efficiency loss due to electron transfer to the hole-conducting medium from the FTO[45]. For DSCs, the blocking layer thickness must not exceed certain values (typically 300 nm) in order to prevent the layer from acting as a charge trapping site[49]. In ssDSCs, the blocking layer is usually thinner (100-200 nm)[54,55].

2.1.3 Mesoporous layer

The mesoporous layer is the backbone of the DSC. It provides the area on which the dye molecules will attach and the pathway over which the electrons will travel to the FTO to be finally collected. The most important processes inside the DSC are related with the mesoporous layer, such as injection and transport of carriers and most of the recombination processes. In the DSC, the photoanode needs to exhibit an extremely large surface to multiply the available area for dye anchoring. The pores of the electron-conducting network need to be large enough to allow ion diffusion of a solution-based electrolyte or pore infiltration by a solid-state hole conductor. Furthermore, the porous network has to offer direct percolation paths for the extraction of charges. Thus, an idealized photoanode morphology should be mesoporous (i.e., exhibit porosity on the 2-50 nm length scale), bicontinuous and offer sufficiently high charge-carrier transport[20,56]. Different semiconductor metal oxides have been studied for their use in DSCs, including TiO_2[23,24], ZnO[31,57–60], SnO_2[61], Nb_2O_5[62,63] and Ta_2O_5[63]. Important physical properties of the materials include the energetic position of the conduction band, the nature of the acceptor levels, presence of electron traps both at the surface and in the bulk, and charge transfer kinetics to the solution and the oxidized dye[64].

The most commonly used semiconductor material is TiO_2 since it possesses properties such as an excellent thermal and chemical stability and it is non-toxic. Other benefits include its cost-effectiveness and abundance. The common crystalline form used in solar cells is the anatase form since it is easiest to prepare as a nanomaterial and it has also been reported to have a higher electron conductivity compared to the rutile form[6].

2.1.4 Scattering layer

Light scattering is a method that has been employed in DSCs for optical absorption enhancement. The basic idea of a light scattering method is to confine the light propagation and extend the traveling distance of light within the photoelectrode film so as to increase the opportunity of the photons to be absorbed by the dye molecules and, in this way, to enhance the light harvesting efficiency of the photoelectrode as well as the conversion efficiency of the solar cells. In conventional DSCs, large TiO_2 particles with sizes comparable to the wavelength of visible light are used as scatterers by either being mixed into the nanocrystalline film to generate light scattering or forming a scattering layer on top of the nanocrystalline film to reflect the incident light[65,66].

2.1.5 Dye

The mesoporous layer has to be sensitized since it does not absorb visible light due to its large bandgap. The photosensitizer absorbs the solar radiation and injects electrons into the conduction band of the oxide substrate. A sensitizer should have strong light absorption in the visible and near infrared region for efficient light harvesting; good solubility in organic solvents for facile deposition from stock solutions in few hours; presence of suitable peripheral anchoring ligands such as -COOH to promote the effective interaction of the dye with the oxide surface and thus the coupling of donor and acceptor levels; suitable position

of the HOMO and LUMO levels of the dye molecule to permit quantitative injection of charges from the electronically excited state and good thermal and chemical stability to retain the chemical identity over repetitive redox cycles[11,64,67]. Thousands of small, medium and large sized molecules have been examined as potential candidates. In addition to organic molecules, coordination complexes of transition metals with polypiridine or porphyrin ligands have been studied[67]. The highest efficiency DSC reported to date employed co-sensitization with two different dyes in order to increase absorbance of the incident light, improving in this way the attainable current in the DSC[28]. In the case of solid-state DSCs, the mesoporous layer has to be thinner than for regular DSCs to prevent high recombination. It is for this reason that organic sensitizers with high extinction coefficient are usually employed[6,20,68].

2.1.6 Electrolyte solution

The electrolyte solution plays a very important role in the DSC by facilitating the transport of charge between the working and counter electrodes. Usually a non-aqueous organic solvent is employed to dissolve the electron mediators. Cations and additives are usually dissolved into the electrolyte solution in order to optimize the performance of the DSC.

Organic Solvents

An organic solvent is used to dissolve redox mediators and various additives for the preparation of DSCs and to help charge transfer. Solvents used in electrolytes can affect charge dissociation, separation and transfer, as well as the photovoltaic performance[67,69]. The solvent should be stable in the potential range where the cell operates, it should not interact with the dye-metal oxide linkage, and should not react with spacer/sealant materials[64]. Nitrile solvents such as acetonitrile, 3-methoxypropionitrile and valeronitrile, as well as esters such

as ethylene carbonate and propylene carbonate are preferred as solvents in DSCs as they offer a wide range of electrochemical stability and good solubility for redox mediators and the various additives used in the electrolyte[64,67]. The ideal electrolyte solvent is one that has very low viscosity, negligible vapor pressure, high boiling point and high dielectric properties[67].

Cations

Cations such as Li^+ as counter ions in the electrolyte play an important role in DSCs. Upon light illumination of a dyed mesoporous TiO_2 film, the injected electrons accumulate in the conduction band of TiO_2 and the cations in the electrolyte become adsorbed or intercalated in the TiO_2 film for charge compensation (Figure 2.3).

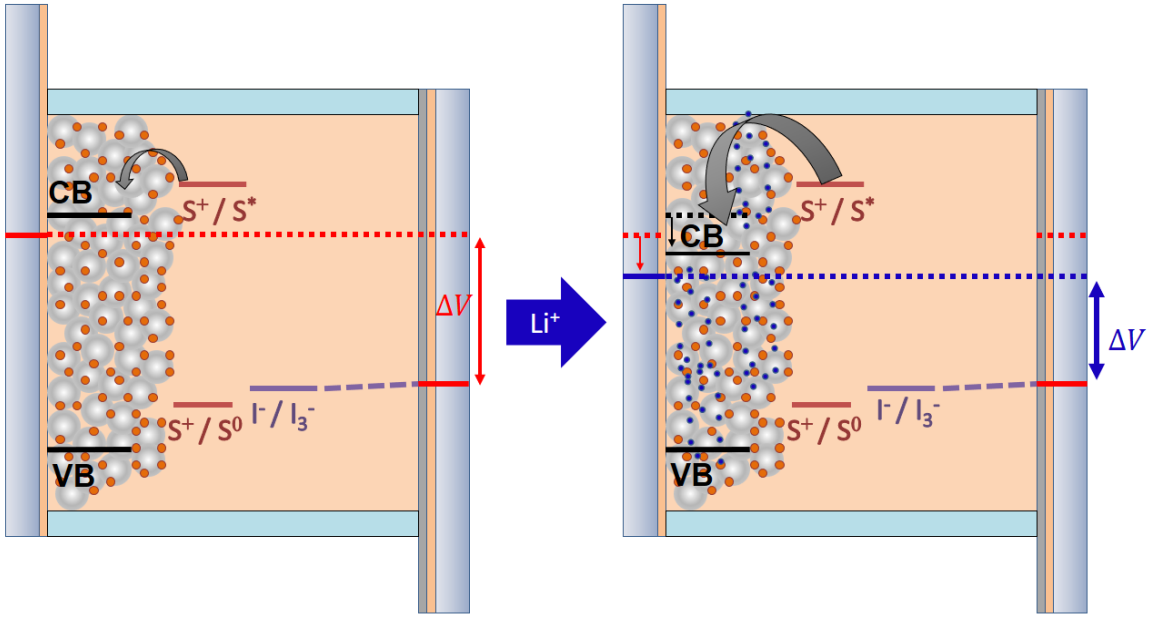

Figure 2.3. Movement of the TiO_2 band edges due to addition of Lithium cation. The change in potential and injection is highlighted. In the figure, the blue dots represent lithium cations, the red and blue lines represent the Fermi level at the contacts.

As compared to cations of large size, a small sized cation can easily be adsorbed into the TiO_2 surface, which results in a large potential drop. Due to the movement of the TiO_2 band

edges to lower energy, the driving force of the charge injection from the excited dye molecules to TiO_2 increases, resulting in a large injection efficiency and thus a large photocurrent. On the other hand, cation adsorption can affect the open-circuit potential due to the fact that the voltage is influenced by the position of the TiO_2 band edges and the redox potential of the electrolyte[64,67,70,71].

Additives

In DSC electrolytes, it has been found that the device performance can improve with nitrogen-containing heterocyclic compounds such as *tert*-butylpyridine (*t-BP)*. The *tert*-butyl pyridine adsorbs to active surface sites of the mesoporous layer and blocks electron transfer to the electrolyte solution (Figure 2.4).

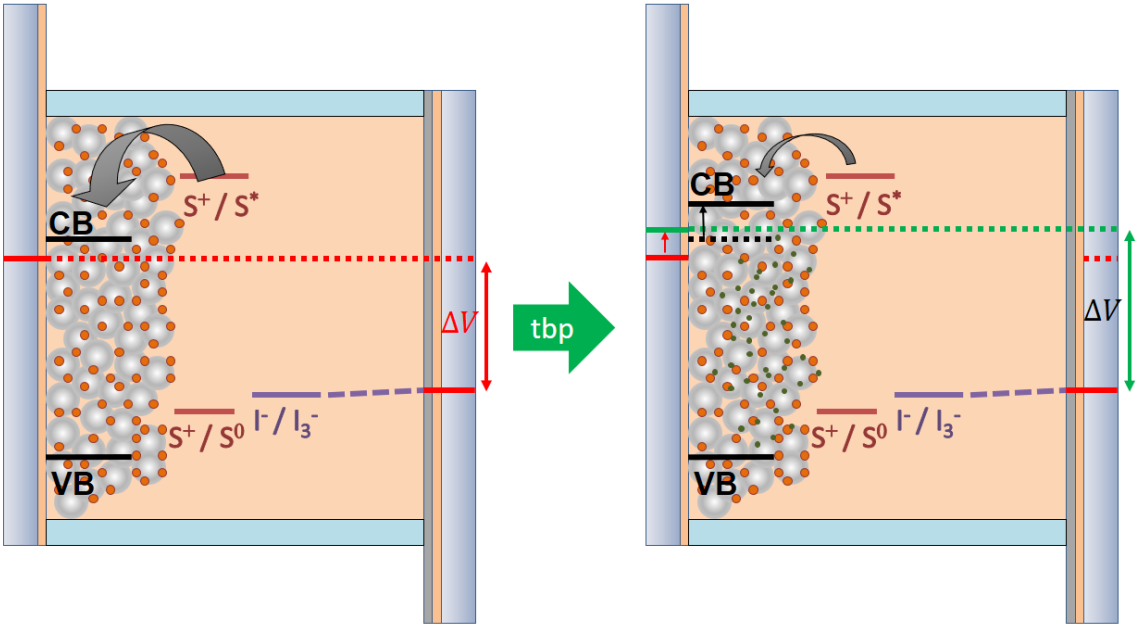

Figure 2.4. Movement of the TiO_2 band edges due to addition of tbp. The change in potential and injection is highlighted. In the figure, the green dots represent tbp molecules.

A similar effect was found for a large amount of nitrogen-containing heterocyclic compounds such as pyridine derivatives, benzimidazole derivatives, triazole derivatives, pyrazole

derivatives and imidazole derivatives. The smaller the size of the derivatives used in the electrolytes, the higher the open circuit potential (V_{oc}) of the corresponding cells, due to better effective adsorption on TiO_2. In addition, the increase in V_{oc} can also be explained by the movement of the TiO_2 band edges to higher energy due to the adsorption of the additives. The band edges of the TiO_2 electrode can move to higher energy also upon the addition of basic derivatives (Figure 2.4)[67,72].

Electron mediators

An electron mediator is a key material in an electrolyte, and its function is to reduce dye cations anchored on the surface of the semiconductor, and carry electrons from the counter electrode to the dyed semiconductor in DSCs. It should have a large solubility in the solvent and should be stable. Its redox potential should be at a higher energy level (more negative value) than that of the dye so that the oxidized dye can be reduced. The rate of reduction of the dye cation by a redox couple should be higher than the rate of recombination of the dye cations with electrons injected into the semiconductor. Moreover, the charge recombination should be slow to avoid recombination between electrons in the semiconductor and the oxidized part of a redox couple in the electrolyte before electrons transfer to the external circuit. In the DSCs, the open-circuit voltage is determined by the difference between the Fermi energy level of the illuminated semiconductor and the redox potential of the redox couple. A favorable redox potential of an electron mediator is expected to achieve a high open-circuit voltage while having a sufficient driving force for the reduction of oxidized dye molecules. Traditionally, a triiodide/iodide redox couple has been the common choice in DSCs with high conversion efficiencies, since it provides fast dye regeneration and shows slow recombination kinetics. Nevertheless, this couple has some disadvantages: a significant

portion of the visible light is screened from the sensitized TiO_2 electrode due to the absorption of the triiodide with high concentration in the electrolyte, its low redox potential limits the open-circuit voltage, and its corrosiveness to most metals prevents the use of a grid to collect current in large modules[36,40,41,64,67]. There have been attempts aimed at finding different redox couples, either to optimize the cell voltage and/or to improve the regeneration kinetics. Feldt et al proposed that an organic dye with high extinction coefficient and bulky ligands could help to prevent charge recombination between one-electron outer-sphere redox couples and electrons in the mesoporous layer and the FTO[32]. This discovery allowed the development of alternative redox couples instead of iodie/triiodide. Alternative redox couples based on cobalt or copper complexes have been studied with promising results[22,30–43]. These redox couples exhibit a redox potential located at lower energy levels (more positive values) than that for iodide/triiodide couple (Figure 2.5), increasing the attainable photovoltage in the DSC and are less aggressive towards metallic conductors than iodine[11,22,30,32,33,35,37,39,40].

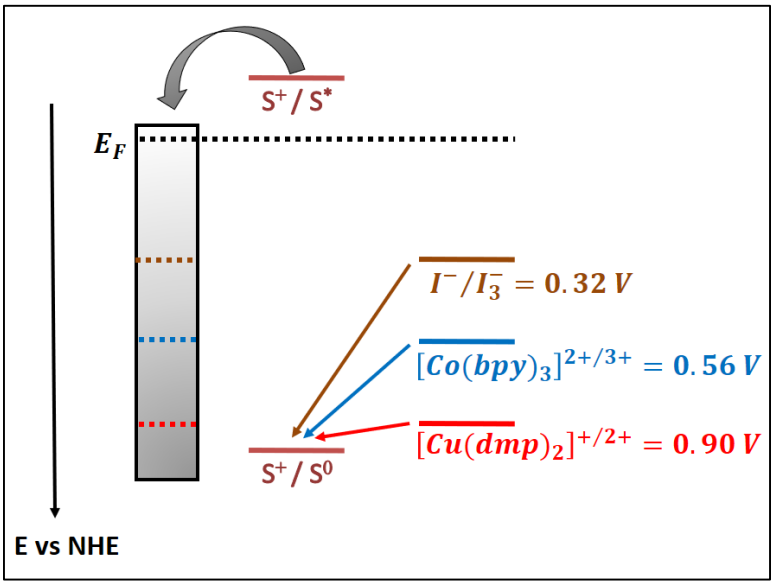

Figure 2.5. Energetic representation of the redox potential of I^-/I_3^-, $[Co(bpy)_3]^{2+/3+}$ and $[Cu(dmp)_2]^{+/2+}$ redox couples against a Normal Hydrogen Electrode (NHE)[31,32,38].

Due to the bulky nature of some of these redox couples, they may present mass transport limitation, particularly in the mesoporous layer, so specific dyes and DSC designs have to be employed to obtain high efficiency solar cells.

2.1.7 Counter electrode

To balance the charge and regenerate the key components, the oxidized form of the mediator needs to be reduced by the electrons flowing through the external circuit passing through the counter electrode. To reduce losses, the counter-electrode material should show good electrocatalytic properties. Best performance and long-term stability has been achieved with nanoscale Pt clusters. Pt can be deposited using a range of methods such as electrodeposition, spray pyrolysis, sputtering and vapor deposition[11]. As an electrode material, Pt shows excellent chemical stability and very low overpotential for the tri-iodide reduction reaction. There have been a number of studies on alternative counter electrodes for DSCs. Different forms of carbon including graphite, pyrolytic carbon, carbon black, single and multiwalled carbon nanotubes and even graphene have been proposed as alternatives to platinum[11,67]. Conductive polymers have also been studied as counter electrodes since they present many interesting properties such as flexibility, transparency and affordability. Among them, poly(3,4-ethylenedioxythiophene) (PEDOT) is known to be a potential replacement for platinum in DSCs, since its synthesis is extremely facile and amenable to scale up and it can be electropolymerized in acetonitrile and water solutions[11,73,74].

2.2 Solid state DSCs

A clear disadvantage of the DSCs is the liquid electrolyte, which makes them difficult to encapsulate for long-term stability in solar modules. An alternative of DSC is the solid-state DSCs, where the liquid electrolyte is replaced by a molecular hole transport material or an

inorganic p-type semiconductor[34,75]. Although the basic structure and working principles are very similar to those presented for the DSCs, there are differences in the design, dye regeneration and hole transport in the hole conductor. A scheme of the solid-state DSC is presented in Figure 2.6.

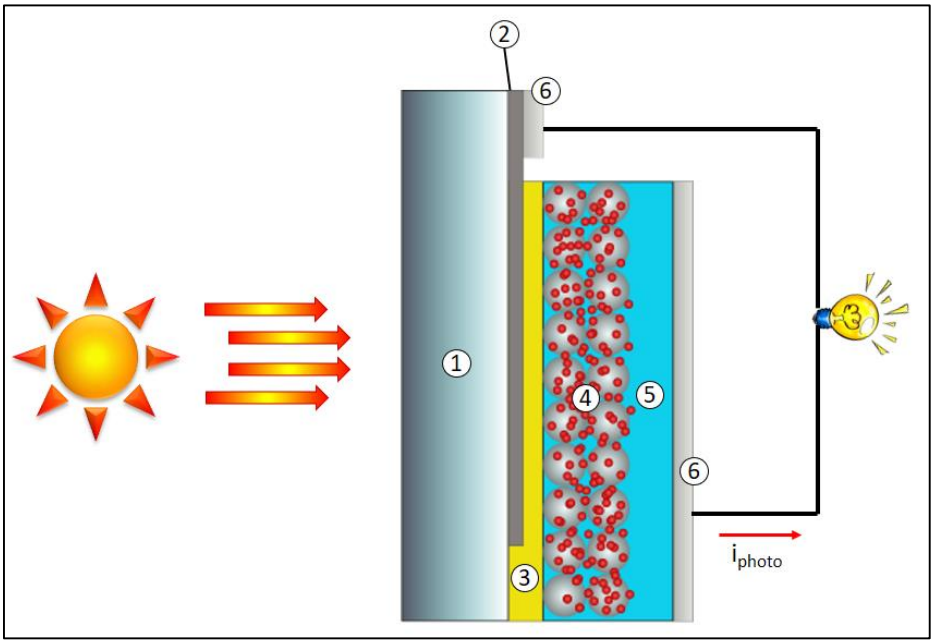

Figure 2.6. Representation of a solid-state DSC. The main components are highlighted: (1) Glass substrate, (2) FTO film, (3) blocking layer, (4) mesoporous sensitized layer, (5) hole conductor and (6) metallic contacts in the electrodes.

Generally, the device consists of a partially etched conducting glass substrate ((1) and (2)), a compact TiO_2 dense film prepared by spray pyrolysis (3) to avoid short circuits between the FTO substrate and hole transport material (HTM) layer, a mesoporous film, usually TiO_2, anchored with dye molecules (4), a HTM layer (5) and metallic contacts to the working and counter electrode (6), usually deposited by evaporation[76]. The cell mechanism using HTM is analogous to liquid DSCs. After dye excitation and electron transfer to the conduction band of TiO_2, the ground state of the dye is regenerated by the HTM: electrons from the highest

occupied molecular orbital (HOMO) of the HTM regenerate the ground state of the dye molecules instead of the redox couple of the electrolyte. The oxidized HTM material is then reduced at the counter electrode. The main difference relies on the kind of transport between the electrodes. In the cell using HTM, the transport is typically electronic, in comparison to ionic transport in the DSC using liquid or polymer electrolyte.

The following equations show the most important reactions involved in a DSC using a HTM.

$$S^* \rightarrow S^+ + e^-(TiO_2) \tag{2.1}$$

$$S^+ + HTM \rightarrow S + HTM^+ \tag{2.2}$$

$$HTM^+ + e^-(Metallic\ contact) \rightarrow HTM \tag{2.3}$$

$$S^+ + e^-(TiO_2) \rightarrow S \tag{2.4}$$

$$e^-(TiO_2) + HTM^+ \rightarrow HTM \tag{2.5}$$

(2.1), the excited dye molecule, *S**, injects an electron into the TiO_2 mesoporous layer. (2.2) the oxidized dye molecule, S^+, is generated by the hole transport material and the *HTM* becomes oxidized (HTM^+). (2.3) The hole in the HTM is transported to the counter electrode where it is regenerated. Processes (2.4) and (2.5) represent the main pathways of recombination, where an electron in the mesoporous layer can recombine either with the oxidized dye molecule (2.4) or with the hole transport material (2.5). In the solid-state DSC, the charge transfer reactions at the dye-sensitized nanocrystalline TiO_2-HTM interface play a key role in determining the overall solar cell efficiency[77,78]. In general, the performance of a ssDSC may be limited by different reasons. Since a hole conductor is employed to fill the mesopores, poor wetting and bad pore filling of the mesoporous network leads to incomplete interfacial contact between the dye attached to the TiO_2 electrode and the HTM, which leads

to low performance of the ssDSC[34,76,78,79]. The recombination in ssDSCs has been reported to be 100 times faster than in DSCs[54,56,76,78,80], thus recombination becomes the major feature determining the lower efficiency of the solar cell. The performance of the solar cell can also be limited by low conductivity of the hole transport material[34,76,78]. The short diffusion length does not allow the use of thick TiO_2 layers in ssDSCs, limiting the available surface for dye loading and, therefore, light absorption and current. All these limitations have led to design ssDSCs with interfacial blocking treatments, mesoporous layer thicknesses between 2-5 µm and high extinction coefficient dyes to improve ssDSC performance[20,54,76,79]. These design strategies have already led to ssDSCs with efficiencies of 7.2%[37,81].

2.2.1 Hole transport material

An appropriate HTM for fabricating ssDSCs must satisfy several requirements: (1) It must be able to transfer holes from the sensitizing dye after the dye has injected electrons into the TiO_2, that is, the upper edge of the valence band of p-type semiconductor must be located above the ground state level of the dye; (2) efficient deposition within the mesoporous TiO_2 film, good pore filling ability, and stable interfacial contact with the dye-TiO_2; (3) sufficient hole mobility; (4) thermal and photochemical stability and (5) no strong absorption in the visible spectrum to avoid competition with dye molecules[20,34,77,78,82]. In principle, all materials with p-type semiconducting behavior, capable of accepting holes from the dye cation, are potential candidates to replace the liquid electrolyte in DSSC. These materials can be crystalline inorganic salts, such as CuI and CuSCN, or organic molecular solids and polymers such as Spiro-OMeTAD (Figure 2.4 (a)). Plastic materials, when properly modified, combine the excellent processing advantages and mechanical properties of conventional polymers with the desired electrical, optical, electronic and magnetic properties

of metals and semiconductors[77]. In 1998, Bach and Grätzel et al. reported the first efficient ssDSC with amorphous organic HTM (spiro-OMeTAD)[78,83] (Figure 2.4). Thereafter, the efficiency of spiro-OMeTAD-based ssDSCs has increased dramatically through dye development and TiO_2 modification[80,84]. Other studies have described improvement through the addition of additives to spiro-OMeTAD, such as 4-*tert*-butylpyridine (*t*-BP) to increase the V_{oc} and cobalt complexes as *p*-dopant to enhance hole conductivity[20,82].

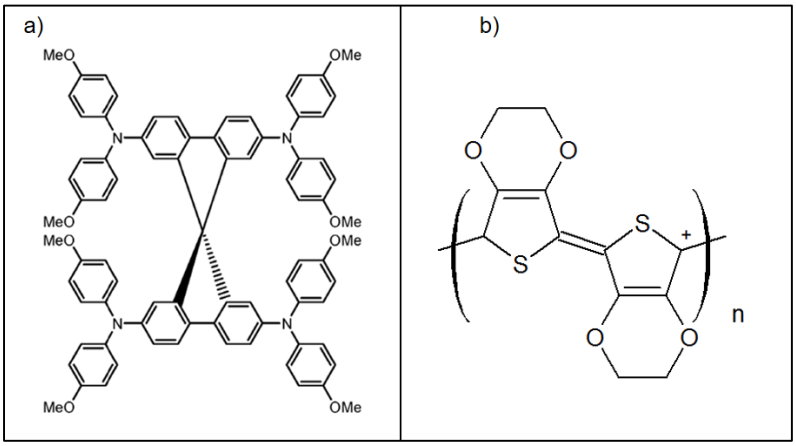

Figure 2.7. Chemical structures of (**a**) Spiro-OMeTAD[68] and (**b**) PEDOT polymer[84].

Although spiro-OMeTAD is the most favorable organic HTM for fabricating ssDSCs, it has some disadvantages such as low hole mobility and high fabrication cost. Consequently, conjugated polymers (CPs) have been intensively investigated as alternative HTM due to their thermal stability, high conductivity, good solubility as well as tunable optoelectronic properties. These photovoltaic devices combine the distinctive features of inorganic semiconductor TiO_2 such as mechanical and chemical stability, with the unique properties of polymer HTMs such as easy film formation and adjustable functionality by molecular design[20,76–78]. Some conjugated polymers include polyaniline, poly(3-alkythiophene)s, triarylamine-based polymers and poly(3,4-ethylenedioxythiphene). Among PT derivatives, poly(3,4-ethylenedioxythiophene) (PEDOT) (Figure 2.4 (b)) has recently been described as

a remarkably stable, highly conductive material, possessing very pronounced electrochromic properties. PEDOT is known to be a potential replacement for Pt when used as the catalytic layer on the counter electrode, and may also be used as the hole transport material in DSCs[73,74,76,82,85,86].

CHAPTER 3

Characterization techniques in Dye-sensitized solar cells

3.1 Standard solar spectrum and solar irradiation

The sun emits radiation resembling the spectrum of a blackbody at a temperature of 5670 K. The amount of solar power flux that reaches the outer atmosphere of the Earth is known as top-of-atmosphere (TOA) irradiance, and has a current accepted value of 1366 W/m^2 [87]. However, because of absorption and scattering by the atmosphere, the spectral distribution of solar radiation outside the atmosphere differs significantly from that on Earth's surface (Figure 3.1). To take into consideration the scattering of the radiation, the radiation of the sun is usually measured as global horizontal radiation, which is the sum of direct normal irradiance, diffuse horizontal irradiance and ground-reflected radiation. Direct normal irradiance refers to the irradiance that comes in a direct line from the sun, whereas diffuse horizontal irradiance is the radiation that is scattered by molecules, aerosols and clouds. The diffuse radiation composes about 10% to 20% of the total global radiation under clear sky conditions[87]. The ground-reflected radiation is the radiation from the sun which is reflected back into the atmosphere after striking the Earth. However, because ground reflected radiation is commonly insignificant compared to direct and diffuse radiation, it is usually omitted. Since a high portion of the solar radiation is composed of visible and infrared radiation, a good solar device must interact strongly with this part of the spectra.

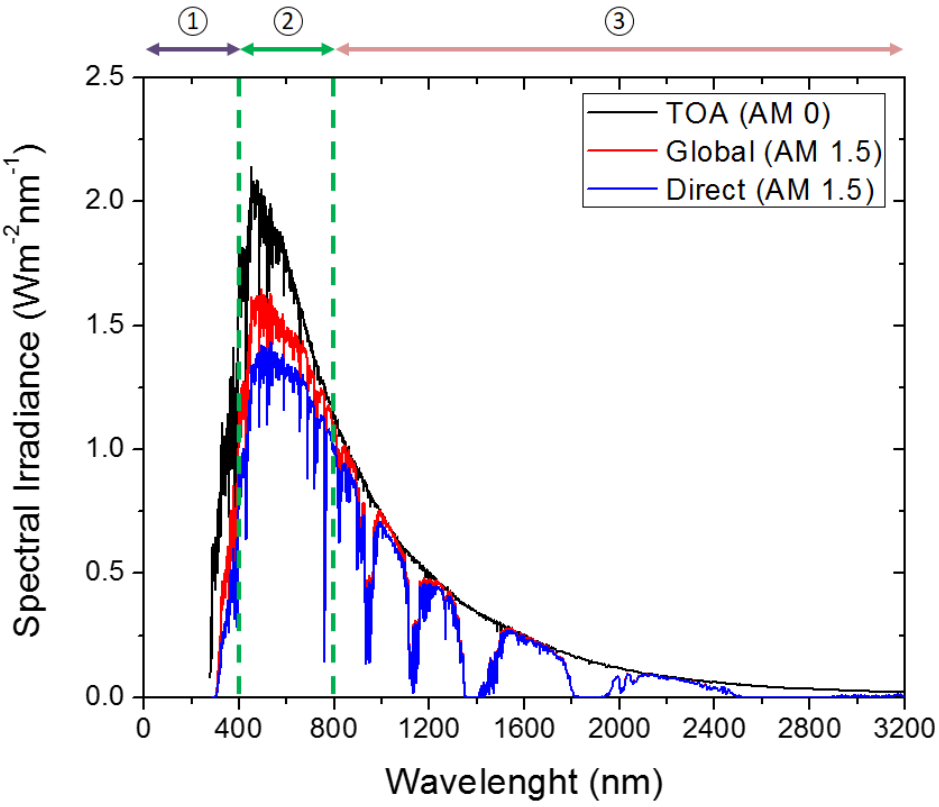

Figure 3.1. Solar spectrum for top-of-atmosphere (AM 0), direct and global irradiance (AM 1.5). Ultraviolet (1), visible (2) and infrared region (3) are highlighted[87].

Since the efficiency of a solar cell is sensitive to the intensity of solar radiation received and this latter depends on the path length the radiation has to travel through the atmosphere to reach the device, a standard value has to be used in order to properly compare solar cell devices. The Airmass is defined as the relative path length direct solar beam radiance has to go through the atmosphere before reaching Earth's surface. When the sun is directly above a sea-level location the path length is defined as airmass 1 (AM 1.0). The standard value used for efficiency measurements of solar cells is AM 1.5 G. The value of 1.5 represents an optical path length 1.5 times longer than for AM 1.0, and corresponds to an angle of 48.2° with respect to the position of the sun at AM 1.0. The G stands for global radiation. The integrated irradiance of this spectrum per unit area is 1000 W/m^2, also known as 1 sun illumination.

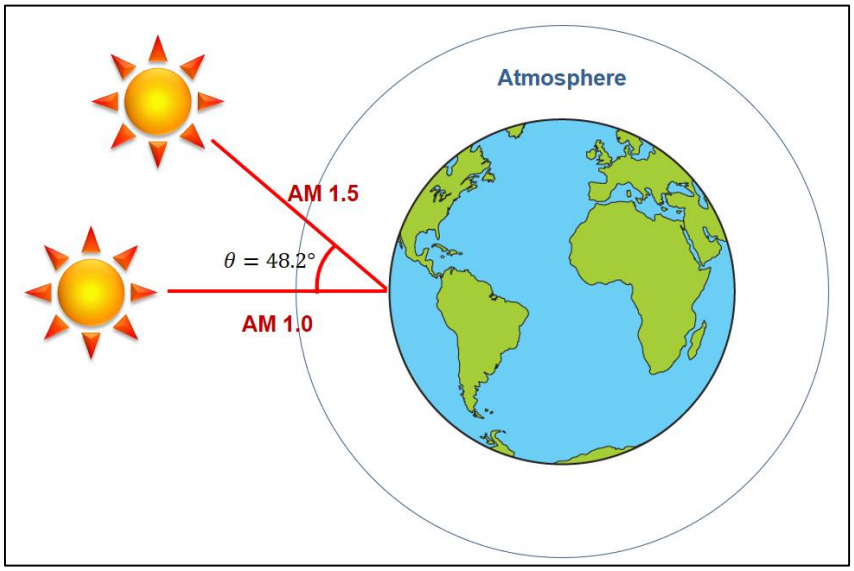

Figure 3.2. Schematic representation of AM 1.0 and AM 1.5.

There are several processes that occur simultaneously inside a solar cell, such as absorption of light, injection of charge to the mesoporous layer, electronic transport through the mesoporous layer, ionic diffusion in the electrolyte solution, charge collection and charge recombination, among others. Several different characterization techniques have been proposed in order to have a better understanding of the mechanisms that determine the performance of DSCs.

3.2 Current-potential curves

The performance of a solar cell is generally described through the measurement of the current-voltage (or current density-voltage) characteristics of the device, i.e., the J-V curve.

$$J = J(V) \tag{3.1}$$

where J is the DC electrical current density flowing through the device and V is an externally applied bias. The universal shape of a J-V curve of a solar cell under illumination (Figure

3.3) is a consequence of the balance between two opposing mechanisms: (1) light-induced charge separation and subsequent current generation and (2) loss processes (recombination, or dark current)[23,25]. When a forward bias is applied, accumulation of electrons within the negative photoanode occurs. This leads to an increase of current in the opposite direction to the current generated by the cell. At sufficiently high bias, the two currents will cancel, corresponding to open-circuit conditions. The potential at which this occurs is known as open circuit potential, V_{oc}. At zero bias, which corresponds to short circuit conditions, the cell will produce its maximum current, the short circuit current density, J_{sc}. Both the V_{oc} and the J_{sc} represent the maximum potential and current density the solar cell can deliver under specific measurement conditions. The solar cell will only generate power if it produces current at non-zero bias[23,25,64,88].

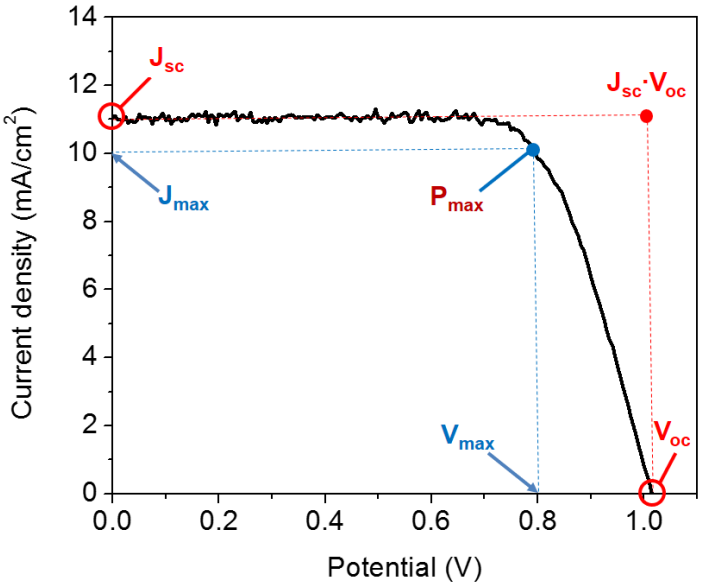

Figure 3.3. General shape of a J-V curve. The main J-V parameters are displayed: short circuit current density, J_{sc}, open circuit potential, V_{oc}, maximum power point, P_{max}, current density and potential at the maximum power point, J_{max} and V_{max} respectively, and the product between the short circuit current density and the open circuit potential, J_{sc}·V_{oc}.

The point at which the cell produces its maximum power is known as maximum power point, P_{max}, with their corresponding photocurrent (J_{max}) and photovoltage (V_{max}). The relationship between P_{max} and the product of J_{sc} and V_{oc} is known as the fill factor (*FF*)[11,64,88]:

$$FF = \frac{P_{max}}{J_{SC} * V_{OC}} \tag{3.2}$$

The FF is basically the ratio between the area of the red and blue rectangle in Figure 3.3. Its value goes from 0 to1 and is an indirect way to predict the shape of a J-V curve. If the fill factor is high, the drop in current at high voltage is delayed, and we can extract the electrons at high voltage while the current is still close to J_{sc}[88]. The overall sunlight-to-electric-power conversion efficiency, η, of a DSC is given by the following expression[11]:

$$\eta = \frac{P_{max}}{P_{in}} = \frac{J_{SC} V_{OC} FF}{P_{in}} \tag{3.3}$$

where P_{in} is the intensity of the incident light. The four values J_{sc}, V_{oc}, FF and η are the key performance parameters of the solar cell[11].

3.3 Incident photon-to-current conversion efficiency (IPCE)

Another fundamental measurement of the performance of a solar cell is incident photon-to-current conversion efficiency (IPCE). The IPCE value corresponds to the photocurrent density produced in the external circuit under monochromatic illumination of the cell divided by the photon flux that strikes the cell[11]. The IPCE as a function of wavelength can be calculated from:

$$IPCE = \frac{J_{SC}(\lambda)}{q\phi(\lambda)} = 1240 \frac{J_{SC}(\lambda)[Acm^{-2}]}{\lambda[nm] P_{in}(\lambda)[Wcm^{-2}]} \tag{3.4}$$

where q is the elementary charge, $\phi(\lambda)$ is the spectral photon flux, $J_{sc}(\lambda)$ is the current density at each specific wavelength, λ is the illumination wavelength and $P_{in}(\lambda)$ is the power of the illumination at that wavelength. IPCE values provide practical information about the monochromatic quantum efficiencies of a solar cell[11,89]. The photocurrent measured under short circuit conditions, J_{sc}, is the integrated sum of IPCE measured over the entire solar spectrum:

$$J_{SC} = q \int_{\lambda_{min}}^{\lambda_{max}} IPCE(\lambda) \cdot \phi(\lambda) d\lambda \tag{3.5}$$

where λ_{min} and λ_{max} defines a wavelength range[88,89].

The IPCE can be expressed as the product of the efficiencies of three separate physical processes:

$$IPCE(\lambda) = \eta_{lh}(\lambda)\eta_{inj}(\lambda)\eta_{col}(\lambda) \tag{3.6}$$

Where $\eta_{lh}(\lambda)$ is the light-harvesting efficiency of the sensitized oxide layer, $\eta_{inj}(\lambda)$ is the efficiency of the electron injection from the sensitizer into the oxide and $\eta_{col}(\lambda)$ is the electron collection efficiency[88,89]. The value of $\eta_{lh}(\lambda)$ indicates how efficiently the adsorbed dye molecules harvest incident photons. It depends on the extinction coefficient of the dye and the transmittance of the FTO. The quantity $\eta_{inj}(\lambda)$ indicates the probability that an electron is generated in electronic states of the semiconductor as a consequence of the electron injection from the dye. It depends of the energetics of the dye and the mesoporous layer and on the regeneration efficiency for the dye. The final parameter $\eta_{col}(\lambda)$ is an indicator of the probability that a photogenerated electron reaches the collector substrate before it is lost by recombination[89].

3.4 Cyclic voltammetry

In general, an electric potential difference can be controlled between the working electrode and a reference electrode with a constant potential in an electrochemical cell. This cell potential is a measure of the energy available to drive charge transfer processes[90]. By driving the working electrode to more negative potentials, the Fermi energy of electrons is raised. Once the Fermi energy reaches a level high enough to transfer electrons into vacant electronic states of the oxidized species in the electrolyte, a flow of electrons from electrode to solution occurs, corresponding to a reduction or cathodic current. Similarly, the Fermi energy of the electrons can be lowered by imposing a more positive potential, and at some point electrons of the reduced species in the electrolyte will flow from the electrolyte solution to the electrode. This current is known as an oxidation or anodic current. The critical potentials at which these processes occur are related to the formal Nernst potential, $E^{0'}$, for the specific chemical substances in the system[90].

Assuming an electrochemical system with the following redox reaction:

$$Ox^{+} + e^{-} \leftrightarrow Red \tag{3.7}$$

where Ox^{+} and *Red* are the oxidized and reduced elements of an electrolyte solution and e^{-} represents the exchange of one electron. If a potential sweep is applied to the electrochemical system with only *Red* present in the solution, and the scan is started at a potential well negative of $E^{0'}$, only non-Faradic currents flow (Figure 3.4). When the electrode potential approaches $E^{0'}$ the oxidation of *Red* begins and a current starts to flow. As the potential continues to be swept more positive, the charge transfer rate increases, resulting in an increase of the current until the concentration of *Red* at the surface starts to decrease related to transport limitations, reaching a maximum value at E_{pa}, the potential at the anodic peak

current. Moving past this point the concentration gradient of *Red* keeps decreasing and the current decrease to a semi-stationary value. If the potential scan is then reversed and taking into account that Ox^+ has been forming at the surface of the working electrode at a constant rate, the reduction of Ox^+ starts occurring at values close to $E^{0'}$ This reversal current has a shape similar to that of the anodic peak for essentially the same reasons. The formal potential can then be obtained as the average value between the anodic and cathodic potential for a reversible process[90].

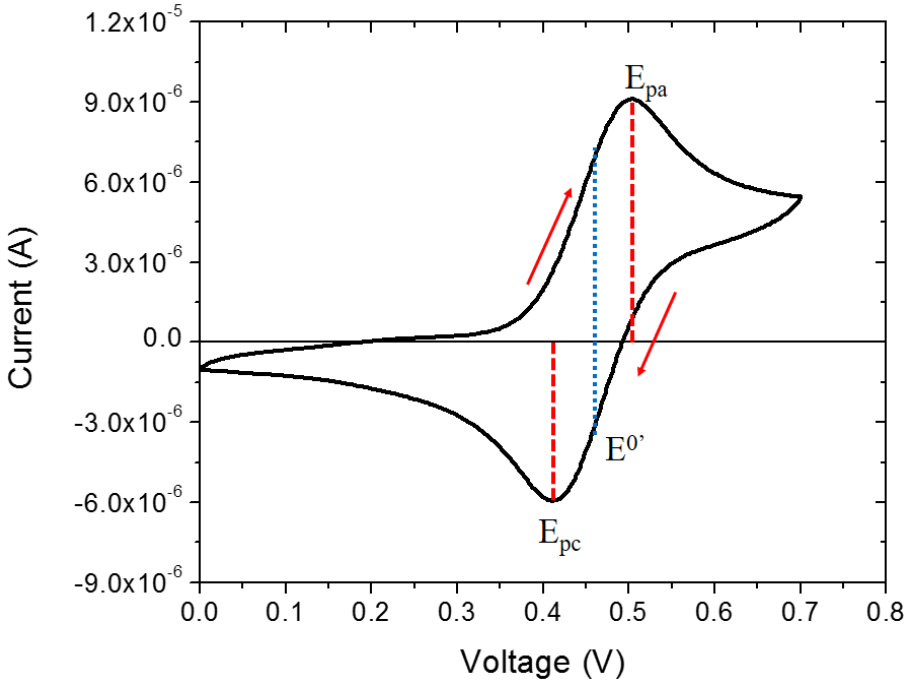

Figure 3.4. Example of a cyclic voltammogram. The potential at the anodic (E_{pa}) and cathodic (E_{pc}) peak current is displayed, along with the position of the formal potential ($E^{0'}$) and the direction of the potential sweep.

This sweep reversal method is known as cyclic voltammetry and is among the most widely practiced characterization techniques of all electrochemical methods[90].

3.5 Reverse bias measurements

Considering a positive current, when a reverse bias (positive potential) is applied to the working electrode of the cell, one of the following electrochemical reactions should take place at the FTO in the working electrode, depending on the electrolyte solution employed:

$$3I^- \rightarrow I_3^- + 2e^- \quad (3.8\ a)$$

$$[Co(bpy)_3]^{2+} \rightarrow [Co(bpy)_3]^{3+} + 1e^- \quad (3.8\ b)$$

$$[Cu(dmp)_2]^{+} \rightarrow [Cu(dmp)_2]^{2+} + 1e^- \quad (3.8\ c)$$

where $[Co(bpy)_3]^{2+/3+}$ represents a cobalt (II/III) bypyridine complex and $[Cu(dmp)_2]^{+/2+}$ represents a copper (I/II) dimethyl-phenantroline complex. If the voltage is large enough a maximum value of current is obtained. This saturation current density, J_{lim}, is related to the transport of the ionic carriers from one electrode to the other[60,91,92], and its value will depend on diffusion limitations of the oxidized species, since its concentration is lower than the reduced species. If a negative potential is applied to the cell, then the TiO_2 is no longer insulating, and an electrochemical reaction can take place in any part of the mesoporous layer[56,93]. In order to relate the limiting current with mass transport limitations through the mesoporous layer, the TiO_2 has to be electrochemically inactive so the redox species have to diffuse through the mesoporous layer to produce an electrochemical reaction. If a reverse bias is applied to a symmetric cell, where both electrodes are platinized and no mesoporous layer is present, the saturation current density can be employed to determine the diffusion coefficient of the oxidized species, D_{ox}, in the electrolyte solution, according to the following relationship:

$$D_{ox} = \frac{l}{2nFC_{ox}} j_{lim} \tag{3.9}$$

where n is the number of electrons involved in the electrochemical reaction at the electrode, F is Faraday's constant, C_{ox} is the concentration per volume unit of the oxidized part of the redox couple, assumed uniform along the cell array, and l is the distance between the electrodes[60,91,92].

3.6 Transient photocurrent measurements

Transient photocurrent measurements conducted at short circuit are employed to evaluate mass transport inside a DSC (Figure 3.5).

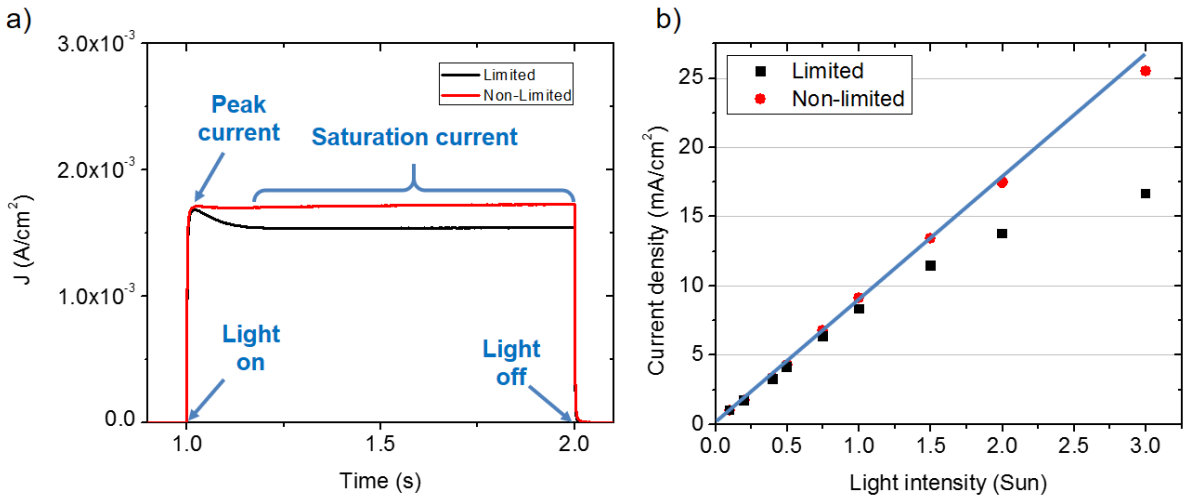

Figure 3.5. (**a**) Evolution of photocurrent during a transient photocurrent measurement. The peak current, saturation current and the moment where the light is turned on and off are highlighted. (**b**) Representation of the saturated current against light intensity. A line was added to show deviation from linearity. In both plots, an example of a mass transport limited and non-limited DSC is displayed.

The experimental procedure consists in monitoring the photocurrent of a DSC, initially in dark conditions, when illumination is applied to it. When a DSC is under equilibrium in the dark, the oxidized and reduced species in the electrolyte solution are equally distributed

inside the cell. When illumination is applied to the cell, charge is generated from the dye and the regeneration process from the electrolyte solution takes place. In an ideal DSC, the regeneration is efficient and the current is limited only by the photon flux. However, if the diffusion of the redox couple is slow, then the maximum attainable current in the cell will be limited by its diffusion coefficient inside the DSC[41,93–95]. A big difference between the peak current and the saturated current in a DSC is a consequence of mass transport problems inside the DSC. When plotting the current density against light intensity, a deviation from linear behavior is also an indication of mass transport limitations within DSCs. This effect increases under high light intensity conditions[41,93–95].

3.7 Voltage decay measurements

In an open circuit voltage decay measurement (OCVD), the DSC is illuminated under open circuit conditions until the potential is stable. The illumination is shut down and the evolution of potential over time is monitored. An example of an OCVD is displayed in Figure 3.6.

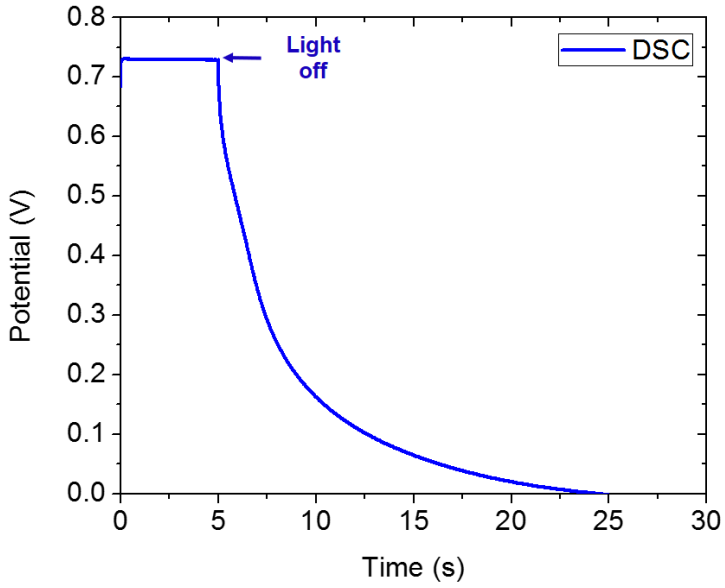

Figure 3.6. Open circuit voltage decay measurement.

For a DSC that is illuminated under open circuit conditions to establish a steady photovoltage and for which the illumination is interrupted, the cell voltage first decays rapidly and then more slowly as electrons escape from the mesoporous oxide by transfer to I_3^- ions or equivalent hole species[96–99]. The slowing down of the decay arises from the fact that electrons must be de-trapped before transferring to I_3^-, and as the quasi-Fermi level moves to lower energy, de-trapping slows down considerably. In the absence of a blocking layer, electron transfer via the substrate may cause the voltage to decay more rapidly, and it typically falls to zero after 10-20s.

Photovoltage decay plots can be used to derive the effective electron lifetime, τ_n, as a function of photovoltage[97,98]. It can be shown that τ_n is related to the gradient of the photovoltage decay by:

$$\tau_n = -\frac{k_B T}{q}\left(\frac{dU_{photo}(t)}{dt}\right)^{-1} \tag{3.10}$$

where k_B is the Boltzmann constant, T is the temperature and U_{photo} represents the photovoltage. In this way, the electronic lifetime can be obtained numerically or analytically by fitting the decay curve to a suitable function that can be differentiated. The photovoltage decay measurements become unreliable to determine electronic lifetime at low photovoltages, due to the influence of the back reaction at the substrate[96].

3.8 Charge extraction measurements

Whereas photovoltage methods measure the decay of free electrons, the charge extraction method can be used to determine the rate at which the total electron density decays. It involves illuminating the DSC at open circuit until a steady photovoltage is obtained. The illumination is then switched off so that the photovoltage begins to decay as the quasi-Fermi

level moves to lower energy. The cell is then switched to short circuit when a pre-determined photovoltage has been reached, and the resulting current is integrated over a suitable period (typically several minutes) to obtain the trapped charge (Figure 3.7). This experiment is repeated for several values of the photovoltage to obtain the density of trapped electrons, n_t, as a function of the photovoltage. The charge extraction method requires only that the electron collection efficiency approaches unity under short circuit conditions. The charge extraction method provides direct access to the electron density as a function of illumination intensity and decay time. The method also allows a direct correlation to be made between the photovoltage and the total electron density[67,99]. It is worth noting that the photovoltage decay method and the charge extraction method both become unreliable for deep states (low photovoltages). In the case of the charge extraction method, this is due to the fact that not all carriers will be extracted on the time scale of the measurement[96].

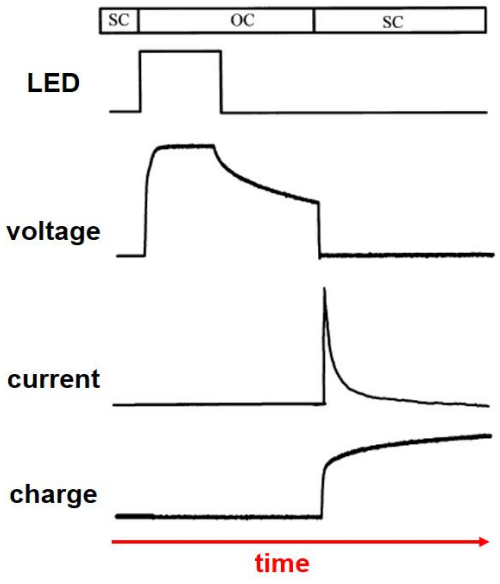

Figure 3.7. Open circuit (OC)/short circuit (SC) sequence showing the relationship between the illumination and the measurement of potential and charge in the charge extraction experiments[99].

3.9 Electrochemical impedance spectroscopy (EIS)

Direct current (DC) techniques do not provide any information about the internal dynamics of the photovoltaic device. Therefore, additional information can be obtained using time dependent and frequency dependent measurements. Electrochemical impedance spectroscopy (EIS) measurements provide a full picture of the processes determining the operation of DSCs, and this allows for a more fundamental study of the cells. EIS is normally measured using a small excitation signal (1 to 10 mV) to an electrochemical cell and measuring the current through the cell. This is done so that the cell's response is linear. In a linear system, the current response to a sinusoidal potential will be a sinusoid at the same frequency but shifted in phase. The system being measured must be at a steady state throughout the time required to measure or it will give inaccurate results. The impedance of a system can be expressed as[67]:

$$Z(\omega) = \frac{E_t}{I_t} = Z_0(cos\phi + jsin\phi) \qquad (3.11)$$

where Z_0 is a constant, E_t is the excitation signal, I_t is the response signal, ω is the radial frequency and ϕ is the phase shift. The expression for Z(ω) is composed of a real and imaginary part. If the real part is plotted on the X-axis and the imaginary part is plotted on the Y-axis of a chart, a Nyquist plot is obtained. In this plot the Y-axis is negative and each point on the Nyquist plot is the impedance at one frequency (Figure 3.9)[100]. The impedance of DSC can be described by an equivalent circuit model. The equivalent circuit is constructed by assigning equivalent circuit elements such as resistances and capacitors associated in series and/or parallel to represent the different process inside a DSC. Resistances usually represent charge transport in the materials and charge transfer across their interfaces, while

capacitors represent accumulation of charge at these interfaces. One of the most successful models to represent a DSC is the one proposed by Bisquert, Fabregat *et al* (Figure 3.8) [88,91,101,102].

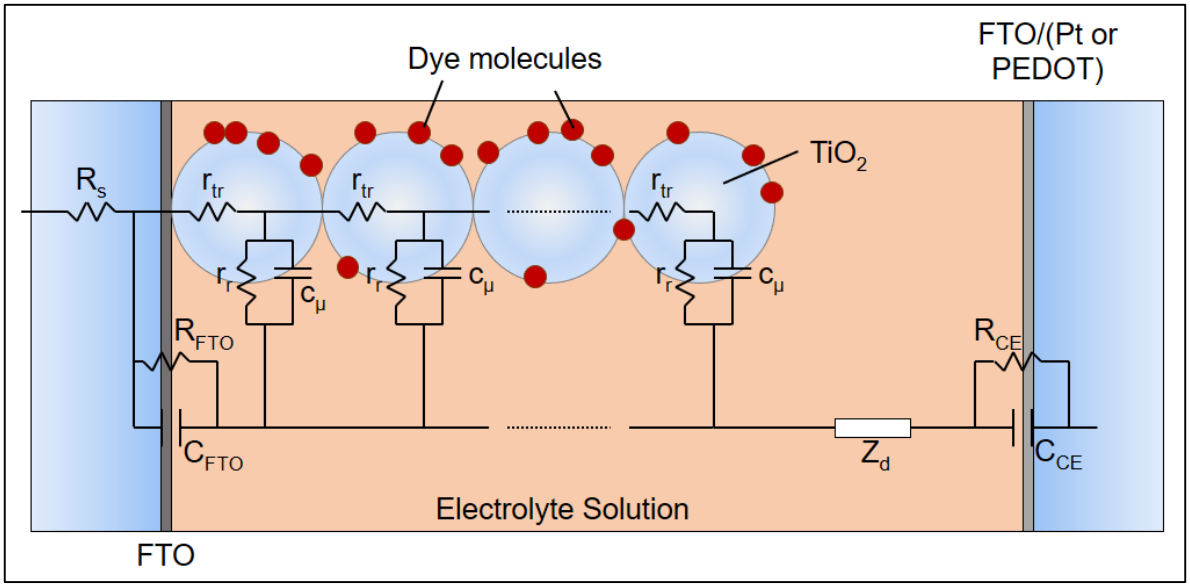

Figure 3.8. General equivalent circuit model used to fit impedance spectroscopy results for DSCs.

In Figure 3.8, R_S represents the series resistance of the FTO; R_{FTO} and C_{FTO} stand for the elements of resistance and capacitance for the recombination via the substrate uncovered by the TiO_2 nanoparticles; r_{tr} represents the resistance for electron transport along the metal oxide nanoparticles; r_r is the charge transfer resistance that exists to the process of recombination between electrons in the metal oxide and the redox species in the electrolyte solution (or dye); c_μ is the chemical capacitance; Z_d is the Warburg impedance of the diffusion of the redox species in the electrolyte solution; R_{CE} stands for the charge transfer resistance at the counter electrode/electrolyte interface and C_{CE} represents the Helmholtz capacitance at the counter electrode/electrolyte interface. The transfer function for this equivalent circuit is[91,101]:

$$Z(\omega) = \left(\frac{R_t R_r}{1 + i\omega/\omega_k}\right)^{1/2} coth\left[(\omega_k/\omega_d)^{1/2}(1 + i\omega/\omega_k)^{1/2}\right] \quad (3.12)$$

where $\omega_d = 1/R_tC_\mu$ is the characteristic frequency of diffusion in a finite layer, $\omega_k = 1/R_rC_\mu$ is the rate constant for recombination, ω is the angular frequency and $i = (-1)^{1/2}$. $R_t = r_tL$, $R_r = r_r/L$ and $C_\mu = c_\mu L$ where L is the thickness of the mesoporous layer. Particularly, the element Z_d accounting for diffusion of the redox species in the electrolyte can be expressed as[91,101]:

$$Z_d = R_d \frac{tanh\left[(i\omega/\omega_d)^{1/2}\right]}{(i\omega/\omega_d)^{1/2}} \quad (3.13)$$

where *Rd* represents the diffusion resistance associated with this process.

The different impedance components of the cell exhibit different time constants (characteristic frequencies) and therefore can be seen as separate impedance arcs in the complex plane plot of the cell impedance (Figure 3.9). This enables fractioning the total cell resistance to partial contributions from the different cell components and interfaces by the EIS measurements[89]. The high frequency arc in a Nyquist plot (1) is usually assigned to the counter electrode charge transfer resistance and the associated capacitance. The second arc (2), is associated with a transmission line that represents the mesoporous layer and its interaction with the electrolyte solution. It includes parameters such as transport resistance of electrons in the mesoporous layer, recombination resistance at the TiO_2/electrolyte interface and the chemical capacitance of the TiO_2. The low frequency arc (3) is due to the impedance related to diffusion in the electrolyte. The initial displacement of the arcs from the origin corresponds to the contribution from the FTO series resistance, R_s. Separation of

different components of the cell and the analysis of their dependence on potential using EIS is a very valuable tool to determine the properties of the solar cell[88].

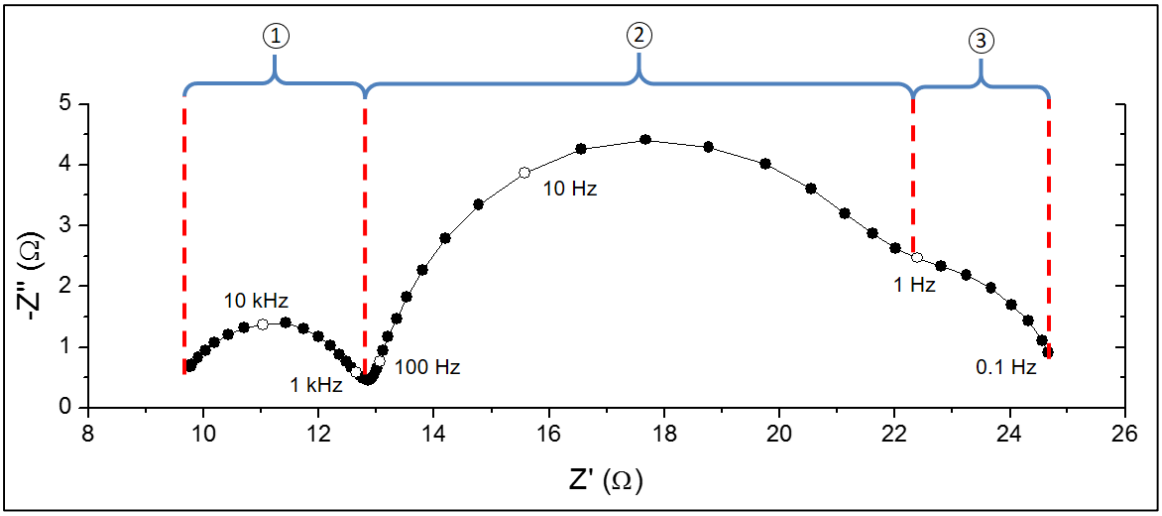

Figure 3.9. Nyquist plot obtained from EIS measurements. Regions associated with different process in the cell are highlighted. Representative frequency values are displayed.

Recombination resistance:

The charge transfer resistance (R_{ct} *or* R_r) represents a resistance to electronic recombination. The higher the resistance value, the lower the recombination events. Mathematically, it is the inverse of the dependence of recombination current, J_R, with variation of the Fermi level and can be expressed as[25,57,98]:

$$R_{ct} = \left(\frac{\partial E_F}{\partial J_R}\right) = R_{ct,0} exp\left(-\frac{\beta q V}{k_B T}\right) \tag{3.14}$$

where E_F is the Fermi level, $R_{ct,0}$ is a constant and β is an empirical parameter reflecting the non-linearity of recombination kinetics. A β exponent different from unity leads to a non-ideal current-voltage curve with smaller fill factors than an ideal diode curve[25]. At higher voltages the dominant mechanism of charge recombination in the DSC is the recombination

of the electrons from the TiO_2 mesoporous layer to the electrolyte. At low voltages, charge transfer from the TCO working electrode dominates[88].

The Capacitance:

The chemical capacitance (C_μ) corresponds to the differential response of the total electron density within the semiconductor upon small variations of the external voltage[25,57]:

$$C_\mu = \left(\frac{\partial n}{\partial E_F}\right) = C_{\mu,0} exp\left(\frac{\alpha q V}{k_B T}\right) \quad (3.15)$$

where n is the total electron density, $C_{\mu,0}$ is a constant and α is a parameter that reflects the average energy of the distribution of trap states below the conduction band[25,57]. In a DSC, the chemical capacitance of TiO_2 dominates at high voltages, whereas at low voltages the dominant capacitance is the combination of the capacitances at the contacts[88]. Another effect that is found often at low frequencies is a negative capacitance contribution that makes the impedance spectrum to enter the fourth quadrant. The negative capacitance decreases the charge accumulation ability of the solar cell, reducing its performance[103–108]. The product between charge transfer recombination and chemical capacitance gives the electronic lifetime:

$$\tau_n = R_{ct} C_\mu \quad (3.16)$$

The electronic lifetime is the time an electron will prevail in the mesoporous layer before it recombines. It is a central quantity to determine recombination dynamics in the DSC[98].

3.10 Intensity-modulated photovoltage and photocurrent spectroscopy (IMVS and IMPS)

Intensity-modulated photocurrent spectroscopy (IMPS) and intensity-modulated photovoltage spectroscopy (IMVS) can offer valuable information about DSCs. IMPS and IMVS yield time constants which are related to the electron transport and electron recombination, respectively. During IMPS and IMVS experiments, light with a base intensity is focused on a DSC. Upon the constant base intensity, a sinusoidal waveform is superimposed. The frequency of the sine wave is changed during the experiment. The photocurrent (IMPS) or photovoltage (IMVS) of a DSC is measured. The resulting signal has the same frequency as the applied signal, but its phase is shifted. By changing the frequency of the light signal, time-dependent information about various processes such as diffusion or reaction rates can be obtained[109]. The IMVS response in the frequency domain is a semicircle in the negative complex plane (Figure 3.10).

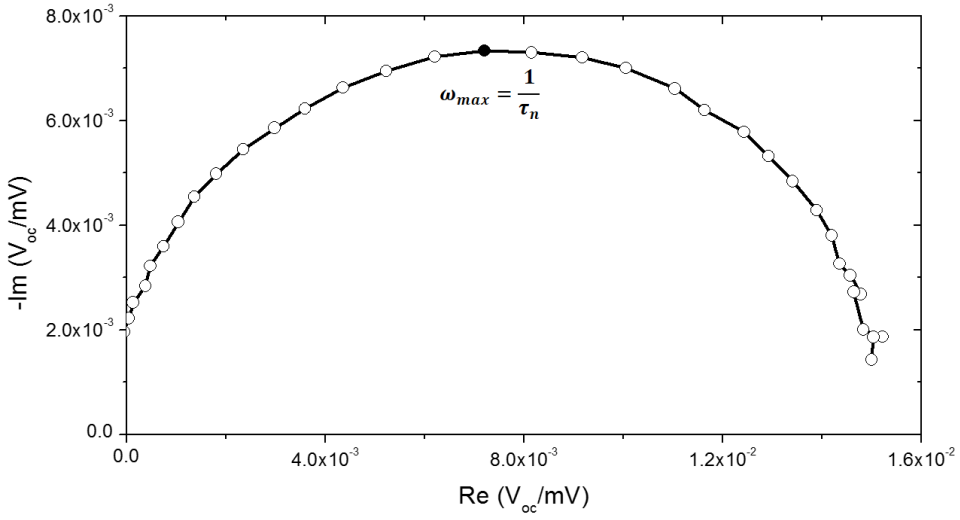

Figure 3.10. Nyquist plot of an IMVS measurement. The frequency associated with the time constant is displayed.

The maximum value of the semicircle is located at an angular frequency, ω_{max}, which is related with the effective electron lifetime, τ_n, according to[110]:

$$\omega_{max} = \frac{1}{\tau_n^{IMVS}} \tag{3.17}$$

Under short circuit conditions, the electron lifetime is assumed to be much larger than the electron transport time, so the time constant, τ_{IMPS}, obtained from the inverse of the maximum angular frequency is nearly equal to the transport time (Figure 3.11)[11].

This time constant can be related to the effective diffusion coefficient, *Dn*, by:

$$\tau_{IMPS} = \frac{d^2}{\gamma D_n} \tag{3.18}$$

where γ is a numerical factor, and d is the film thickness[11]. At low frequencies, the IMPS plots converge to a point on the real axis that corresponds to the steady-state photocurrent. At high frequencies, the excitation time is shorter than the relaxation time of the charge carrier density by transport to the contacts and the modulated photocurrent tends to zero[110].

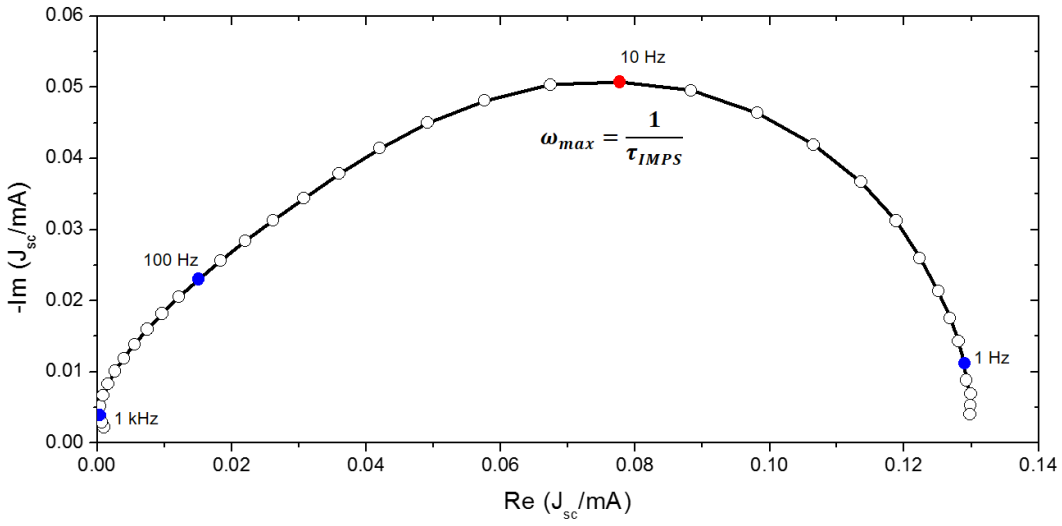

Figure 3.11. Nyquist plot of an IMPS measurement. Frequency values are displayed.

CHAPTER 4

Study of recombination in DSCs by small perturbation techniques

As mentioned in Chapter 2, cobalt redox couples represent an interesting alternative to the more commonly used iodide/triiodide redox couples, since they possess a more positive redox potential than the iodide/triiodide redox couple, which may increase the maximum photovoltage a DSC can achieve. However, the kinetics of recombination for these redox couples are usually very fast, since the reaction involves only one electron. Feldt *et al*[32] found that a suitable organic dye may help to decrease recombination with the cobalt redox couple and, nowadays, the most efficient DSCs are prepared by employing high extinction coefficient organic bulky dyes, which can absorb large amount of light while, at the same time, can prevent direct recombination with the cobalt redox couple [28]. On the other hand, ruthenium dyes, although largely used for DSCs with iodide/triiodide electrolyte solution, have failed to make the transition to DSCs with alternative redox couples, particularly with cobalt-based electrolyte solutions. It has been suggested that the bad performance of ruthenium dyes with cobalt-based electrolyte solutions is due to the interaction between the positively charged $[Co(bpy)_3]^{3+}$ and the negatively charged carboxylates of the ruthenium dye, which increases the interaction between the $[Co(bpy)_3]^{3+}$ redox couple and electrons in the sensitized mesoporous layer, increasing recombination in the solar cell[111]. It has been reported that the long alkyl chains incorporated into the Z-907 ruthenium dye structure

(Figure 4.3) may prevent direct interaction between electrons in the semiconductor and the cobalt-based electrolyte solution and DSCs with this configuration have presented efficiencies as high as 6.5%[112]. In this chapter, a study of the performance and charge recombination with steady-state and small perturbation techniques is presented for DSCs with the Z907 ruthenium dye and I^-/I_3^- and $[Co(bpy)_3]^{2+/3+}$ redox couples.

4.1 Experimental procedure

A customized TiO_2 paste was prepared according to the procedure reported by Escalante *et al*[23,24]. An amount of 0.2 mol of acetic acid was added all at once to 0.2 mol of titanium iso-propoxide and vigorously stirred for 15 min at room temperature. The mixture of titanium iso-propoxide and acetic acid was added drop-wise into a flask with 290 mL water with vigorous stirring. The final mixture was stirred at 700 rpm for 40 min. After adding 4 mL of nitric acid, the mixture was heated from room temperature to 80 °C within 40 min and subsequently peptized for 75 min. Water was then added to the cooling liquid mixture to adjust the volume to 370 mL. Aliquots from the resultant mixture were hydrothermally treated at 200 °C for 12 h in a Teflon-lined stainless steel autoclave (Parr Instruments). After the heating process, the mixture was sonicated for 1 h, centrifuged, and washed with ethanol. The final material was a colloid with 40 wt% TiO_2. An amount of 1.8 g of the colloid was dissolved in 9 mL ethanol and mixed with 7.3 g of terpineol; the resulting mixture was sonicated for 1 h. This mixture was added drop-wise to a solution of 0.9 g ethyl cellulose in 10 mL ethanol. The final mixture was sonicated for 1 h and the excess ethanol was removed with the aid of a rotary evaporator. To prepare the DSC working electrodes, FTO glass is used as current collector (Pilkington TEC 15). The FTO glass was cleaned in an ultrasonic bath by a total of 4 sonications each 10 min long, using, in consecutive order: (1) a detergent

solution (Alconox), (2) distilled water, (3) ethanol and (4) isopropanol. The FTO substrate glasses were heated up to 450 °C for 30 min in order to eliminate all the organic residues. The compact layer was prepared by preheating the FTO substrates to 500 °C for 10 minutes; one layer of a solution of 0.2 M titanium diisopropoxide bis(acetylacetonate) in isopropanol was sprayed over the FTO every 10 seconds during two minutes. The FTOs were then sintered at 500 °C during 30 min and cooled to room temperature. The mesoporous layer of TiO_2 paste was applied via screen printing, after which the films were heated following the temperature ramp described in Figure 4.1. At a final temperature of 80 °C, the electrodes were immersed in a 0.25 mM Z-907 dye in acetonitrile/*tert*-butanol (1 to 1 volumen ratio) and kept at room temperature for 24h in the dark to assure complete sensitizer uptake.

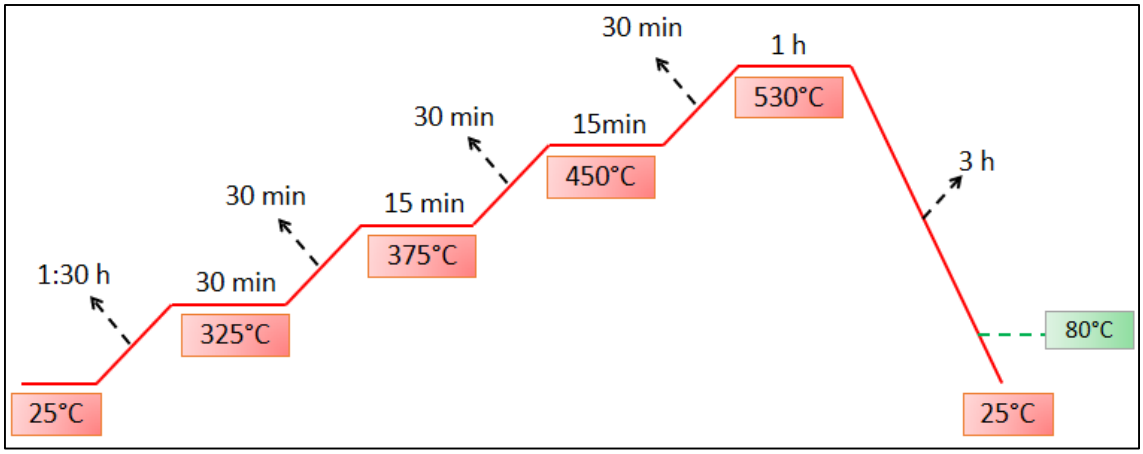

Figure 4.1. Temperature ramp for the sintering of TiO_2 films after screen printing deposition. When films are heat-treated prior to dye loading, the process is halted at 80 °C.

To prepare the counter electrodes, two holes were drilled in FTO-covered glass electrodes (Pilkington TEC 8). The perforated counter electrodes were cleaned following the same procedure as used for the working electrodes. The counter electrode was covered with Pt electrocatalyst by spreading a drop of Platisol (Solaronix) and sintering at 400 °C for 5 min. The sensitized TiO_2 electrode and Pt-catalyzed counter electrode were assembled into a

sandwich-type cell and sealed with Surlyn polymer of 60 µm thickness by applying mechanical pressure and a temperature of 215 °C for 15 min.

The electrolyte solution was introduced through the small holes in the back of the counter electrode. The composition of the I^-/I_3^- electrolyte solution was 0.6 M DMII (1,2-dimethyl-3-propylimidazolium iodide), 0.1 M LiI (lithium iodide), 0.1 M GuSCN (guanidinium thiocyanate), 0.05 M I_2, and 0.5 M TBP (tert-butyl pyridine), in a mixture of acetonitrile and valeronitrile (volume ratio 85:15). For the cobalt (II/III) tris(2,2'- bipyridine) $[Co(bpy)_3]^{2+/3+}$ electrolyte solution, the composition was 0.22 M $[Co(bpy)_3]^{2+}$, 0.05 $[Co(bpy)_3]^{3+}$ and 0.2 M TBP in acetonitrile. In order to have good electrical contact for the connections to the measurement set-up, the edges of the FTO outside the cell were covered with a conductive silver paint (SPI-High Purity Silver Paint). The thickness of the TiO_2 nanoparticulate film was measured using an AlphaStep D-120 profilometer (KLA Tencor). The crystal structure and average particle size of the TiO_2 films were determined by X-ray diffraction (XRD) using a Siemens D-5000 with CuKα radiation. Photovoltaic characterization was performed using a set-up consisting of a 450 W ozone-free Xe-lamp (Oriel, Newport Corporation) with a water filter, calibrated to an irradiance of 100 mW/cm^2 on the surface of the solar cell using an Air Mass 1.5 Global (AM 1.5G) optical filter (Newport Corporation); the intensity was calibrated using a certified 4 cm^2 monocrystalline silicon reference cell with incorporated KG-5 filter. The scan rate for all the current–voltage curves was 0.01 V/s. Current–voltage curves and electrochemical impedance spectroscopy were recorded with an Autolab PGSTAT302N/FRA2 set-up. The EIS measurements were performed under red LED illumination (625 nm), an AC amplitude of 10 mV was applied and the frequency range was from 0.1 Hz to 100 kHz. The electrochemical impedance spectrum was analyzed using Z-

View software with the aid of the equivalent circuit proposed by Fabregat-Santiago *et al*[88], previously presented in Figure 3.8.

4.2 Results and discussion

Characterization of the TiO_2 mesoporous layer by X-ray diffraction measurements is shown in Figure 4.2. The average crystallite size, Ø, was estimated using the Scherrer equation[25]:

$$\emptyset = \frac{(0.94)\lambda}{B cos\theta} \tag{4.1}$$

where 0.94 is the Debye-Scherrer constant, λ is the X-ray wavelength, θ is the Bragg angle (measured in radians) at which the peak is observed, and *B* is the full width at half maximum. The TiO_2 film was crystalline and consisted of pure anatase and the average crystallite size, calculated from both main peaks (2θ = 25.3° and 2θ = 48°), was approximately 18 nm (diameter).

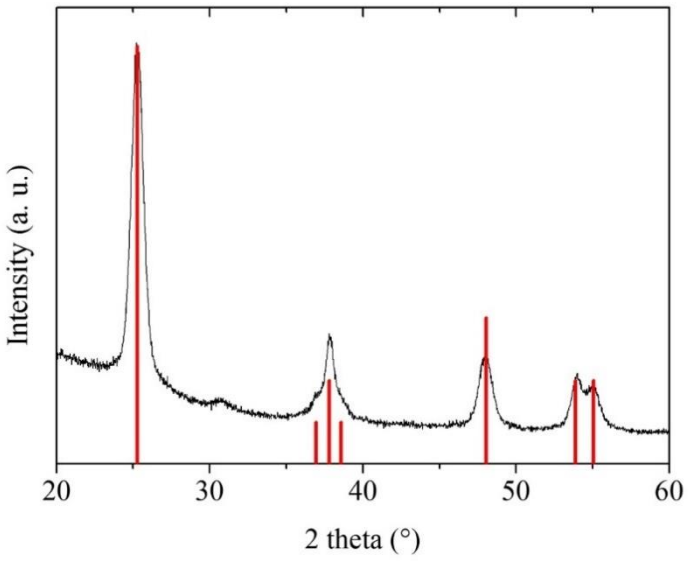

Figure 4.2. XRD pattern of the TiO_2 films. The main peaks of the anatase phase are displayed.

Four different DSC systems were fabricated in order to evaluate the influence of the compact layer and the effect of the redox couple when interacting with Z-907 sensitized DSCs. The chemical structures of Z-907 and $[Co(bpy)_3]^{2+}$ are presented in Figure 4.3. Three cells for each configuration were employed in the characterization. For the evaluation of the blocking layer, J-V curves and OCVD measurements were employed. The configuration of the cells along with the results from the J-V curves are summarized in Table 4.1 and a representative J-V curve of each system is displayed in Figure 4.4.

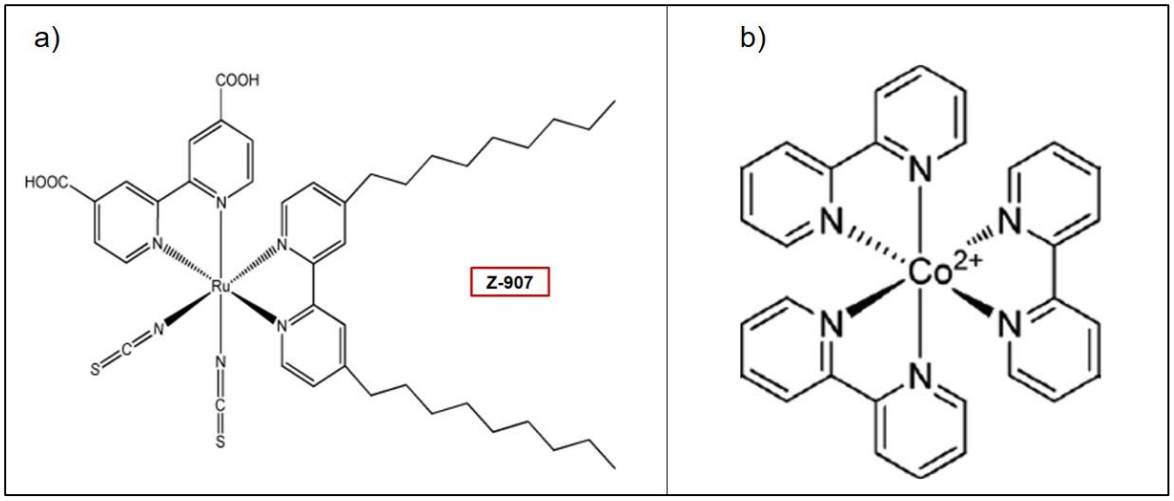

Figure 4.3. Chemical structure of (**a**) Z-907 dye and (**b**) $[Co(bpy)_3]^{2+}$ complex.

The thickness of the mesoporous layer was (7.9 ± 0.3) µm and (7.2 ± 0.1) µm for I^-/I_3^- and $[Co(bpy)_3]^{2+/3+}$ DSCs, respectively. The influence of the blocking layer in the performance of the DSCs cannot be underestimated. From table 4.1 and Figure 4.4, a clear difference is observed between the cells with and without compact layer. For the iodide cells, the open circuit potential does not change significantly. It has been previously reported that recombination between electrons in the FTO and the electrolyte solution is not the main recombination pathway for cells with iodide/triiodide electrolyte[67]. However, a change in the current density is observed in all iodide cells. As mentioned in Chapter 2, the role of the compact layer is not only to prevent recombination between

the substrate and the electrolyte solution, but also to improve the contact between the mesoporous layer and the FTO. This will help to have a better collection efficiency of electrons and will lead to an increase in photocurrent, as observed in Figure 4.4.

Table 4.1. Average J-V parameter values of the DSCs. At least three cells of each configuration were measured.

Redox couple	*Compact layer*	*V_{oc} (V)*	*J_{sc} (mA/cm^2)*	*FF*	*Efficiency (%)*
I^-/I_3^-	No	0.700 ± 0.002	10.8 ± 0.5	0.63 ± 0.1	4.8 ± 0.3
	Yes	0.701	12.6 ± 0.1	0.61 ± 0.1	5.4 ± 0.1
$[Co(bpy)_3]^{2+/3+}$	No	0.123 ± 0.033	1.2 ± 0.1	0.35 ± 0.1	≈ 0.1
	Yes	0.624 ± 0.045	2.0 ± 0.1	0.40 ± 0.1	0.5 ± 0.1

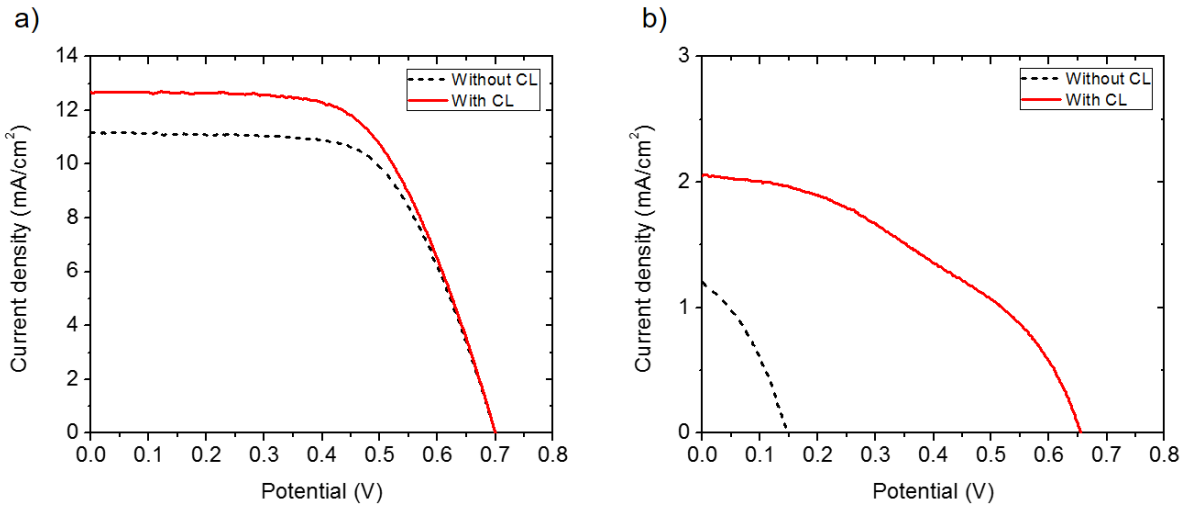

Figure 4.4. Representative J-V curves of (**a**) I^-/I_3^- and (**b**) $[Co(bpy)_3]^{2+/3+}$ DSCs with and without compact layer. CL stands for compact layer.

The change is even more dramatic when working with cobalt DSCs. If no compact layer is applied, the performance of the DSC is very poor, reaching small values of J_{sc} and V_{oc}, with efficiencies under 0.1%. These results show that by only implementing the Z-907 ruthenium dye, the electronic recombination with the cobalt-based electrolyte is not prevented. When the compact layer is applied, the performance of the cobalt DSC improves significantly, with V_{oc} increasing to around 620 mV, doubling the photocurrent, and increasing over 5 times its efficiency. This results suggest that recombination with the substrate is an important factor to take into consideration when working with cobalt redox couples. In spite of the notorious increase in performance when the blocking layer was applied for cells with cobalt electrolyte solution, the resulting DSC still presented an overall bad performance, especially when compared with iodide DSCs. In their work, Liu *et al*[112], presented a DSCs with Z-907 dye and cobalt $[Co(bpy)_3]^{2+/3+}$ redox couple with efficiencies as high as 6.5%. However, this result was obtained for DSCs with an adequate blocking layer, an optimized electrolyte solution with a higher concentration of tbp (0.5 M) and with the implementation of a scattering layer and $TiCl_4$ treatment. Mosconi *et al*[111] worked with the same system but with a DSC with a similar configuration to the one employed in this work (no scattering layer and a tbp concentration of 0.2 M), reporting a maximum efficiency of 2.1%. These results show that in order to obtain a good performance DSC with the Z-907 ruthenium dye and a cobalt-based electrolyte solution, a combination of an adequate blocking layer and high concentration of tbp in the electrolyte solution also have to be employed.

OCVD measurement results for iodide cells are summarized in Figure 4.5. No results are reported for cobalt cells due to the low performance of the system. From Figure 4.5 it can be observed that, even though there seems to be no difference in the open circuit potential, the

loss of photovoltage over time is reduced with the incorporation of a blocking layer. As time goes on, the voltage loss for the cell with the blocking layer becomes slower, probably due to the presence of traps. As mentioned in Chapter 3, in order to recombine, the electrons must be de-trapped before transferring to I_3^-, and as the quasi-Fermi level moves to lower energy, de-trapping slows down considerably. The voltage decay close to open circuit potential is related with the electronic lifetime of electrons in the mesoporous layer, provided that there is no strong recombination between electrons in the substrate and the electrolyte solution. In Figure 4.5 (b), a negligible difference in electronic lifetime is observed for iodide DSCs with and without compact layer at high voltages close to V_{oc}.

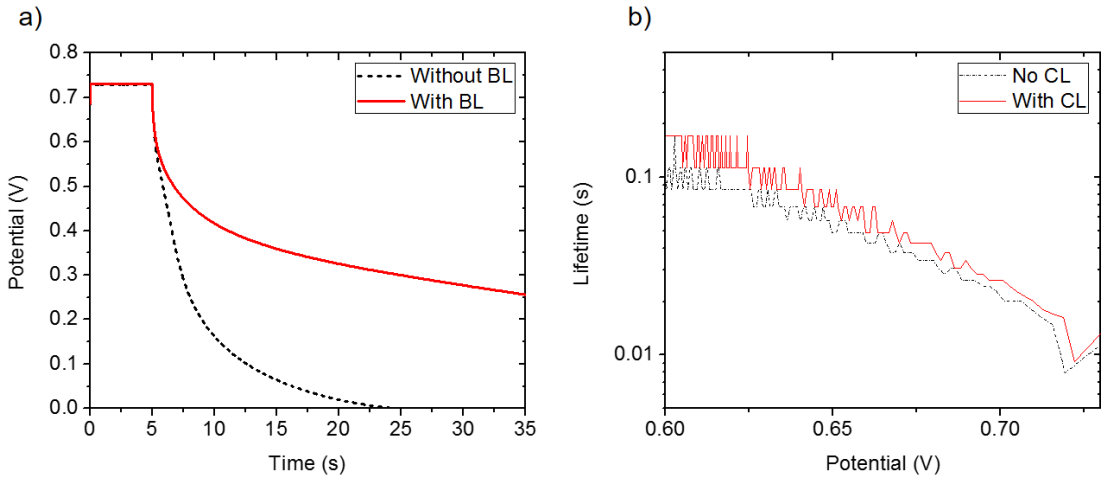

Figure 4.5. (**a**) OCVD measurements for iodide cells with and without compact layer. (**b**) Electronic lifetime obtained with equation (3.10) at potentials close to V_{oc}.

Electrochemical impedance characterization under illumination was employed to distinguish differences between systems with different redox couples. All the cells analyzed with EIS had a blocking layer. The Nyquist plots are presented in Figure 4.6 for both DSCs. From the Nyquist plot for the iodide DSC the three main semicircles related with processes in the counter electrode, transport and recombination of electrons and the diffusion impedance can

be properly distinguished. This allows to obtain parameters such as the charge transfer resistance or the chemical capacitance. For $[Co(bpy)_3]^{2+}$ DSCs at open circuit this statement may also be valid. However, the shape and size of the semicircles is very different to that for the iodide cells. The semicircle that involves the processes at the counter electrode is merged with the transmission line semicircle, so it cannot be properly evaluated. However, the charge transfer resistance still can be determined since the shape of the second semicircle is still very clear. The third semicircle shows that the diffusion impedance for the cobalt redox couple is considerably larger than for iodide DSCs, which is consistent with reported results of mass transport limitations for this redox couple[36,93,94].

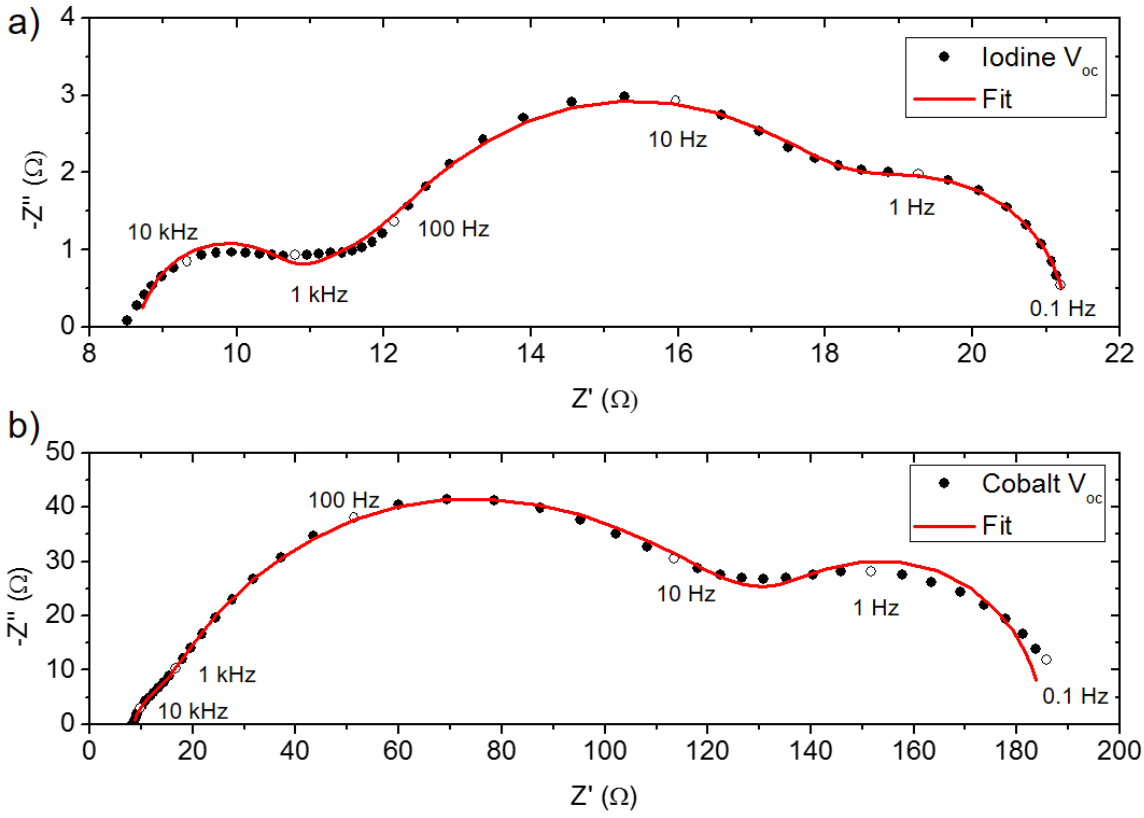

Figure 4.6. Nyquist plots for (**a**) I^-/I_3^- DSC and (**b**) $[Co(bpy)_3]^{2+/3+}$ DSC. EIS measurements were made under illumination at 0.726 and 0.602 V, respectively. The fitting curves are displayed.

From the EIS analysis of the Nyquist plots at different potentials, information about the internal processes in the DSC can be obtained (Figure 4.7).

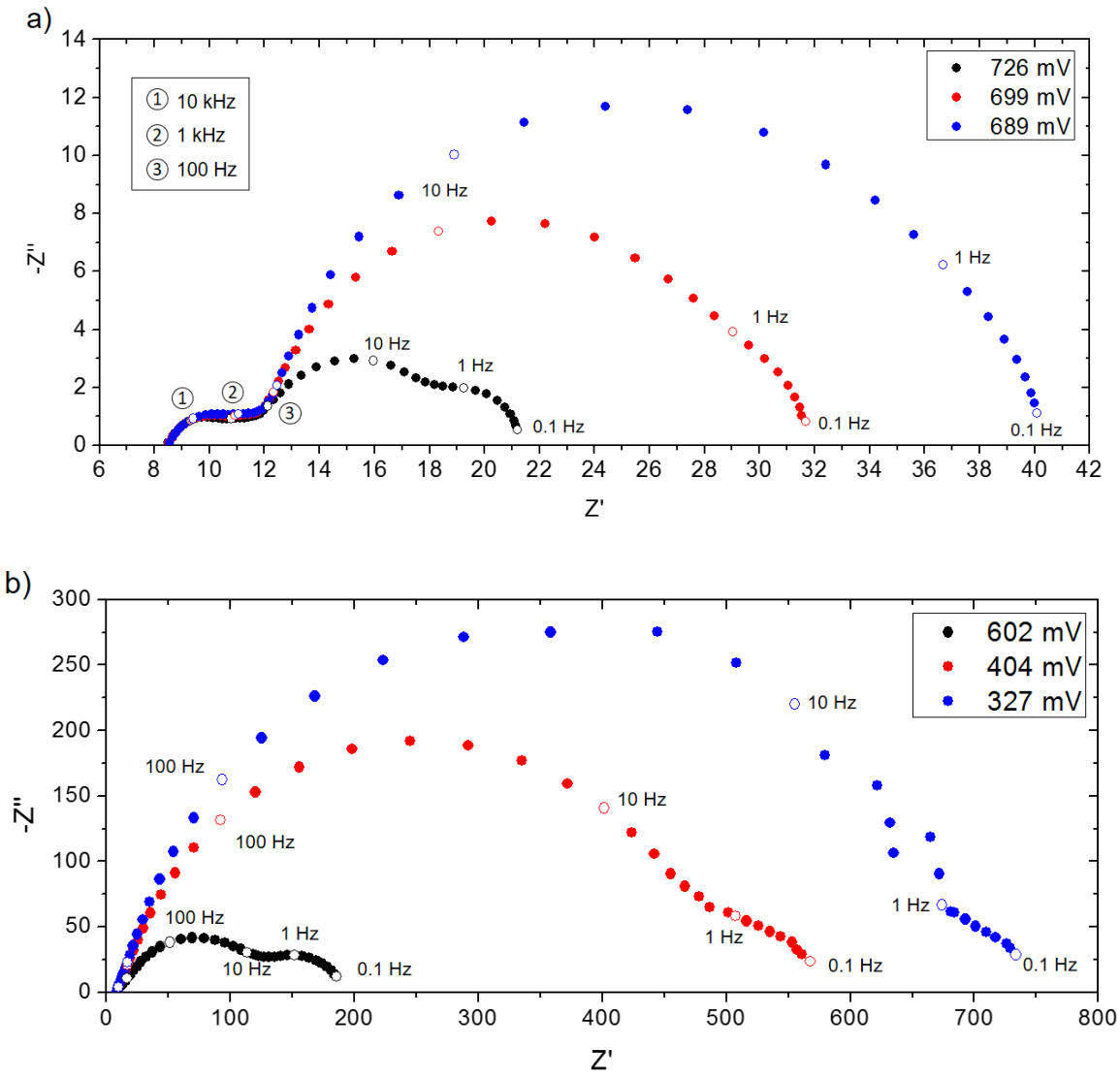

Figure 4.7. Nyquist plots obtained at different potentials for (**a**) iodide and (**b**) cobalt DSCs.

For the DSCs with iodide based electrolyte solution, the semicircle associated with the processes in the counter electrode remains unchanged with the decrease of potential. This implies that the processes on the counter electrode are independent of the potential applied, and changes in the behavior of the cell related with changes in the potential are not related

with the counter electrode. However, the size of the second semicircle, associated with transport and recombination inside the DSC, increases considerably. This behavior is related to an increase in the charge transfer resistance with potential, as shown in Figure 4.8. The same trend can be observed for the DSCs with a cobalt based electrolyte solution. In Figure 4.8 the charge transfer resistance and chemical capacitance obtained from EIS analysis for DSCs with iodide based electrolyte solution configurations are presented.

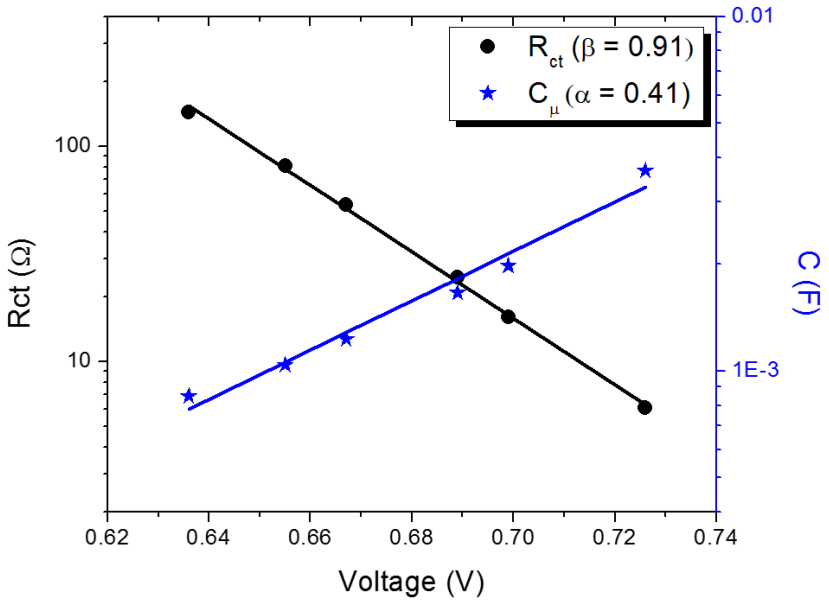

Figure 4.8. Charge transfer resistance and chemical capacitance for iodide DSCs. The α and β parameters are also displayed.

The exponential dependence of charge transfer resistance and chemical capacitance on potential is related to the reported exponential distribution of traps below the conduction band[23,25,57]. It can be observed that the charge transfer resistance value decreases as the potential increases. At high potentials, a larger concentration of electrons is present in the mesoporous layer, which will increase recombination events and, thus, a decrease in charge transfer recombination resistance. As the Fermi Level goes to lower energy (more positive

values of potential), the population of electrons in the mesoporous layer also decreases, thus, recombination processes also decrease and the overall charge transfer resistance increases. The chemical capacitance indicates how the electronic density changes with the potential and from Figure 4.8 it is observed that the electronic density increases exponentially with potential. This is expected since at higher potentials, the electronic density will also be higher, and an increase in the potential will also increase the electronic density, giving an increase in chemical capacitance. The electronic lifetime obtained with EIS is presented in Figure 4.9.

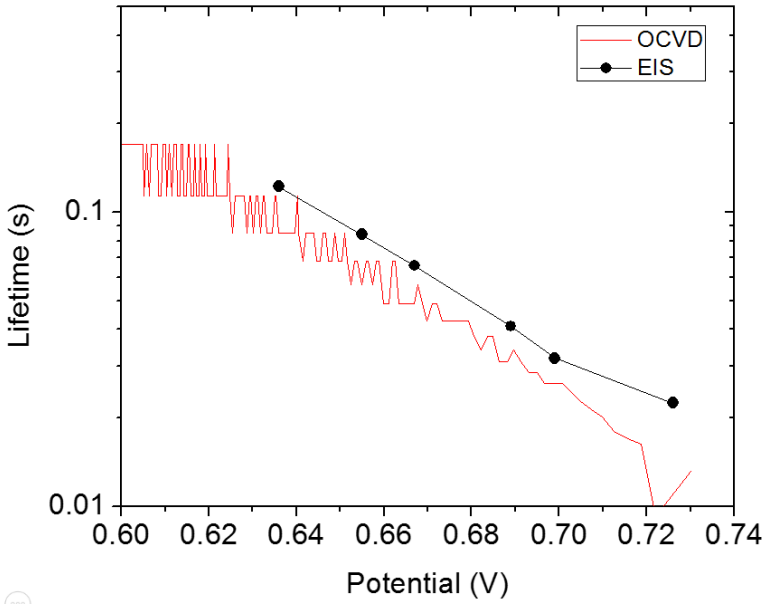

Figure 4.9. Electronic lifetime for iodide DSC. The values obtained from OCVD measurements are displayed as a reference.

Although the electronic lifetime depends on the charge transfer resistance and the chemical capacitance, and both behave differently with the increase in potential, recombination at high potential values predominates and the electronic lifetime follows the same trend as the charge transfer resistance, becoming smaller for higher potentials. This behavior is the same obtained from OCVD measurements, and the values of electronic lifetime are also very

similar when compared at the same potential, which confirms that these two different techniques, under appropriate conditions, deliver the same values of electronic lifetime.

The results of EIS for cobalt DSCs are displayed in Figure 4.10.

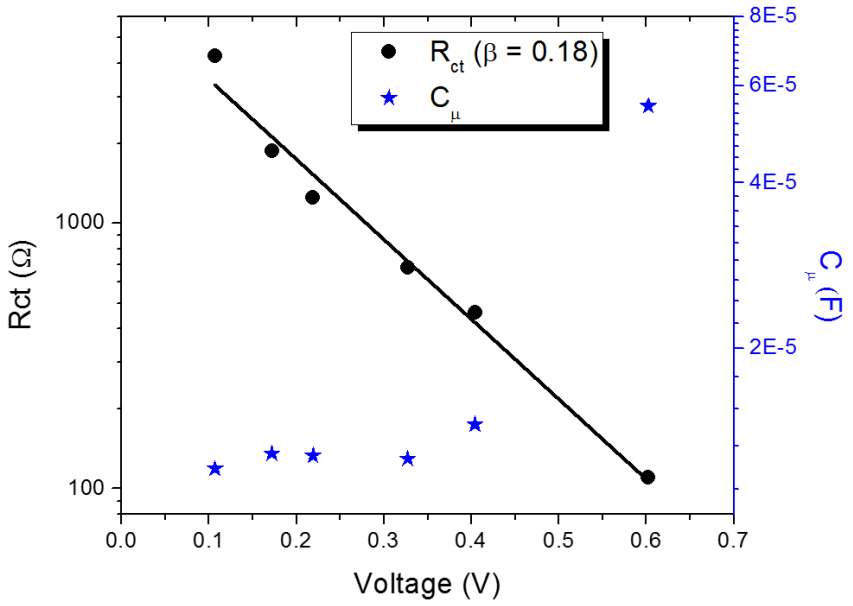

Figure 4.10. Charge transfer resistance and chemical capacitance obtained for cobalt DSCs. The value of β is also displayed.

From Figure 4.10, an exponential behavior for the charge transfer resistance is also obtained. However, the value of β is completely different than for the iodide cells. This suggest that recombination is different for cobalt and iodide cells. It is important to mention that for low photovoltage values, the recombination may be dominated by charge transfer processes from the FTO to the electrolyte solution, as has been already reported[88]. This may explain the differences in the β value. For the chemical capacitance, it has also been reported that at low photovoltages, the capacitance of the cell is actually dominated by the capacitance at the contacts[88], and the value obtained from the analysis of EIS does not represent the chemical capacitance of the cell and, thus, does not give information on the electronic distribution in

the semiconductor. For this reason, no α value is reported. No results of electronic lifetime for cobalt-based DSC are displayed since, at low photovoltages, determination of charge transfer resistance and chemical capacitance are not reliable via EIS measurements, so the time constant obtained from Equation 3.16 will not represent the electronic lifetime inside the DSC. These results imply that due to the large recombination and bad performance of cobalt-based DSCs, a direct comparison between the latter and iodide based DSCs will not be possible via EIS measurements.

4.3 Conclusions

The compact layer increased the performance of the DSCs especially for the cobalt based cells. It was observed that, when used alone, the Z-907 ruthenium dye does not work properly with $[Co(bpy)_3]^{2+/3+}$. DSCs with cobalt-based electrolyte solution require not only an appropriate dye that can prevent fast recombination with the electrons in the mesoporous layer, but also a proper compact layer to prevent recombination between electrons in the FTO and the electrolyte solution and an optimized electrolyte solution to reduce even further the recombination in the mesoporous layer. A complete EIS analysis was only possible for the iodide DSCs, where the measurements were performed close to the open circuit potential and the recombination resistance and chemical capacitance could be properly distinguished.

CHAPTER 5

Ideal thickness of the mesoporous layer in a DSC. Determination with steady-state and small perturbation techniques

One of the factors that affect DSC performance is the thickness of the nanostructured, mesoporous, TiO_2 film[24,113–119]. The exposed TiO_2 surface area is proportional to the thickness, hence, a thicker TiO_2 film allows for more dye to be adsorbed resulting in an increase in light harvesting efficiency; however, the surface is also the main source of recombination sites, which directly affects the charge collection efficiency. Various studies have shown that the efficiency of the DSC increases with thickness of the film until it reaches a critical value, and then decreases, thus defining an optimal film thickness. The optimal thickness is generally reported to be around 10 μm[24,115,118], although 15–20 μm has also been reported as the ideal thickness[113,114,117,119]. It has been proposed theoretically that this dependence on thickness is a consequence of a balance between absorption of light and photogeneration of electrons and dark electron transfer processes in the cell[120]. In describing dark processes, we need to take into account a variety of parameters. One of these parameters is the exchange current density in the dark, J_0, and several groups have analyzed the influence of J_0 on the performance of the solar cell[88,119–122]. Assuming that $J_0 \propto d$, where d is the semiconductor film thickness, Zhu and coworkers[120] determined theoretically the effect of

the film thickness dependence of J_0 on the performance of DSCs. Using this assumption, they concluded that, as the semiconductor film thickness increases, the solar cell becomes more efficient due to better absorption of light and a larger photogenerated current, but after reaching a thickness of 10 μm or more, the processes in the dark have more relevance in the performance of the cell and ultimately limit the efficiency of the device; the optimal film thickness was found to be around 10 μm. In spite of this, the relationship between J_0 and d has not been yet unambiguously demonstrated and has not been verified experimentally.

In this chapter J_0 is determined by steady state current-voltage measurements via the diode equation and by small perturbation techniques. Using a continuity equation model for the total electron density, a relationship between J_0 and the recombination time constant and electron density in the dark is analytically derived. The relationship was corroborated experimentally. Implementing the diode equation, the influence of the ideality factor, the exchange current density in the dark and the effective absorption coefficient on the determination of the optimal film thickness in DSCs is described.

5.1 Theoretical background

5.1.1. Determination of J_0 from Steady State Measurements.

The current voltage response of a solar cell can be approximated as the sum of the short circuit photocurrent and the dark current as a function of applied voltage; this method is known as the superposition approximation. Although the reverse current which flows in response to voltage in an illuminated cell is not formally equal to the current that flows in the dark, the approximation is reasonable for many photovoltaic materials. The sign convention for current and voltage in photovoltaics is such that the photocurrent is positive. With this sign convention and for a non-ideal diode, the net current density in the cell is[25,123,124]:

$$J = J_{SC} - J_0 \left[exp\left(\frac{qV}{mk_BT}\right) - 1 \right] \quad (5.1)$$

where J_0 is the exchange current density in the dark and m is the ideality factor of the diode equation. The value of m depends on the order of the recombination reaction rate in electrons and oxidized species in the electrolyte, and the distribution of recombination sites[125,126]. In addition, the value of J_0 is related to the rate constant of the recombination reaction, the film thickness, the order of reactions of electrons and oxidized redox species, and the background concentrations of electrons in the TiO_2 and oxidized redox species in the electrolyte[120]. The second part of Equation (5.1) represents the dark current density. At sufficiently high bias, the two currents cancel, corresponding to open-circuit conditions, while at zero bias the cell produces its maximum current, corresponding to short-circuit conditions. Together with series resistance losses, the balance between transport and recombination determines the shape of the current–voltage curve of the device[25,127]. If only the resistance losses relating to current are considered, the expression for the net current density (J_{net}) of a DSC can be expressed as:

$$J_{net}(V) = J_{SC} - J_0 \left\{ exp\left[\frac{q\left(V + J_{net}R_S^{total}\right)}{mk_BT} \right] - 1 \right\} \quad (5.2)$$

where J_{net} is the net photocurrent density and R_s^{total} is the total series resistance of the solar cell. From the last equation we can obtain:

$$\frac{dV}{dJ_{net}} = -R_S^{total} + \frac{mk_BT}{q} \cdot \frac{1}{J_{net} - J_{sc} - J_0} \quad (5.3)$$

The dark exchange current density, J_0, is normally orders of magnitude smaller than the sum of J_{net} and J_{SC} and, therefore, can be neglected in this equation[120,128]. Isolating the J_0 term in

Equation (5.2) and under open circuit conditions (J_{net} = 0), the following expression is obtained:

$$J_0 = \frac{J_{SC}}{exp\left(\frac{qV_{oc}}{mk_BT}\right) - 1} \tag{5.4}$$

From equation (5.4) the value of J_0 can be obtained. Considering no recombination losses at short-circuit conditions, the value of J_{sc} will be equal to the light absorbed:

$$J_{SC} = q\phi(\lambda)T_{FTO}[1 - exp(-\alpha_{abs}d)] \tag{5.5}$$

where $\phi(\lambda)$ is the incident photon flux, T_{FTO} is the effective transmittance of the FTO substrate, and α_{abs} is the effective absorption coefficient of the solar cell. Assuming a collection efficiency of over 99% ($\eta_{cc} \geq 99\%$), $J_0 \propto d$, ohmic losses have been corrected for and light scattering, reflection at the counter electrode and light absorption by the iodide electrolyte and TiO_2 are negligible[120], the diode equation can be expressed as:

$$J(V) = -J_{00}d\left[exp\left(\frac{qV}{mk_BT}\right) - 1\right] + q\phi T_{FTO}[1 - exp(-\alpha_{abs}d)] \tag{5.6}$$

where J_{00} is the exchange current density per unit film thickness. The first and second terms on the right side of the last equation denote the contributions to $J(V)$ in the dark and in the light, respectively[120].

5.1.2. Determination of J_0 from Small Perturbation Techniques

The electron transport and recombination properties of the DSC have been investigated using a continuity equation for electrons, which can either be expressed in terms of the free electron density in the conduction band, including a separate term for the trapping and detrapping processes, or in terms of the total electron density; it has been shown that these two

approaches are mathematically equivalent under "quasi-static conditions"[25]. It is convenient to express the continuity equation in terms of the total electron density in the photoanode, *n*, as this is an experimentally accessible quantity: the total electron density includes both free and trapped electrons and can be determined experimentally by charge extraction measurements. Assuming 1-dimensional geometry for electronic processes in the photoanode, the continuity equation can be written as[25]:

$$\frac{\partial n(x,t)}{\partial t} = \frac{\partial}{\partial x}\left[D_n(n(x))\frac{\partial n(x)}{\partial x}\right] + G(x) - k_n\big(n(x)\big)n(x,t) \tag{5.7}$$

which is the continuity equation in terms of the total electron density, *n*, taking the approximation that a quasi-static equilibrium holds between free and trapped electrons. Here, *x* is the distance to the working electrode, *G(x)* is the volume generation rate and the trapping-detrapping dynamics are implicitly considered in the form of an effective diffusion coefficient, D_n, and an effective recombination constant, k_n, which are a function of the total electron density. Another advantage of using Equation (5.7) is that the transient and stationary behaviors of the device are described with a single continuity equation[25], so this equation can also be used in the time-dependent analysis. The photovoltage is related to the total density accumulated in the semiconductor as[25]:

$$n = n_0 exp\left[\frac{\alpha q V}{k_B T}\right] \tag{5.8}$$

where n_0 is the total electron density in the dark and α is a parameter that reflects the average energy of the exponential distribution of trap states below the conduction band. This parameter can be estimated from capacitance data obtained from impedance measurements. In the continuity equation (Equation (5.7)), the last term represents the recombination term, in which k_n stands as a small-perturbation recombination constant, which can be obtained

directly by small perturbation techniques. The recombination constant represents all possible recombination processes, including recombination with the dye, and can be expressed as[25]:

$$k_n(n) = k_0 \left(\frac{n}{n_0}\right)^{\frac{\beta-\alpha}{\alpha}} \tag{5.9}$$

where k_0 corresponds to the recombination constant in the dark and β is the recombination reaction order with respect to free electrons, corresponding to the inverse of the ideality factor, *m*. From Equations (5.8 and 5.9), an expression for the recombination term in the continuity equation is obtained:

$$k_n n = k_0 n_0 exp\left[\frac{\beta qV}{k_B T}\right] = U \tag{5.10}$$

The recombination current density (J_{rec}) at the open circuit can be approximated as[122,127]:

$$J_{rec} = Uqd = J_0 exp\left[\frac{\beta qV}{k_B T}\right] \tag{5.11}$$

where *U* is the recombination term of the continuity equation. The recombination current density, J_{rec}, is a useful parameter to describe the flux of electrons lost from the TiO_2. It gives the total rate of loss over the full TiO_2 film thickness. As the cell voltage increases, the recombination current also increases as expected due to the increasing total charge concentration, *n*, in the TiO_2[129]. Combining Equations (5.10) and (5.11) an expression for the exchange current density in the dark is obtained:

$$J_0 = k_0 n_0 qd \tag{5.12}$$

The values of k_0 and n_0 can be obtained from small perturbation techniques (Figures A5.1 and A5.2 in the Appendix), which allows to determine the value of J_0 and to compare its

value with the value obtained from steady state measurements, in particular, the current-voltage curve.

5.2.Experimental procedure

The cells were prepared and assembled the same way as presented in Chapter 4, with some slight modifications. No scattering layer was applied. In the screen printing step, a layer of TiO_2 paste was coated on the FTO and then dried for 10 min at 120 °C; five layers of TiO_2 were deposited using this method, after which the films were heated following the temperature ramp described in Figure 4.1. After the heat treatment, another five layers were deposited onto the previously deposited films in order to increase the thickness of the film. After deposition, the films underwent the previously mentioned heat treatment. This procedure was repeated until the film reached the desired thickness. Films of 5, 10, 15, 20, 25, and 30 layers were elaborated. The application of the temperature ramp is necessary every five depositions in order to prevent failures and cracks in the semiconductor film. All the electrodes were, once again, heated according to the temperature ramp described in Figure 4.1, but they were taken to a final constant temperature of 80 °C. The electrodes at 80 °C were immersed in a solution of 0.5 mM N-719 dye in ethanol and kept at room temperature for 24 h in the dark to assure complete sensitizer uptake. The electrolyte composition used was the same as in the I^-/I_3^- DSCs in Chapter 4. Photovoltaic characterization was performed using a set-up consisting of a 450 W ozone-free Xe-lamp (Oriel) with a water filter, calibrated to an irradiance of 100 mW/cm^2 on the surface of the solar cell using an Air Mass 1.5 Global (AM 1.5G) optical filter (Newport Corporation); the intensity was calibrated using a certified 4 cm^2 monocrystalline silicon reference cell with incorporated KG-5 filter. Photovoltaic characterization with blue, green, and red light LED illumination (467, 525, and 625 nm

wavelength, respectively) was also employed. The scan rate for all the current–voltage curves was 10 mV/s. J–V curves, EIS, IMPS and IMVS measurements were recorded with an Autolab PGSTAT302N/FRA2 set-up (Metrohm Autolab). The evolution of the electron transport process in the cell was investigated using EIS, both in the dark and under red light LED illumination (625 nm). An AC amplitude of 10 mV was applied and the frequency range was from 0.1 Hz to 100 kHz. The electrochemical impedance spectrum was analyzed using Z-View software with the aid of the equivalent circuit proposed by Fabregat-Santiago *et al*, presented in Figure 3.8[88,101,102]. IMPS and IMVS measurements were performed at modulation frequencies between 1 mHz and 10 kHz. A red LED (625 nm) was used to illuminate the sample from the substrate side and it served both as the bias illumination and the small sinusoidal modulated probe beam.

5.3. Results and discussion

A series of solar cells was fabricated using screen printed TiO_2 films of different thicknesses. A picture of the DSCs with a different number of coatings is presented in Figure 5.1.

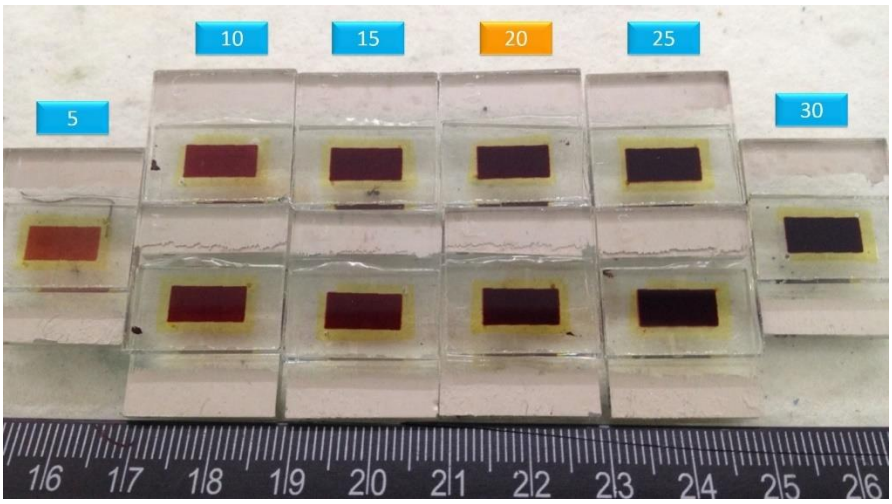

Figure 5.1. Dye solar cells prepared from the electrodes with a different number of screen-printed TiO_2 layers, hence, different thickness of the mesoporous, nanostructured TiO_2 film.

The corresponding experimental results of Scanning Electron Microscopy (SEM), are shown in the Figure A5.3 in the Appendix. Figure 5.2 shows cross sections of the TiO_2 films, after sintering, as measured by profilometry.

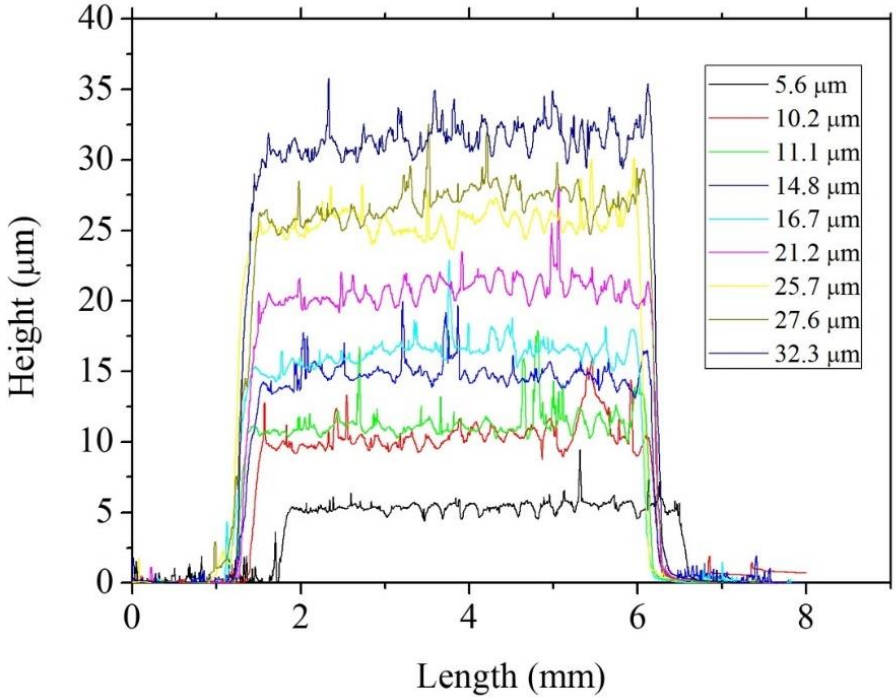

Figure 5.2. Cross sections of the TiO_2 films obtained by profilometry.

Crack free films were obtained up to a thickness of 32 μm. Figure 5.3 shows representative J–V curves for dye-sensitized solar cells, illustrating that the current at short circuit tends to increase with film thickness while the open circuit potential decreases. The characteristics of the film and solar cell are summarized in Table A5.1 in the Appendix.

Figure 5.4 shows the dependencies of the short circuit current density, open circuit photovoltage, fill factor and cell efficiency as a function of the film thickness.

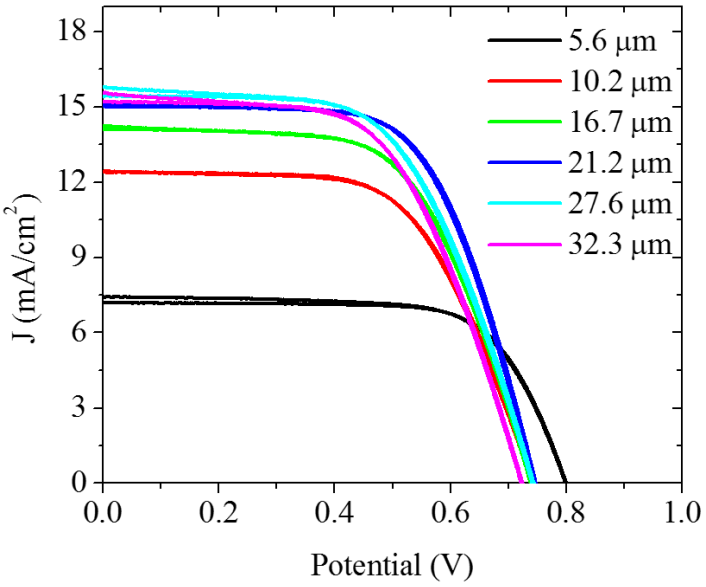

Figure 5.3. Current–voltage curves for a selection of DSCs as a function of TiO_2 film thickness.

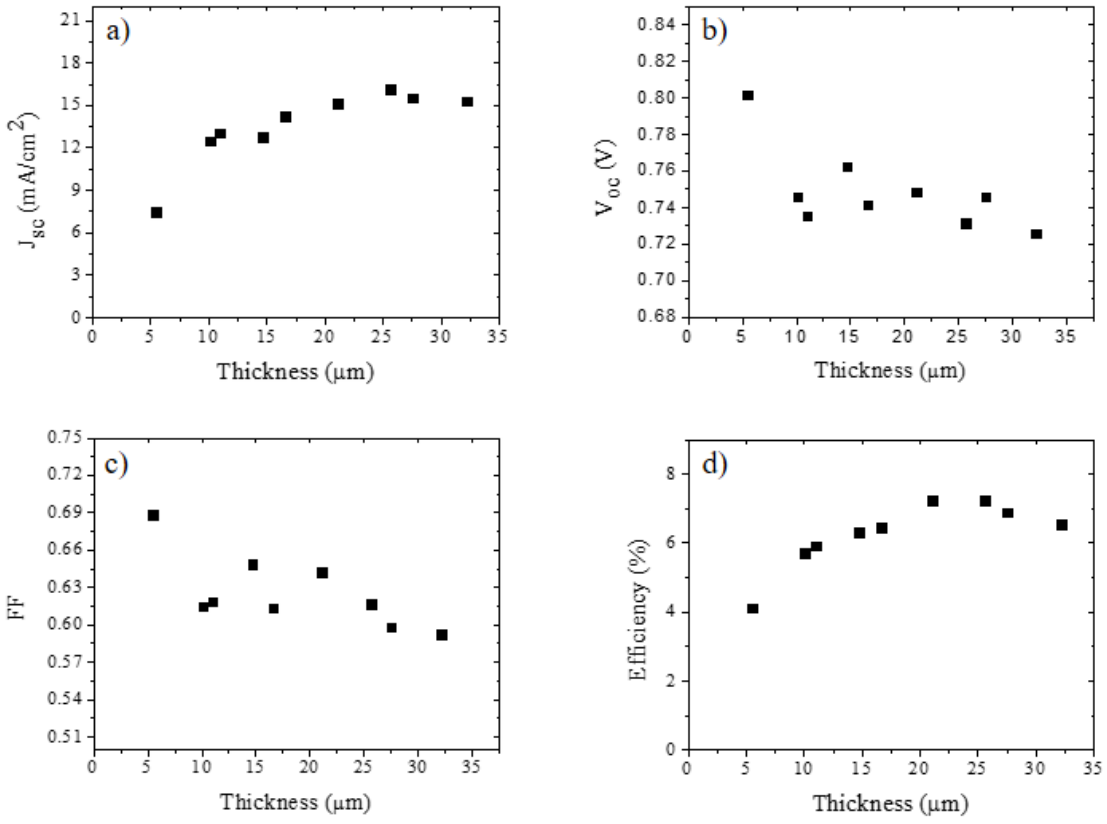

Figure 5.4. Main parameters of the solar cells as a function of TiO_2 film thickness; (**a**) J_{SC}, (**b**) V_{oc}, (**c**) Fill factor, and (**d**) Overall efficiency.

Upon increasing the film thickness, the exposed TiO_2 surface area increases, which results in the adsorption of more dye on the film[113,119]. In turn, this leads to an increase of the photogenerated electron flux, which is reflected in the increase of J_{SC}. Another important feature is that the photocurrent increases with thickness until it reaches a saturation value. This is related to the very limited increase of light absorption with increasing thickness for thick films as most light is already absorbed[116]. We can also observe that as the thickness increases, V_{oc} decreases. The V_{oc} is a parameter strongly related with recombination in the cell[24,113,118]. The main loss of current is due to a recombination process between photogenerated electrons in the TiO_2 and the oxidized redox species in the electrolyte solution[130]. As the surface area of the semiconductor film and contact area with the electrolyte solution increases, the number of recombination pathways increases thus facilitating recombination, resulting in a lower V_{oc}[113,118,119]. It is important, however, to take other factors into consideration such as dye regeneration, especially for solar cells with large film thickness; although frequently omitted, electron transfer back to the oxidized dye could become an important recombination processes that should not be ignored[129]. The fill factor also diminishes with the increase of thickness. This could be due to inefficient electron injection and/or dye regeneration, especially at high voltages, where regeneration of the dye becomes voltage dependent[131], but also to increasing series resistance losses. At high voltages, the electron concentration in the TiO_2 can be several orders of magnitude larger than that at short circuit, and this could also increase the probability of undesirable electron transfer to the oxidized sensitizer (S^+)[132]. In addition, it has been argued that the regeneration of the dye under illumination leads to a higher I_3^- concentration, which should increase the rate of recombination in DSCs[120]. As mentioned, an increase in series resistance will also decrease the value of fill factor, but, as shown in Figure 5.7, this parameter varies only

slightly with the film thickness in the solar cells. The solar cell efficiency increases with thickness due to a better absorption of light and an increase in photocurrent, until it reaches a maximum value after which it does not change significantly. If the thickness is further increased, recombination will become more important resulting in a decreased solar energy conversion efficiency[130].

Figure 5.5 shows three different Nyquist diagrams for the same cell at three different voltages. The high frequency semicircle remains unchanged, which means no significant changes are occurring at the counter electrode/electrolyte solution interface. The middle frequencies semicircle, associated with transport and recombination of electrons in the mesoporous layer, increases as the voltage decreases. This is related to an increase in charge transfer resistance for lower voltages. This can be observed in the inset of Figure 5.6(a). A third semicircle at low frequencies is observed for the high voltage solar cell. This implies diffusion limitation in this cell, due to the large thickness of the mesoporous layer. This semicircle disappears at lower voltages (*i.e.*, illumination intensity), which is usually the case for diffusion limited systems.

Figure 5.6 shows the charge transfer resistance, chemical capacitance and electronic lifetime values obtained by EIS as a function of the TiO_2 film thickness. The comparison is made at 0.74 V, although the tendency is the same at other voltages. The insets show the dependence of R_{ct} and C_{μ} on the open circuit potential under illumination (at different light intensities) for the 21.2 μm cell. The values of the trap distribution parameter α (Equations (5.8) and (5.9)) and the recombination reaction order, β, (Equation (5.9)) are also displayed.

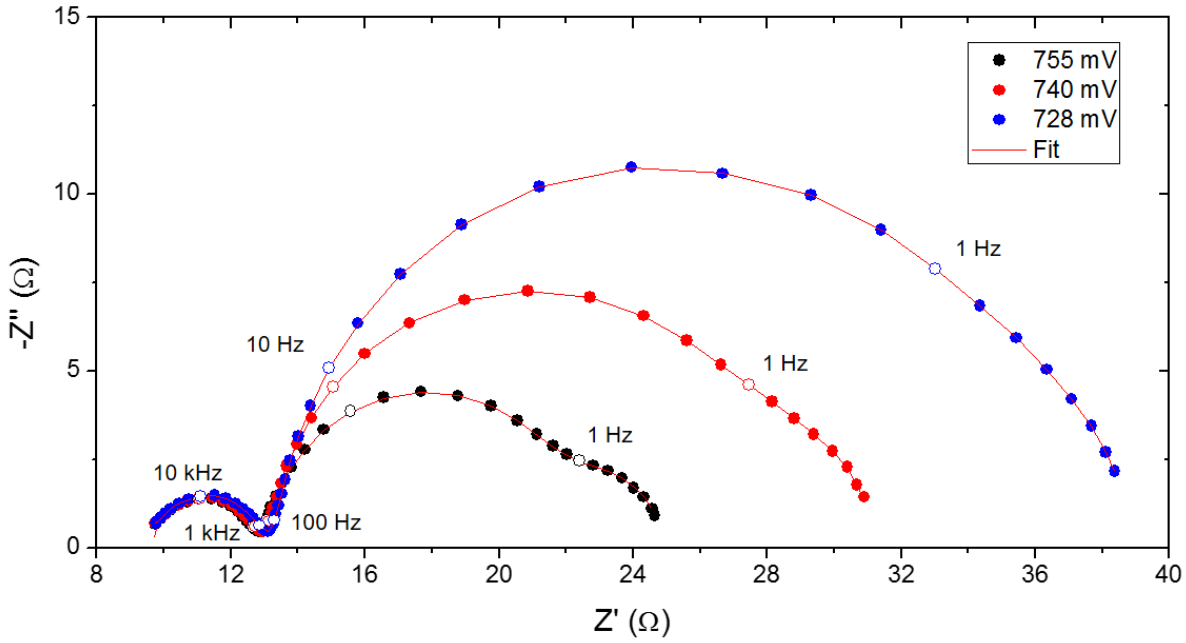

Figure 5.5. Nyquist plot and fitting results at three different voltages for the 21.2 μm cell. Representative frequency values are displayed.

The results show a decrease in R_{ct} value with increasing thickness, which means that the recombination processes between electrons in the TiO_2 film and the oxidized species in the electrolyte or dye become more significant as the thickness increases. This result is consistent with the V_{oc} thickness dependence observed in Figure 5.4. Since the surface area is proportional to the thickness (if the morphology is independent of the number of layers deposited), R_{ct} is expected to be proportional to 1/d; Figure 5.6 (a) illustrates that this is the case. The chemical capacitance increases linearly with film thickness and is proportional to the increase in surface area of the mesoporous layer. Although the chemical capacitance increases with thickness, the value of α for the cell remained constant ($\alpha \approx 0.18$), indicating that the energetic distribution of trap states stays the same. The electron lifetime is a function of the charge transfer resistance and the chemical capacitance[88,89,125]. Since both have

opposite behaviors with respect to increasing electrode thickness, the electron lifetime is essentially independent of electrode thickness[133], as illustrated in Figure 5.6 (c).

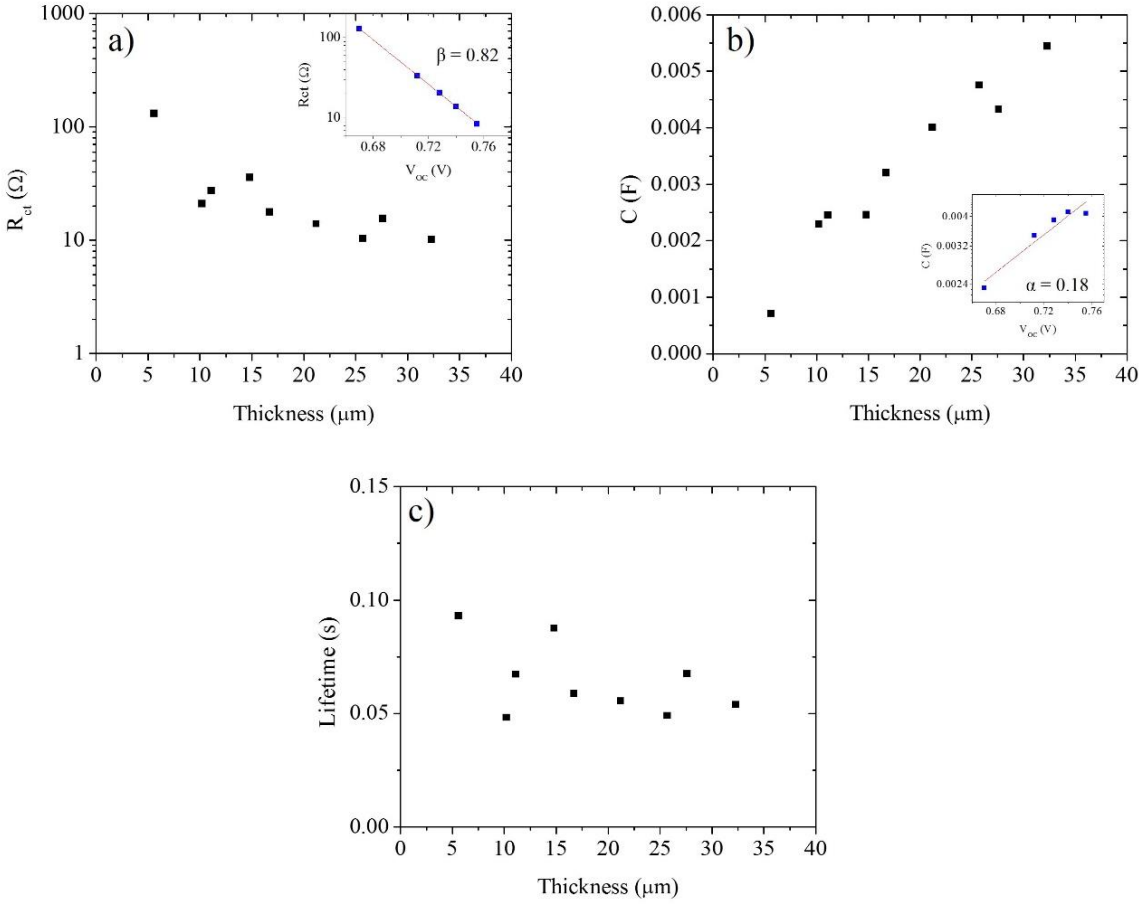

Figure 5.6. (**a**) Charge transfer resistance, (**b**) chemical capacitance and (**c**) electron lifetime obtained from EIS as a function of TiO_2 film thickness. The comparison was made at 0.74 V. The insets in (**a**) and (**b**) show the open circuit photovoltage dependence of the charge transfer resistance and chemical capacitance for the 21.2 μm solar cell, respectively; the corresponding values of the parameters α and β are shown.

In Figure 5.7, the series resistances of the cells versus film thickness are shown. The values of R_s were determined both by means of the diode equation and by EIS. From Figure 5.7 it can be concluded that as the thickness increases, the series resistance of the cell increases slightly as well. An increase of the series resistance is expected for thicker cells, hence reducing the efficiency somewhat[25,113,115].

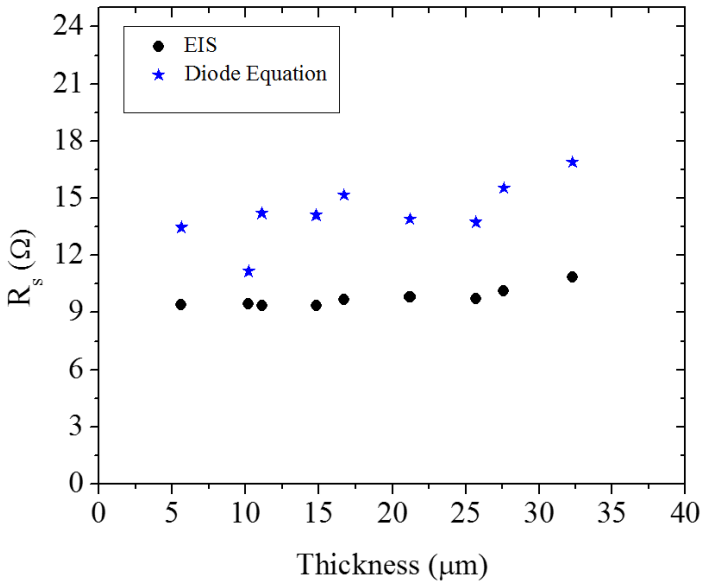

Figure 5.7. Comparison of the series resistances of the solar cells as a function of TiO_2 film thickness obtained by two different methods: steady state (blue dots) and small perturbation (dark dots) techniques.

Both experimental methods illustrate that the series resistance does not increase substantially, hence it is not a crucial parameter to determine an ideal film thickness for optimal cell performance. A small but significant difference is observed between the series resistance obtained by the diode equation and by EIS measurements. The series resistance obtained by means of Equation (5.3) includes the contributions from the active layer corresponding to r_{tr} and the contribution from the elements connected to the active layer, such as the FTO of the working and counter electrodes, contacts, and wires, and the electrolyte solution; the series resistance obtained by EIS is related only with the series resistance of the FTO[88]. The difference between both values can be observed in Figure 5.7.

As the thickness of the semiconductor film increases, the electrochemical system that is the cell becomes more complex and different parameters can have important influence on its performance. As mentioned in the introduction, one of those important parameters is the exchange current density in the dark, J_0, which is directly related with recombination as

shown in Equation (5.11). Using Equation (5.4), the values of J_0 were determined for all the cells as a function of TiO_2 film thickness. The experiments were performed under 1 sun illumination and the results are presented in Figure 5.8.

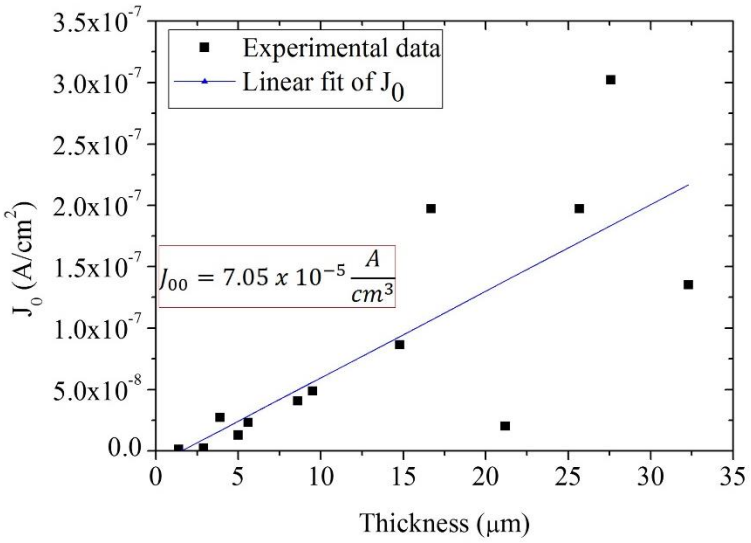

Figure 5.8. J_0 as a function of film thickness obtained by steady state measurements and the diode Equation (5.6) under 1 sun illumination. The slope represents J_{00}.

Figure 5.8 shows that the exchange current density in the dark, J_0, is approximately linear with respect to thickness, in agreement with what would be expected from Equation (5.12). However, it has to be taken into account that the step-wise process that has been used to prepare the films (alternating layer deposition and calcination) can lead to a non-negligible variation of the porosity of the film[75], which could explain the increased scattering of J_0 at larger thickness. Note, however, that the dependence of R_{ct}, C, and the lifetime on thickness imply that the morphology is essentially independent of thickness. According to Equation (5.12), the value of J_0 depends on the rate constant, k_0, for electron transfer from the TiO_2 to oxidized redox species in solution (recombination) or the oxidized dye, the intrinsic electron density in the film, n_0, and the electrode thickness, d; the value of J_0 should become larger

with increasing values of these parameters[120]. In a previous study of the influence of thickness in the distributed parameters of the cell by EIS, the results of Jennings *et al*[133] imply that the electron lifetime and, as a consequence, τ_0 are independent of electrode thickness. From Equation (A5.1) in the Appendix[122,129,130], taking a constant value for the porosity and assuming that $J_{sc} \propto d$, the value of n_0 will be independent of the electrode thickness. Since the value of k_0 and n_0 are independent of electrode thickness, then their product will also be independent of d. According to Equation (5.12), J_0 should follow a linear behavior with film thickness, as was also established by Zhu and coworkers[120]. The results in Figure 5.8 are in agreement with Zhu's approach, indicating that from the slope of Figure 5.8 we can obtain the value of J_{00}; this value is independent of TiO_2 film thickness. In order to determine the influence of J_0 on the performance of a DSC and using the diode equation (Equation (5.2)), J–V curves for different hypothetical cells are presented in Figure 5.9 and compared to experimental results. In Figure 5.9, experimental data obtained for the cell with thickness of 21.2 µm is compared with theoretical J–V curves. The red dots represent the experimental J–V curve for this cell under 1 sun illumination. The dark dots represent the J–V curve for this cell based on the super-position approximation, where the experimental J–V curve measured in the dark is shifted by the J_{SC} value obtained under illumination. Using Equation (5.4), the values for J_0 for these two curves were obtained, assuming the same values for the series resistance and β. Using these parameters and Equation (5.2), two J–V curves (yellow and gray lines in Figure 5.9) were simulated. Although the conditions in the dark and under illumination are different and this could lead to different values of R_s and β, they were kept constant to evaluate the influence of J_0 in the performance of the cell. These two curves were also simulated with the same values of J_0 and β but with a series resistances equal to zero.

For these 4 simulations the theoretical efficiency of the cells was calculated, and is presented in Table 5.1.

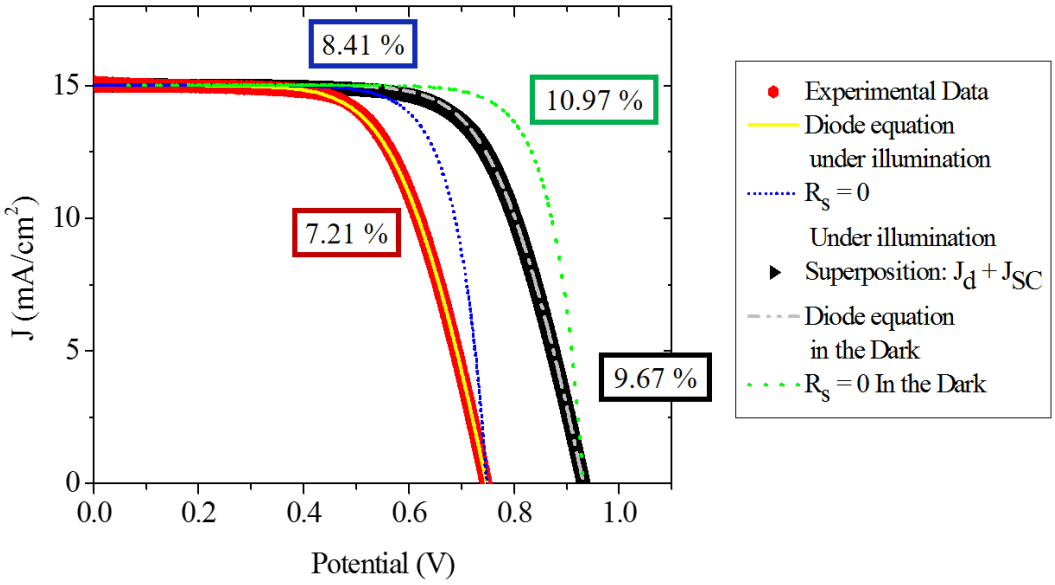

Figure 5.9. Comparison of the experimental J–V curve (Red dots) under 1 sun illumination obtained for the cell with thickness of 21.2 µm with calculated curves. The dark dots represent the J–V curve for this cell based on the super-position approximation, where the experimental J–V curve measured in the dark in is shifted by the J_{SC} value obtained under illumination.

Table 5.1 shows that the value of J_0 for the cell under dark conditions is lower than under illumination, assuming the same values for R_s and β in both cases. This difference in J_0 reflects the difference in recombination processes under light and dark conditions. The main difference between the conditions in the dark and under illumination is that under illumination, a variety of processes occur involving the dye and the redox couple, thus possibly changing the recombination dynamics. Upon illumination the dye is brought into an excited state, and subsequent ultrafast electron injection results in the generation of oxidized dye molecules. These oxidized dye molecules can be reduced back to their original state by either accepting an electron from the TiO_2 via the back reaction, which is a recombination

process[134], or by accepting an electron from the electron donor in the electrolyte solution, creating an increased local concentration of the electron acceptor. This, in turn, may also affect the recombination kinetics via the electron transfer from the TiO_2 to the electron acceptor in the solution[101].

Table 5.1. Comparison of experimental and simulated J-V curves with different values of J_0 and R_s.

21.2 µm Solar Cell Data	*Cell under Illumination*	*Cell under Illumination; $R_s = 0\ (\Omega)$*	*Superposition Approximation*	*Superposition Approximation; $R_s = 0\ (\Omega)$*
J_0 (A/cm^2)	2.01×10^{-8}	2.01×10^{-8}	7.2×10^{-10}	7.2×10^{-10}
J_{00} (A/cm^3)	9.47×10^{-6}	9.47×10^{-6}	3.4×10^{-7}	3.4×10^{-7}
R_s (Ω)	13.90	0	13.90	0
β	0.47	0.47	0.47	0.47
Efficiency (%)	7.21	8.41	9.67	10.97

The results in Table 5.1 suggest that these processes could be significant, which is reflected in an increase of the J_0 value under illumination. In the total density approximation (Equation (5.7)), recombination with the dye is implicitly considered when calculating the recombination constant. In contrast, in the diode equation, this effect is not explicitly considered but leads to a difference in J_0 between dark and illumination conditions. Figure 5.9 illustrates that this difference in J_0 values leads to a loss of photovoltage of almost 200 mV, which translates to a significant difference in the efficiency of the cell on the order of 2%–3%. This result strongly suggests that dye regeneration is a very important process in the

determination of the final performance of the cell, as has been argued by Jennings *et al*[132]. In addition, the results clearly lead to the conclusion that the superposition approximation does not hold. It is in fact well-known that the light J–V characteristics of DSCs cannot usually be predicted from the sum of the dark J–V and the short-circuit photocurrent (J_{sc})[129,132]. Barnes et al. examined differences between dark and light J–V curves of DSCs; they found that non-negligible recombination with the oxidized dye, together with local changes in electrolyte concentrations due to current flow, could explain their data[129]. If we take into consideration the influence of the series resistance of the solar cell we can observe in the J–V curves that decreasing R_s results in an increase of the fill factor and the efficiency of the cell. Even for the idealized curve under dark conditions, we can achieve a significant improvement on the efficiency of over 1%. This implies that if we can achieve a very small value of R_s together with a decrease in the value of J_0, the performance of the solar cell could be improved significantly. In order to compare the different methods proposed to obtain the exchange current density, the values of J_0 were also obtained from small perturbation techniques in the dark (EIS) and under illumination (EIS, IMVS, and IMPS), in accordance with Equation (5.12). The results are presented in Table 5.2. Applying the superposition approximation, the values of J_0 obtained from Equation (5.4) for a solar cell measured under illumination and in the dark are also presented. The most efficient cell (21.2 µm TiO_2 thickness) was employed for this analysis. From Table 5.2 it can be concluded that the values of J_0 obtained under illumination conditions via the small perturbation methods IMVS-IMPS and the steady-state J–V measurements according to Equation (5.4) are very similar. It can also be observed that the values for J_0 obtained under dark conditions via Equation (5.4) and the superposition approximation or EIS in the dark lead to practically the same value of J_0, however, J_0 in the dark is a factor 300 lower than under illumination. These results imply that the

approximations made with the continuity equation as a function of the total electron density are equivalent to the diode equation with respect to the determination of the J_0 value, and either of the two methods may be employed. Small perturbation methods therefore adequately show that the value of J_0 increases significantly under illumination, since the recombination processes are more significant under these conditions as discussed in the previous paragraph. Note that the results obtained by impedance measurements under illumination led to a different value of J_0 of about one order of magnitude lower, implying that the analysis method may not be accurate or that there are differences in conditions.

Table 5.2 Comparison between the values obtained for J_0 by different methods, both in the dark and under illumination.

21.2 µm Solar Cell Data	*Diode Equation under Illumination*	*Diode Equation with Superposition Approximation*	*IMVS and IMPS*	*EIS under Illumination*	*EIS in the Dark*
J_0 (A/cm^2)	2.01 x 10^{-8}	6.75 x 10^{-11}	1.17 x 10^{-8}	2.44 x 10^{-9}	9.44 x 10^{-11}
J_{00} (A/cm^2)	9.47 x 10^{-6}	3.19 x 10^{-8}	5.51 x 10^{-6}	1.15 x 10^{-6}	4.45 x 10^{-8}
Rs (Ω)	13.90	15.45	-	9.80	9.75
B	0.47	0.53	0.79	0.82	0.55

It has been suggested that J_0 ultimately determines the optimal film thickness for the best solar cell performance, because J_0 is an approximately linear function of film thickness[120]. In order to determine the parameters that can influence the optimum film thickness, and using

Equation (5.6) and the experimental values obtained and presented in Figure 5.8, power versus voltage plots were calculated as a function of film thickness with different values of J_{00}, α_{abs}, m, φ, and T (Table A5.2 and Figure A5.4 in the Appendix). From the power density vs. voltage plots, the maximum power point was obtained as a function of these parameters, and the results are shown in Figure 5.10 (a–d).

Figure 5.10 (a) shows the maximum power output of solar cells for three values of J_{00}. It can be observed that the optimum film thickness is around 10 µm, regardless of the value of J_{00}, implying that, although J_{00} is an important parameter for the performance of the DSCs, its value does not determine the optimum film thickness. From Figure 5.10 (b), it can be observed that regardless of the value of the ideality coefficient m, the behavior of the cells is the analogous to that of Figure 5.10 (a). Once again, the optimum film thickness does not change if the value of m is modified, and the optimal thickness remains at values of about 10 µm. When analyzing Figure 5.10 (b), it is very important to take into consideration that changing the value of β (or m) will lead to a change of the J_0 value, as can be observed in Equation 5.4 in agreement with the results reported by Fabregat-Santiago *et al*[88]. They found that a decrease in β value would lead to an increase on J_0 and a decrease in the performance and the fill factor of DSCs. In Figure 5.10 (c), cells with different values of α_{abs} are presented. The values of α_{abs} were taken from the absorption coefficient of the Z-907 dye adsorbed to the TiO_2 film for blue, green, and red light (wavelengths of 467, 525, and 625 nm, respectively). These results were compared with experimental data obtained from J–V curves for the cells under blue, green, and red LED illumination (Figure 5.10 (d)). It can be observed that the theoretical (Figure 5.10 (c)) and experimental (Figure 5.10 (d)) data show a different optimal film thickness for different illumination wavelengths, probably due to the use of

N719 dye in the experimental data. In spite of the differences in the actual value of optimal film thickness between theoretical and experimental data, the same tendency is observed: changing the value of α_{abs} changes the ideal thickness of the semiconductor film of TiO_2. The absorption length, which is the distance for which the light intensity decreases by a factor of 1/e, is inversely proportional to the value of α_{abs}.

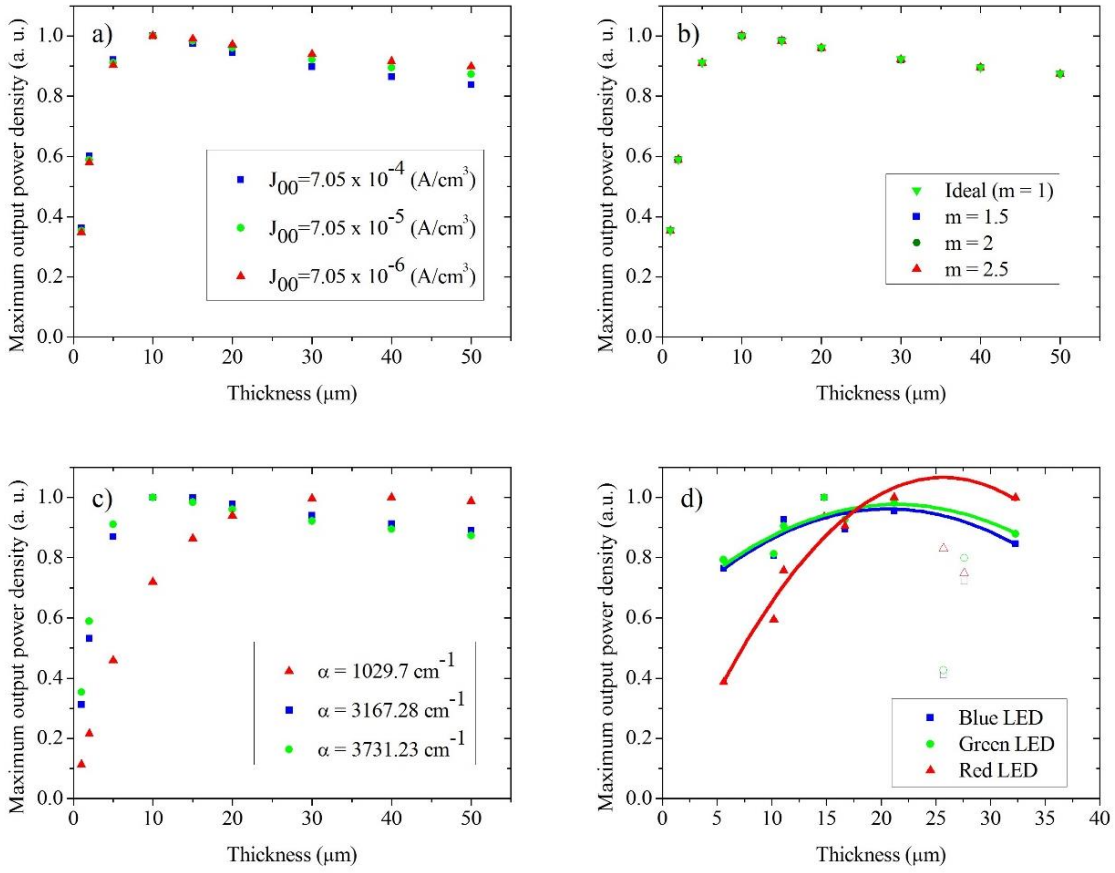

Figure 5.10. Maximum power density versus film thickness as a function of: (**a**) the value of J_{00} (α = 3731.23 cm^{-1}; m = 2; Φ = 2.62 x 10^{17} $cm^{-2}s^{-1}$; T = 0.9; R_s = 0 Ω); (**b**) the value of m (α = 3731.23 cm^{-1}; J_{00} = 7.05 x 10^{-5}; Φ = 2.62 x 10^{17} $cm^{-2}s^{-1}$; T = 0.9; R_s = 0 Ω); (**c**) the value of α_{abs} (m = 2; J_{00} = 7.05 x 10^{-5}; T = 0.9; R_s = 0 Ω; Φ_{C1} = 2.35 x 10^{17} $cm^{-2}s^{-1}$, Φ_{C2} = 2.62 x 10^{17} $cm^{-2}s^{-1}$, Φ_{C3} = 3.14 x 10^{17} $cm^{-2}s^{-1}$); (**d**) Wavelength of light; experimental data obtained for the cells under blue, green, and red LED illumination. Tendency lines are presented and the open dots were not taken into account in the calculation of the fit. Note that the value of α was taken according to the absorption coefficient of the Z-907 dye adsorbed onto films at 525 nm (green).

The value of α_{abs} for the green and blue wavelengths for the Z-907 dye is larger than that for red wavelengths. Therefore, the absorption length for blue and green light is smaller, leading to an optimum film thickness of around 10–15 μm, while for a value of α_{abs} for red light, the optimum film thickness is around 20–30 μm, approximately 2–3 times larger. This implies that the absorption coefficient of the cell and the irradiation wavelength that is applied to the solar cell ultimately determines the ideal thickness for DSCs. Gonzalez-Vázquez et al. established via random walk numerical simulation (RWNS) that the collection efficiency depends on the characteristic optical absorption length in the cells[135]. This result could have implications for the measurements of DSCs, especially using small perturbation techniques, which are often performed with a red LED light illumination. Since white light illumination (operating conditions) corresponds to smaller shorter absorption lengths than red light, the actual diffusion length of the cell under operating conditions could be overestimated when experimentally determined using red LED light illumination.

5.4.Conclusions

The exchange current density in the dark reflects the performance of DSCs, and decreasing its value led to an increase of 200 mV in theoretical cells. Although its value increases linearly with electrode thickness, is very susceptible to changes in porosity, increasing the difficulty to determine it for thick films ($d \geq 15$ μm). Differences in J_0 values between illumination and dark conditions were obtained, showing the fundamental differences in recombination processes under illumination and dark conditions. This result implies that the superposition approximation will not properly describe the J–V characteristics of the DSCs. Starting with the continuity equation as a function of total electron density, an expression of J_0 equivalent to the one deduced from the diode equation was obtained, and that allows to

determine J_0 via small perturbation techniques. Although J_0 depends on film thickness, it was shown that it does not determine the optimal film thickness of the DSCs, the value of α_{abs} being the one that determines the optimal film thickness in DSCs.

CHAPTER 6

DSCs with copper-based redox electrolyte

Because of an excessive loss of voltage during the dye-regeneration reaction, the use of iodide/triiodide electrolyte as a redox shuttle limits the attainable open-circuit potential to 0.7-0.8 V[22]. Copper-based metal complexes redox mediators are a real alternative since they present reduction potentials at a lower energy level than iodide/triiodide electrolyte (Figure 2.5) and are less aggressive toward metallic conductors[35]. However, electron transfer in the copper redox complex does not occur until the metal center is vibrationally excited to match a geometry appropriate for that of the product complex, and for copper such adjustment in the geometry usually requires a large energy because copper (I) and copper (II) have different preferred geometries, that is, tetrahedral and tetragonal, respectively. A distorted tetragonal geometry, which is an intermediate geometry between copper (I) and copper (II), was obtained for $Cu(dmp)_2$ by introducing methyl groups in the 2, 9 positions of phenanthroline ligand[38]. With this copper redox couple, Hattori *et al* obtained cells with high photovoltage, but with only 1.4% efficiency[38]. Based on the same copper (I/II) electron mediator Bai *et al* improved the power conversion efficiency to 7.0% at 1 sun illumination[35]. These results highlight the potential for these new copper redox couples. However, when working with alternative redox couples, mass transport problems associated with their diffusion inside the DSC, mainly in the mesoporous layer, have limited the solar cell performance[32,93,94]. It has been stated that mass transport limitation may also become noticeable when the distance between electrodes is increased[136]. The highest efficiency in DSCs has recently reported to

be 14.3% at one sun illumination intensity[28]. In their work, Kakiage *et al* presented a DSC where the electrodes were held to a minimum distance, increasing the fill factor and the overall performance of the solar cells. However, in the so called "open sandwich cell configuration" the DSCs are not sealed and broad characterization becomes difficult. In this chapter a copper-based electrolyte solution, $[Cu(dmp)_2]^{+/2+}$, is employed and studied for DSCs. A study of the influence of the distance between electrodes on the mass transport and performance of the copper-based solar cells is performed and a sealed cell configuration with the lowest possible separation between electrodes is proposed. All the work presented in this chapter was made in the Department of Chemistry, in Uppsala University, Sweden, under the supervision of Professor Gerrit Boschloo.

6.1.Experimental procedure

Three different DSCs configurations were prepared in this study (Figure 6.1) and at least five cells for each configuration were prepared:

a) *Surlyn cells:* Standard DSCs with a (5.3 ± 0.3) µm thick transparent TiO_2 mesoporous layer sealed with a 30 µm Surlyn thermoplastic polymer.
b) *Epoxy-TiO_2 cells:* DSCs with a (5.3 ± 0.3) µm thick transparent TiO_2 mesoporous layer sealed with epoxy resin.
c) *Epoxy-ZrO_2 cells:* DSCs with a (5.3 ± 0.3) µm thick transparent TiO_2 mesoporous layer and an additional 0.4 µm thick ZrO_2 insulating layer sealed with epoxy resin.

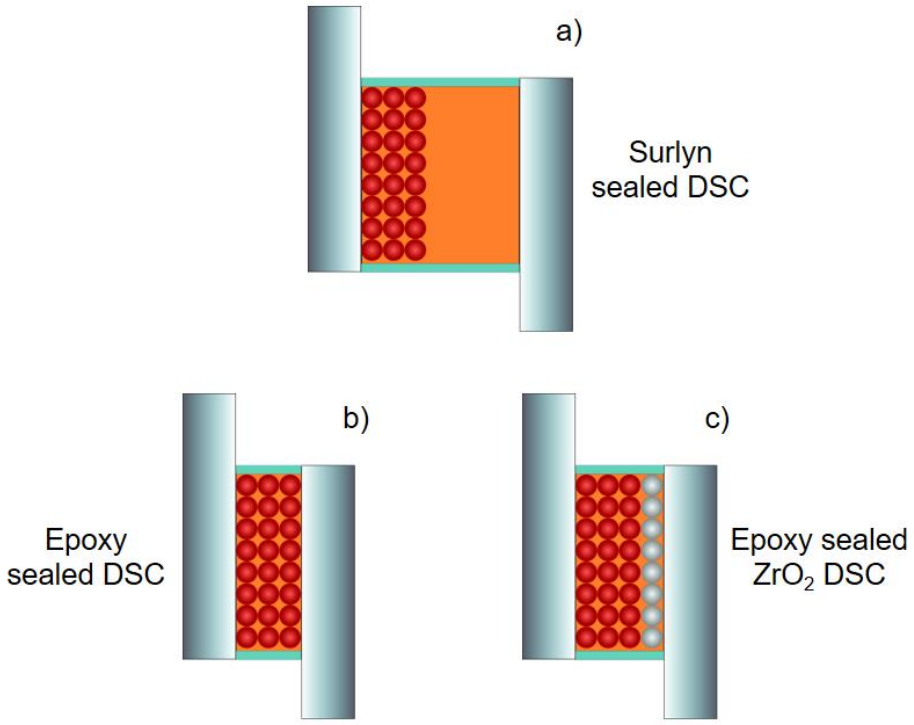

Figure 6.1. Different DSC configurations. (**a**) Surlyn cell, (**b**) Epoxy-TiO_2 cell and (**c**) Epoxy-ZrO_2 cell. In (**c**), the additional ZrO_2 layer, although sensitized, is represented as gray spheres.

Preparing the working electrodes for DSCs

To prepare the DSC working electrodes, fluorine-doped tin oxide (FTO) glass is used as current collector (TEC15). The FTO glass was cleaned in a detergent solution (RBS25, 99%, Fluka) in an ultrasonic bath for 60 min, and then rinsed with water. The FTO glass was then submerged sequentially in deionized water and ethanol for 60 min in an ultrasonic bath, rinsed with water and dried in air. Once dry, they were submerged in a 40 mM aqueous $TiCl_4$ solution and heated to 70 °C for 90 min and then rinsed with water and ethanol. After drying in air, the substrates were screen printed with a 60 wt% TiO_2 paste (Dyesol DSL 18 NR-T) diluted with a 90 wt% terpineol and 10 wt% ehtylcellulose solution. The screen printed area for each substrate was 0.25 cm^2. After every deposition, the electrodes were heated to 120 °C for 6 min and they were taken to room temperature before they could be screen printed

again. After the screen printing, the electrodes were heat treated in an oven (Nabertherm Controller P320) according to the temperature ramp presented in Figure 6.2.

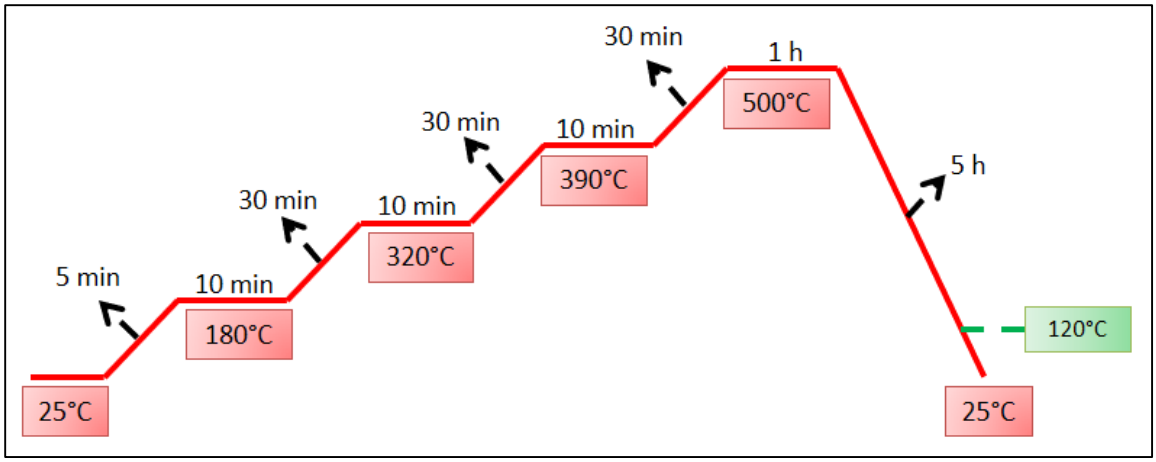

Figure 6.2. Sintering temperature ramp for the 0.25cm^2 working electrodes. When films are heat-treated prior to dye loading, the process is halted at 120 °C.

After the heat treatment, the electrodes were submerged in a 40 mM aqueous $TiCl_4$ solution and heated to 70 °C for 30 min, rinsed with water and ethanol, dried to air and stored. For the epoxy ZrO_2 cells, an additional ZrO_2 screen printed layer (Sigma-Aldrich nanoparticles dispersion < 100 nm particle size, 10 wt% in H_2O) was applied after the second $TiCl_4$ treatment. After the deposition of the ZrO_2 layer, the electrodes were heat treated again according to the temperature ramp presented in Figure 6.2. No scattering layer was used in the preparation of any of the DSCs. To sensitize the working electrodes, they were heated to 500 °C for 30 min and then cooled to 120 °C for 2h and then submerged in a dye bath with a concentration of 0.2 mM LEG4 dye (6.2) in *tert*-butanol/acetonitrile (1:1, v/v). The electrodes remained in the dye bath overnight to allow complete dye uptake in the mesoporous layer. After sensitization, the electrodes were rinsed with acetonitrile and dried in air.

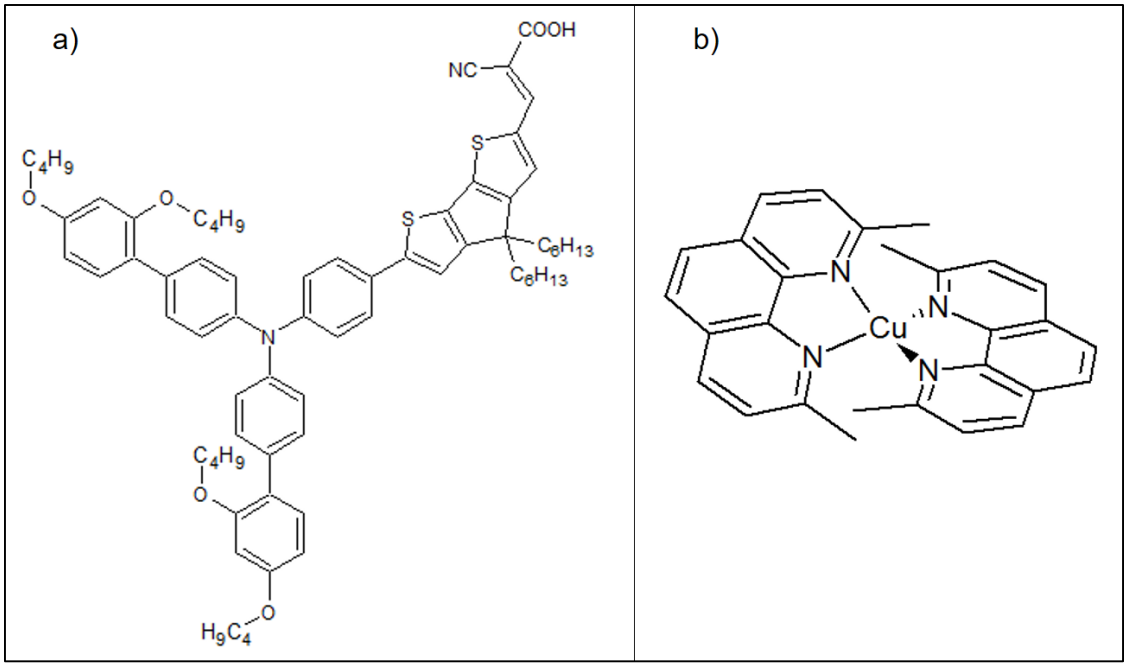

Figure 6.3. Chemical structures of (**a**) LEG4 and (**b**) $Cu(dmp)_2$[34,76,84].

Poly(3,4-ethylenedioxythiophene) (PEDOT) counterelectrodes

PEDOT counter electrodes (≈200 nm) were prepared according to the procedure published by Ellis *et al*[73]. A solution containing 0.1 M of sodium dodecyl sulfate (SDS) and 0.01 M of 3,4-ethylenedioxythiophene (EDOT) in water was used as the electropolymerization solution. Both compounds were sonicated for 1 hour in order to properly dissolve them. Electropolymerization of EDOT was performed with an IviumStar.XR (Ivium Technologies) electrochemical instrument in the galvanostatic mode; a two-electrode cell with a (9 x 6) cm^2 conducting glass as counter electrode and a predrilled (5 x 5) cm^2 TEC8 glass as working electrode was used for this purpose, and a constant current of 13 mA was applied during 25 s. After deposition, the electrodes were rinsed with water and ethanol and dried in air.

Sealing of DSCs

Two different sealing methods were compared in this study. In the first method, the sensitized electrodes and PEDOT counter electrodes were sealed together using a 30 µm thick

thermoplastic polymer Surlyn frame. An electrolyte solution was then injected through one hole predrilled in the PEDOT counter electrode and the hole was sealed with 60 µm thick thermoplastic polymer Surlyn cover and glass coverslips. The second sealing method is depicted in Figure A6.1 in the Appendix. A 1:1 (v/v) mixture of Solaronix Amosil 4R [Bisphenol-A-(epichlorhydrin) epoxy resin] and 4H (2,2'-iminodiethylamine) was prepared separately (Figure A6.1 (a)). The working and counter electrode were pressed against each other (Figure A6.1 (b)). Using paper clamps to keep together the electrodes, the epoxy resin was applied on the edges where the two electrodes meet (Figure A6.1 (c)). Once the epoxy resin was applied, the cells were kept under constant pressure (Figure A6.1 (d)) and put inside a desiccator under dark conditions, where the resin cured overnight (Figure A6.1 (e)). Once the resin was cured, the cells were filled with the electrolyte solution and they were sealed with 60 µm thick thermoplastic polymer Surlyn cover and glass coverslips (Figure A6.1 (f)). The composition of the electrolyte solution was 0.2 M $Cu(dmp)_2TFSI$, 0.05 M $Cu(dmp)_2TFSI/Cl$, 0.1 M LiTFSI and 0.5 M *tert*-butylpyridine (TBP) in acetonitrile (TFSI: bis(trifluoromethane) sulfonamide).

Solar cell characterization

Current-voltage (IV) characteristics of the solar cells were obtained with a Keithley 2400 source/meter and a Newport solar simulator (model 91160). The light intensity was calibrated using a certified reference solar cell (Fraunhofer ISE) to an intensity of 100 mW/cm^2. For the J-V measurements, a black mask of (0.5 x 0.5) cm^2 was employed in order to avoid additional contributions of scattered light in the glass. For incident photon to current conversion efficiency (IPCE) measurements, a computer-controlled setup with a xenon light source (Spectral Products ASB-XE-175), a monochromator (Spectral Products CM 110), and a

Keithley 2700 multimeter were used. Electrochemical impedance spectroscopy and cyclic voltammetry measurements were performed using a computer controlled electrochemical instrument (AutoLab PGSTAT100) incorporating a frequency response analyzer. EIS measurements were performed under illumination conditions using an AC amplitude of 10 mV in the 0.1 Hz to 100 kHz frequency range. The electrochemical impedance spectrum was analyzed using Z-View software and two different equivalent circuits, one of them proposed by Fabregat-Santiago *et al* (Figure 3.8)[88,101] and a second one with an additional component proposed in this work (Figure 6.4).

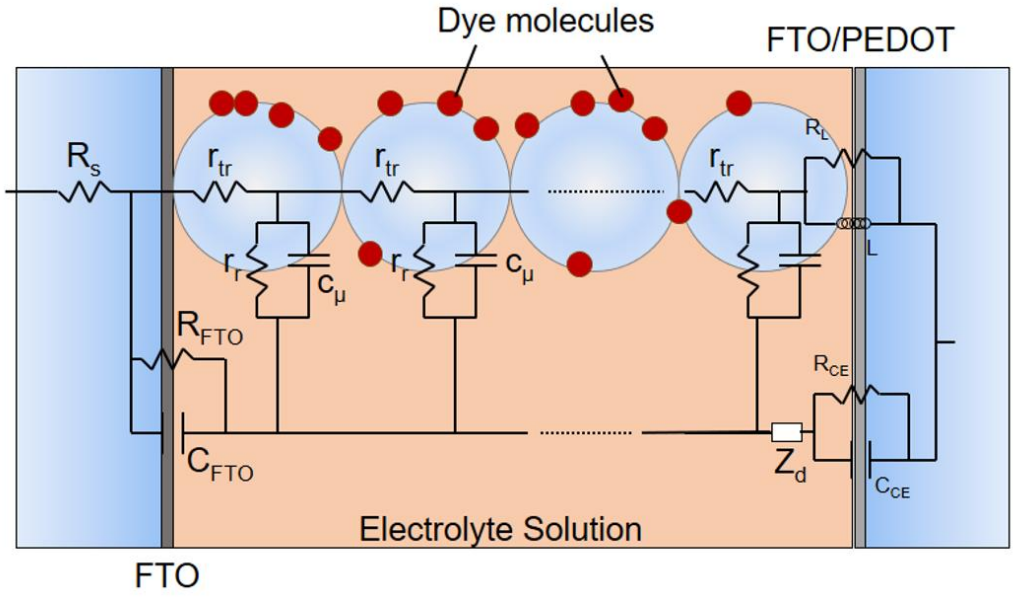

Figure 6.4. General equivalent circuit model proposed to fit impedance spectroscopy results for Epoxy-TiO_2 cells. R_L and L represent the interaction between electrons in the TiO_2 and the PEDOT counter electrode.

Cyclic voltammetry was employed to determine the redox potential of the copper-based redox couple, using a solution of 3 mM of $Cu(dmp)_2TFSI$ in a 0.014 M LiTFSI solution in acetonitrile, scanning from 0 to 1 V with a 2 mV step potential and a scan rate of 100 mV/s. The diffusion coefficient was determined using the relationship between scan rate and peak current[137]. The scan rates employed were 25, 50, 75, 100, 150 and 200 mV/s, using gold,

graphite and Ag/AgCl as working, counter and reference electrode, respectively. The redox potential was calibrated versus a normal hydrogen electrode (NHE) by the addition of ferrocene as an internal standard, taking $E^0(Fc/Fc^+)$ = 0.63 V vs NHE[30,42]. Dye loading was estimated from dye desorption measurements. The sensitized electrodes were immersed in dye baths with a concentration of 0.2 mM LEG4 in *tert*-butanol/acetonitrile (1:1, v/v). After sensitization the samples were put in alkaline solution consisting of 0.05 *tetra*-butyl ammonium hydroxide (TBAOH) in ethanol to desorb the dye. The dye coverage was estimated using the Lambert-Beer law (Figure A6.2 and Table A6.1 in the Appendix). The UV-Vis absorption spectra of the dye desorbed solutions were recorded with an Ocean Optics HR2000 spectrometer and a Micropack DH-2000-BAL light source. The thickness of the TiO_2 nanoparticulate film was measured using a Dektak3 surface profilometer (Sloan technology). To determine the separation between the electrodes, 20 assemblies composed of a (6.9 ± 0.1) µm thick transparent TiO_2 mesoporous layer deposited on regular glass were fabricated; 10 of these assemblies were sealed with Surlyn polymer and a piece of glass and the other 10 were sealed with epoxy resin and a piece of glass. The thickness of each FTO and the thickness of the hole assembly was determined 10 times for each one of the cells using a micrometer with a ratchet knob and the average and standard deviation was obtained for each configuration. Turn-on photocurrent transients were measured under white LED illumination, short circuit condition and at room temperature. The illumination intensity was calibrated using a certified reference silicon photodiode (Fraunhofer ISE), to produce the same photocurrent as under equivalent Sun AM 1.5 illumination; various sun intensities were tested, which ranged from 0.1 Sun to 3 Suns. Stepped illumination (1 s off, 5 s on and 0.5 s off) was synchronized with data acquisition using a programmable power supply, fast solid state switches and an in-house built data acquisition setup. Additionally, J-V curves were

also measured at various light intensities (0.1 Sun to 3 Suns), using white LED illumination. The scan rate was 0.1 V/s and the voltage step was 10 mV. J-V curves were scanned cyclically from 0 V to 1.2 V forward bias to -0.1 V and return.

6.2. Results and discussion

From Figure 6.1 the main differences between the different DSC configurations can be appreciated. In Figure 6.1 (a) a typical DSC configuration, sealed with Surlyn polymer, is presented. In Figure 6.1 (b) the same DSC structure is used, but the distance between the working and counter electrode has been reduced due to the sealing method. In this configuration, the electrolyte solution is only present in the pores of the mesoporous layer and the redox species travel only through this intricate network. However, due to direct contact between the mesoporous layer and the counter electrode, the cell may become shunted. In order to avoid possible shunting of the cell, the third configuration, presented in Figure 6.1 (c), is employed. In this configuration, an additional insulating layer of mesoporous ZrO_2 is applied over the mesoporous TiO_2. ZrO_2 layers are usually applied in solid-state DSCs to avoid direct recombination pathways between the TiO_2 and the hole transport material[106].

A customized assembly with a (6.9 ± 0.1) µm thick transparent TiO_2 mesoporous layer was sealed either with Surlyn polymer or with epoxy resin and the separation between electrodes was determined with a micrometer for both configurations. The results show a separation of (21.9 ± 1.9) µm and (7.4 ± 1.0) µm for the Surlyn and epoxy configurations, respectively. These measurements show that the separation between FTO glass electrodes in the so called "epoxy cells" is basically the thickness of the mesoporous transparent layer. The difference between the separation of electrodes of the epoxy cells and the average value of thickness of

the mesoporous layer can be attributed to the thicker edges usually present in screen printed samples, which determines the ultimate separation in epoxy cells. The separation between the last layer of mesoporous TiO_2 in the working electrode and the PEDOT counter electrode in cells sealed with Surlyn polymer will be around 16 – 17 µm whereas for the epoxy cells, there will be virtually no separation.

Determination of the redox potential and diffusion coefficient of the redox couple was obtained with cyclic voltammetry and the results are presented in Figure 6.5.

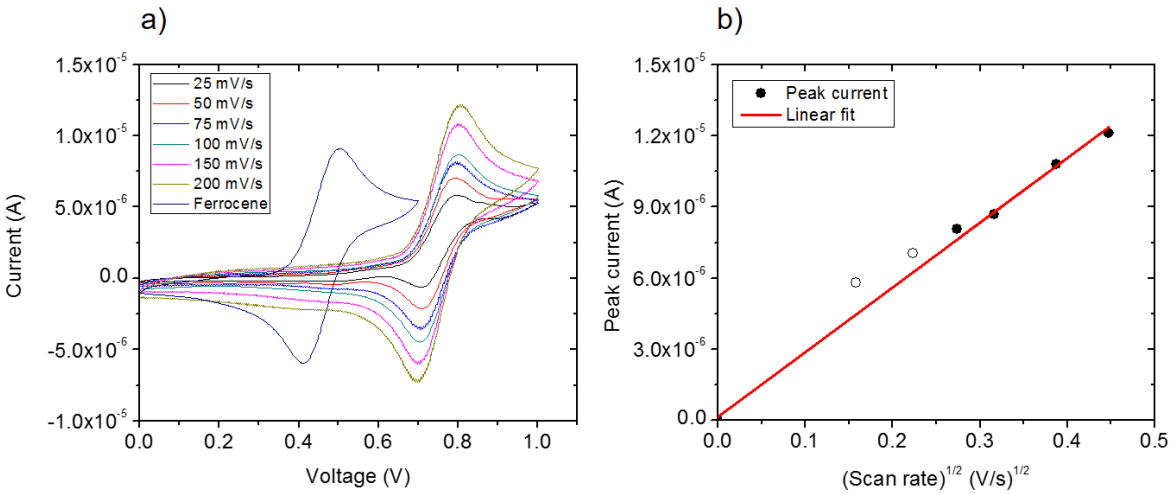

Figure 6.5. (**a**) Cyclic voltammogram of 3 mM $Cu(dmp)_2TFSI$ in 0.014 M TFSI solution in acetonitrile with different scan rates: 25, 50, 75, 100, 150 and 200 mV/s. The cyclic voltammogram for Fc/Fc^+ (0.63 vs NHE) was used to calibrate the reference electrode potential before the experiments and is also presented in the figure. In (**b**) the diffusion coefficient was calculated using the Randles-Sevcik relationship[137] between scan rate and peak current (eq. 6.1); the white dots represent the values of the peak current for the 25 and 50 mV/s scan rates, which were not considered in the fit. The area of the working electrode was 3.1 x 10^{-2} cm^2.

From Figure 6.5, the redox potential of the copper-based redox couple was determined to be 0.924 V vs NHE in acetonitrile, which is a very similar value to the one reported by Hattori

et al for a similar copper redox couple[38]. The value of the diffusion coefficient for this redox couple in the bulk, was obtained according with the Randles-Sevcik relationship:

$$I_p = (2.69 \times 10^5) n^{3/2} A D_0^{1/2} v^{1/2} C_0^* \quad (6.1)$$

where i_p is the peak current in A, n is the number of electrons involved in the redox reaction, A is the area of the working electrode in cm^2, D_0 is the diffusion coefficient of the redox species, v is the scan rate in V/s and C_0* is the bulk concentration of the redox species in mol/cm^3. The value obtained for the diffusion coefficient was $D_0 = 1.2 \times 10^{-6}$ cm^2s^{-1}. This value is lower than the values usually reported for iodine and cobalt redox couples in acetonitrile[32,36,41,77,93]. This implies that the diffusion coefficient in the bulk is a parameter to take into consideration when working with $Cu(dmp)_2$ based DSCs.

The influence of the separation between electrodes in the J-V parameters of the cells is summarized in Table 6.1 and Figure 6.6.

Table 6.1. Average values of the J-V parameters for the Surlyn, Epoxy-TiO_2 and Epoxy-ZrO_2 cells.

Cell	*V_{oc} (V)*	*J_{sc} (mA/cm^2)*	*FF*	*Efficiency (%)*
Surlyn	1.034 ± 0.005	9.76 ± 0.26	0.64 ± 0.01	6.4 ± 0.2
Epoxy-TiO_2	0.904 ± 0.020	11.69 ± 0.37	0.74 ± 0.01	7.8 ± 0.4
Epoxy-ZrO_2	1.010 ± 0.007	10.77 ± 0.43	0.73 ± 0.01	7.9 ± 0.2

The value of the redox potential of the copper electrolyte lead to a high value of the open circuit potential for the DSCs, which is shown in Figure 6.6 (a), where particularly the Surlyn and epoxy-ZrO_2 cells present values over 1 V. However, the cells sealed with epoxy resin without the ZrO_2 layer have a lower V_{oc}. This is attributed to the contact between the mesoporous TiO_2 layer and the PEDOT counter electrode. This contact may be a pathway of recombination of electrons photogenerated in the outer layer of TiO_2, which reduces the maximum attainable potential in the DSC. When the additional ZrO_2 layer is applied, there is no loss in the photovoltage value of the cell, since this insulating layer avoids the loss of electrons to the counter electrode.

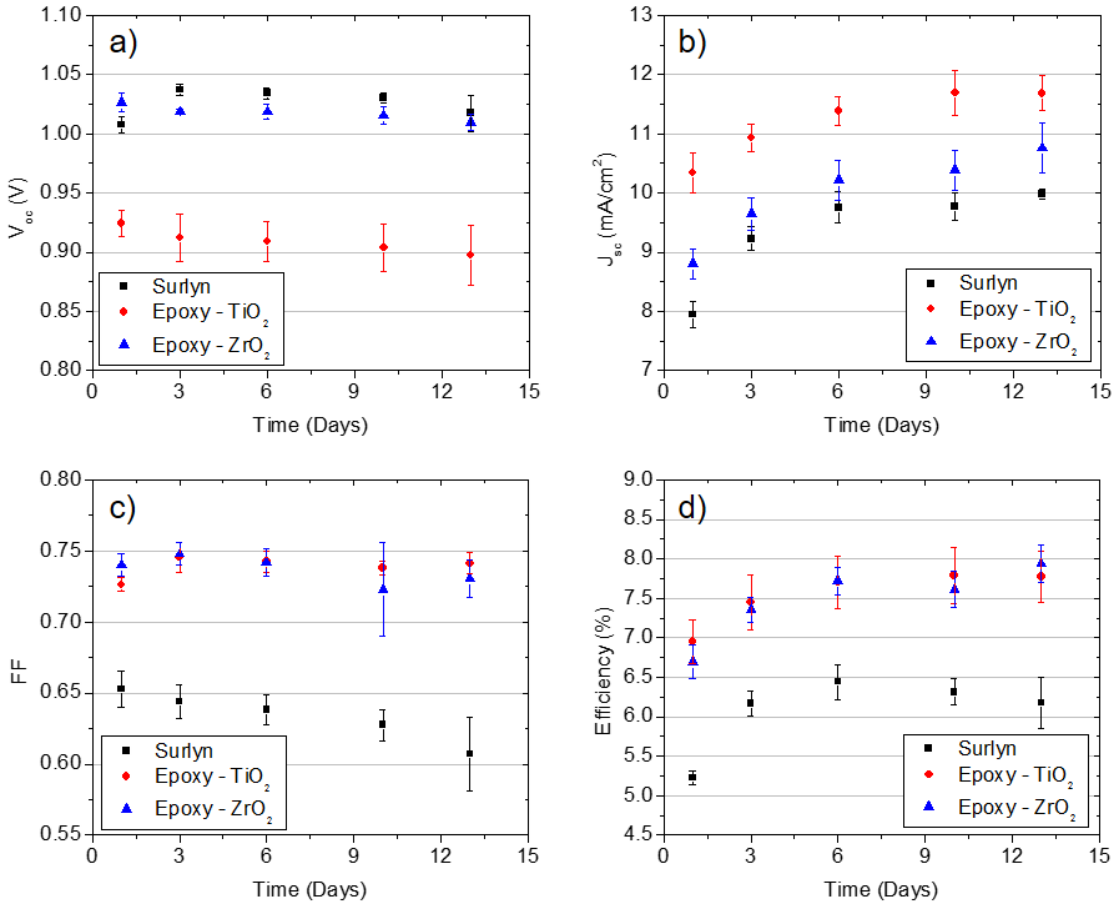

Figure 6.6. Current-voltage parameters over time for Surlyn, Epoxy-TiO_2 and Epoxy-ZrO_2 cells. (**a**) V_{oc}, (**b**) J_{sc}, (**c**) FF and (**d**) efficiency.

In spite of losing almost 100 mV in the epoxy-TiO_2 cells in comparison with the other two configurations, the current density attainable for this cell is the highest, as can be observed in Figure 6.6 (b). The reduction of separation of electrodes decreases the distance the redox couple has to diffuse to regenerate the dye and regenerate itself, and it also may affect the mass transport limitations of the cell[136]. Both differences will increase the current density attainable for this configuration. However, when the cells sealed with epoxy resin are compared, it is observed that the cells with the additional ZrO_2 layer present a lower photocurrent. From the dye desorption measurements presented in the Appendix (Figure A6.2 and Table A6.1) it can be concluded that this difference in photocurrent is not related with dye adsorption by the mesoporous layer, since the cells with the ZrO_2 layer adsorbed more dye than the bare TiO_2 cells. This implies that, although the ZrO_2 layer may adsorb dye molecules, there is no additional photogeneration of electrons due to the position of the conduction band of this insulating layer[62,63,106]. This decrease in J_{sc} value has already been observed in solid-state DSCs, where Li *et al* attributed it to an excessive ZrO_2 coverage which inhibits electron injection by the photoexcited dye into TiO_2[106]. Another reason for the lower value of photocurrent is the increase of thickness of the mesoporous layer, which will increase the diffusion distance of the redox couple, reducing the attainable photocurrent. One of the most noticeable improvements when the distance between electrodes is reduced is in the values of the fill factor, which are displayed in Figure 6.6 (c) and in Table 6.1. Here, an increase of 0.10 in the fill factor value occurs when changing the configuration of the cell from Surlyn polymer to epoxy resin. The average fill factor value obtained for the epoxy cells is just below 0.75, and this value is very stable over time. This increase in fill factor can be attributed to a decrease in series resistance associated to the electrolyte solution inside the cell. Finally, the average efficiency values are presented in Figure 6.6 (d) while the J-V

curves for the best cells of each configuration are presented in Figure 6.7. Both configurations of epoxy cells give the same overall performance, reaching values as high as 8.2%, even though they have different V_{oc} and J_{sc} values. However, due to direct contact between the mesoporous TiO_2 layer and the counter electrode some of the epoxy-TiO_2 presented shunting behavior, as is reported in Figure A6.3 in the Appendix, while the epoxy-ZrO_2 cells never presented this type of behavior, making them the more reliable option.

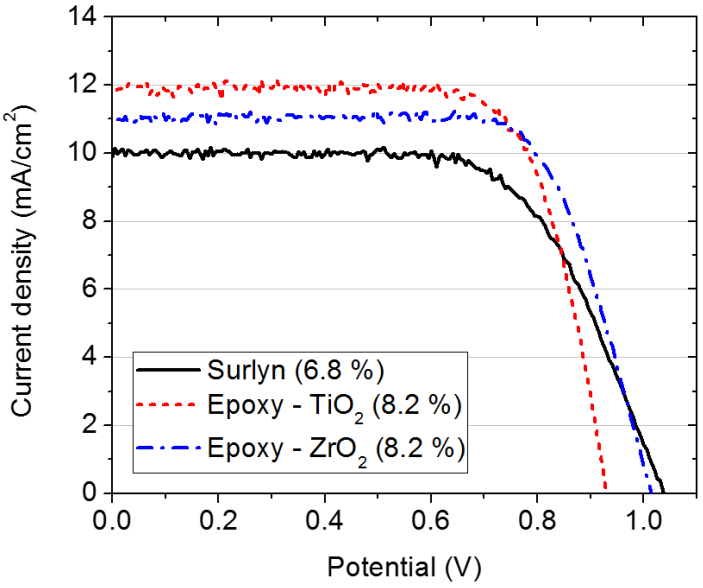

Figure 6.7. J-V curves for the best cell of each configuration. The efficiency values are also displayed.

In Figure 6.8, the IPCE measurements are presented. Since the cells contain the same dye, the light harvesting efficiency should be the same for the different configurations, however, a difference in IPCE between the different cell configurations can be distinguished. The overall IPCE is higher for cells sealed with the epoxy resin, especially for the cells without ZrO_2. Epoxy-ZrO_2 cells present very similar IPCE spectra as observed for the Surlyn cells. From J-V measurements it is observed that the epoxy-TiO_2 cells present a lower V_{oc}, probably due to interaction between electrons in the outer mesoporous layer and the counter

electrode. However, the overall IPCE is higher in this configuration, probably due to a higher collection efficiency. The current could also increase due to a higher regeneration efficiency of the dye. The dye regeneration efficiency may be affected by mass transport difficulties of the redox couple and this could be indirectly observed by the limiting current obtained when measuring reverse bias and also with transient photocurrent measurements[93].

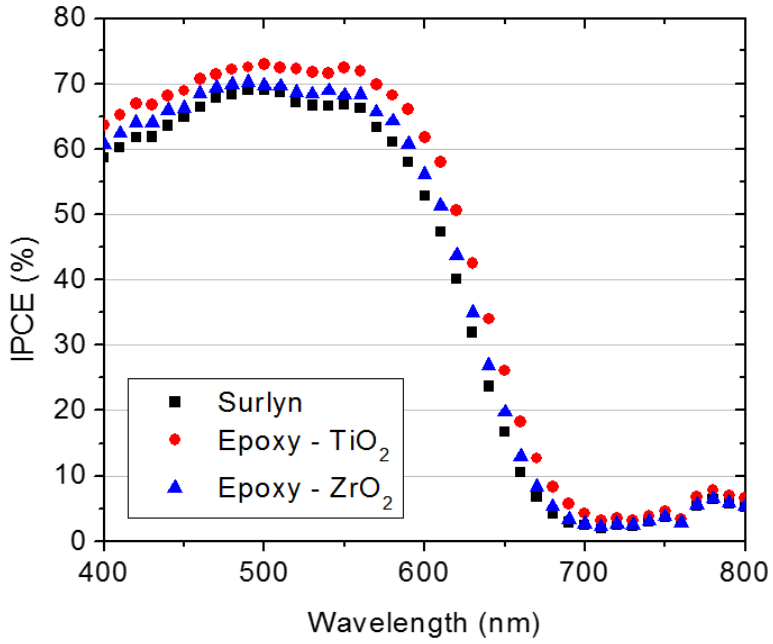

Figure 6.8. IPCE for different cell configurations.

The reverse bias measurements applied to the three different configurations are presented in Figure 6.9. A remarkable difference between cell configurations can be observed in Figure 6.9. Here, the limiting current value obtained for Surlyn cells is lower than half the value obtained for the epoxy-ZrO_2 cells. This implies that the diffusion of the $Cu(dmp)_2$ redox couple in the bulk may be an important factor limiting the attainable current in the device, when usually the diffusion of the redox couple in the mesoporous layer is the only factor considered. When using epoxy cells there is an important increase in the limiting current, suggesting that mass transport limitation can be altered when decreasing distance between

electrodes. When comparing epoxy-TiO_2 and epoxy-ZrO_2 cells, the limiting current for the latter seems to be somewhat lower, while no limiting current value seems to be reached for the former, even at potentials as high as 1.6 V. This difference between both epoxy configurations may be due to the extra ZrO_2 mesoporous layer, which increases the thickness of the mesoporous layer, the distance between electrodes and may start to present mass transport problems.

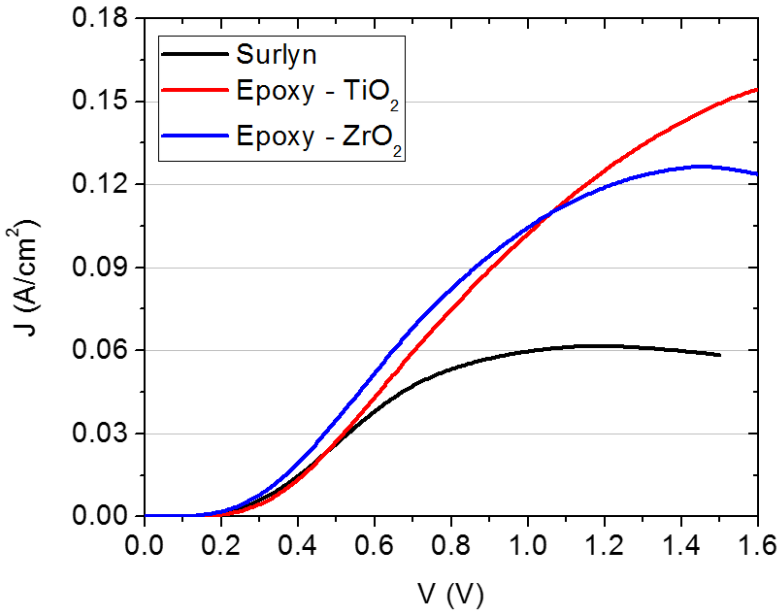

Figure 6.9. Reverse bias measurements for the different cell configurations.

In order to study mass transport limitation in the different cell configurations, transient photocurrent measurements, conducted at short circuit, were employed and are displayed in Figure 6.10. From Figure 6.10 (a) and (b) it is observed that none of the cells present mass transport limitation under low light intensity. However, at 1 sun, Surlyn and epoxy-ZrO_2 cells start to display mass transport limitation in comparison with epoxy-TiO_2 cells, although the difference between currents is not very high. This phenomenon becomes more visible when

the cell is under higher light intensity, where Surlyn cells present a higher difference between peak and steady-state current density, while for the epoxy cells, this difference is smaller.

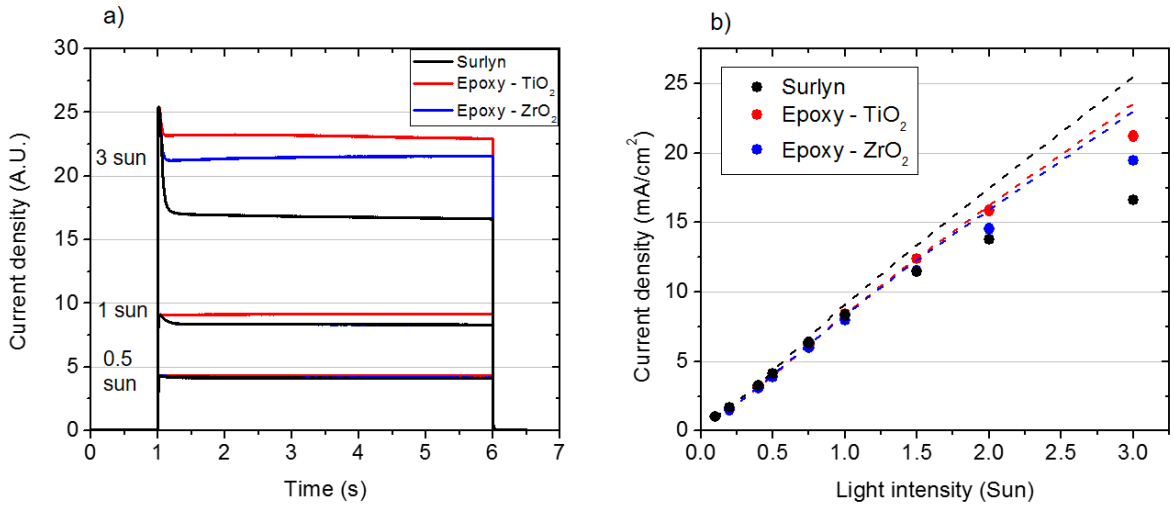

Figure 6.10. (**a**) Transient photocurrent measurements. The values of current density were normalized to the same peak current value at different light intensities. (**b**) Representation of peak and steady-state currents against light intensity obtained from transient photocurrent measurements. The dashed lines represent the peak current density; the dots represent the steady-state current density.

In Figure 6.10 (b) it is observed that even at 3 suns illumination intensity, the deviation from linearity of the epoxy cells is substantially reduced when compared with Surlyn cells and that, in general, epoxy cells present a linear dependence of current density with light illumination even at 2 suns illumination intensity. These results suggest that the photocurrent under full sunlight illumination may be limited by the mass transport of copper cations in the bulk, as it has been already established by Bai *et al*[35], and reducing distance between electrodes may improve the current attainable in the cell by reducing mass transport limitation.

An impedance analysis was employed in all cell configurations, and the Nyquist plots are displayed in Figure 6.11. For the Surlyn cells two main semicircles can be observed if the

semicircle associated with the counter electrode, which appears at high frequencies, is not considered. The first semicircle is associated with transport and recombination in the mesoporous layer and the second one is usually related with diffusion of the redox couple inside the cell[23,88,89,101,113,115,125,138]. In this plot it is clear that the impedance corresponding to diffusion of the redox couple is very high, contributing to the magnitude of the impedance at low frequency values.

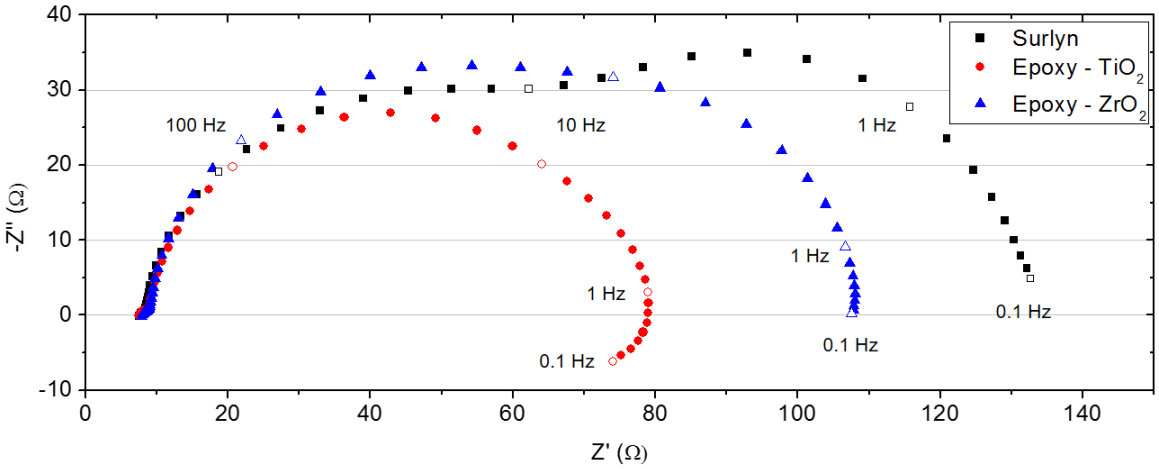

Figure 6.11. Nyquist plots for the Surlyn, epoxy-TiO_2 and epoxy-ZrO_2 cells. The measurements were made at open circuit potential for each cell. Data measured at 0.1, 1, 10 and 100 Hz is highlighted.

Analyzing the Nyquist plot for the epoxy-ZrO_2 cell configuration, it is clear that the behavior is different than for the Surlyn cell. The Nyquist plot for this configuration seems to be composed of two merged semicircles, where the second one, related to the diffusion of the redox couple, is smaller than the one present in the Surlyn cells. This may be related with the decrease of the distance between electrodes, which alter mass transport limitation inside the cell and reduces the total impedance at low frequencies. However, the additional ZrO_2 layer seems to contribute to mass transport limitation since the second semicircle still has an important contribution to the total impedance value. In the plot for the epoxy-TiO_2 cell, the

second semicircle does not appear but instead a negative capacitance seems to be present at low frequencies. This type of negative capacitance has already been reported for other types of solar cells[103–105], including solid-state DSCs[103,106,107]. This negative capacitance has been associated with conductivity modulation due to injection of minority carriers[107,108], loss of interface charge at occupied states below the Fermi level[104], an additional recombination pathway that opens up at forward bias and decreases the charge accumulation ability of the solar cell[103] and also to a charge transfer process between two electronic reservoirs governed by the occupation of an intermediate state, which becomes saturated and limits the kinetics of the process[103,106]. Li *et al*[106] found experimental evidence that the spatial origin of the negative capacitance at low frequencies of nanostructured solar cells is at the metal oxide/hole conductor interface in solid-state DSCs. In our work, this inductive behavior only appears for the epoxy-TiO_2 cells and disappears once a layer of ZrO_2 is applied into the DSC, the same way as Li *et al* reported for ssDSCs[106], where they claimed that charge transfer via surface states can account for the existence of this inductive effect at low frequencies and may limit the performance of the solar cells. This is a clear indication that this negative capacitance is due to the direct interaction between electrons in the TiO_2 mesoporous layer and the PEDOT counter electrode and separating them with an insulating layer (ZrO_2), suppresses completely this negative capacitance behavior at low frequencies. We propose that due to contact between these two layers there is an additional recombination pathway that decreases the charge accumulation ability of the solar cell, implying a negative capacitance, as Mora-Seró *et al* proposed when working in solid state solar devices[103]. This negative capacitance is simulated in the proposed equivalent circuit (Figure 6.4) by the use of an inductive element and the fitting results are displayed in Figure 6.12 where it can be observed that the fit of the equivalent circuit reproduces quite well the experimental values.

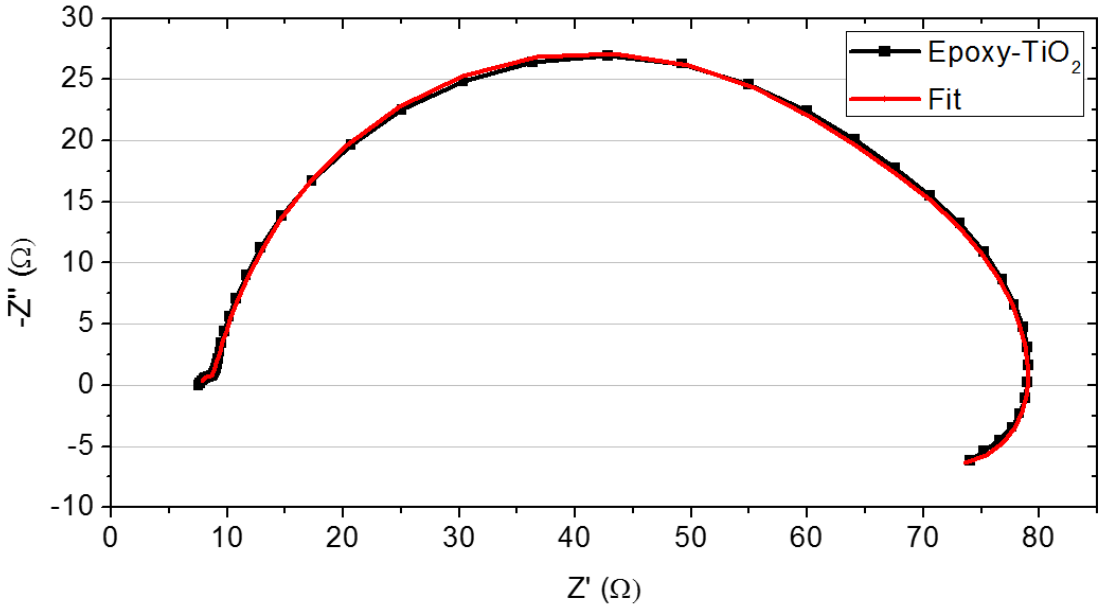

Figure 6.12. Experimental and fitted Nyquist plot for epoxy-TiO_2 DSCs. The equivalent circuit employed was the one presented in Figure 6.4).

The electronic lifetime was obtained from the fit and the results are displayed in Figure 6.13.

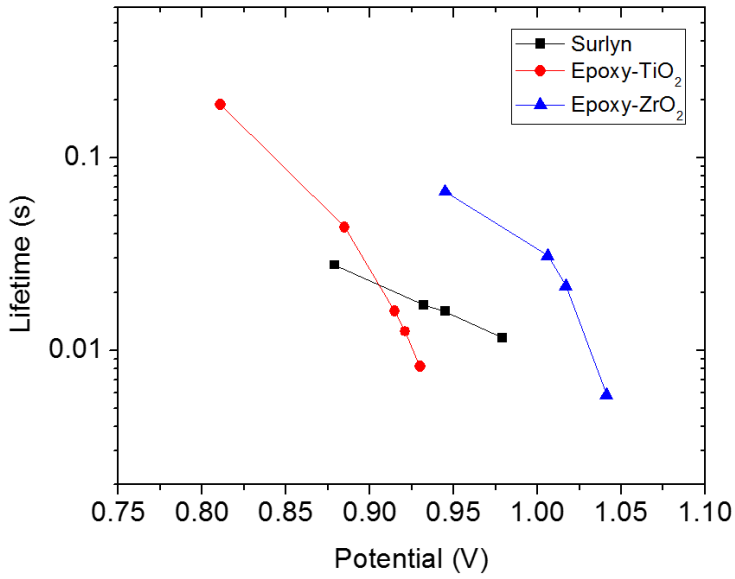

Figure 6.13. Electronic lifetime of the DSCs configurations obtained from EIS measurements.

Since the origin of the differences in the Nyquist plot for the different configurations is not completely clear and the cells gave different open circuit potential values, a direct comparison between DSC configurations is complicated. If we compare the values of the electronic lifetime at the open circuit potential of the epoxy-TiO_2 cells (≈ 925 mV), this configuration presents the lower electronic lifetime. This is in agreement with the lower open circuit potential obtained for this configuration and the extra pathway for recombination. However, the comparison is not reliable since the conditions of the DSCs at this particular potential for the different configurations is not the same.

6.3.Conclusions

DSCs with a copper redox couple presented a high open circuit potential, related with the more positive redox potential of the compound. An important improvement in the fill factor and efficiency of the cells is observed for cells sealed with epoxy resin, related with the reduction of diffusion distance of the redox couple in the DSC and a higher collection efficiency. A study of mass transport shows that diffusion in the bulk may be a limiting factor when working with copper-based redox couples at high illumination intensities, and reducing the distance between electrodes diminishes this inconvenience. Impedance analysis shows an inductive behavior at low frequencies for Epoxy-TiO_2 cells, probably associated with direct interaction between electrons in the TiO_2 mesoporous layer and the polymer counter electrode. This inductive behavior disappears when an insulating ZrO_2 layer is applied over the TiO_2 mesoporous layer.

CHAPTER 7

Fabrication of Solid-state DSCs

Dye-sensitized solar cells offer the opportunity to make efficient solar cells in every color imaginable, and with possibilities for transparency. A clear disadvantage is the liquid electrolyte, which is difficult to encapsulate for long-term stability in solar modules. Therefore, ssDSCs have been developed, where the liquid electrolyte is replaced by a molecular hole transport material or an inorganic p-type semiconductor[34]. In this chapter, a detailed description of the elaboration of ssDSCs is presented, along with SEM and J-V characterization and Nyquist plot analysis from impedance measurements. All the work presented in this chapter was done in the Department of Chemistry, in Uppsala University, Sweden, under the supervision of Professor Gerrit Boschloo and PhD student Jinbao Zhang.

7.1. Experimental procedure

Solid-state DSCs fabrication

Solid-state DSCs were prepared according to a procedure previously reported by Yang *et al*[68]. A (2.5 x 1.5) cm^2 FTO was partially etched by applying Zn powder and an aqueous HCl solution (2 M) to approximately (0.4 x 1.5) cm^2 of exposed area on the FTO for 5 minutes (Figure 7.1). After etching, the FTO was rinsed with ethanol and cleaned according to the procedure described in Chapter 6. After cleaning, the FTO was heated according to the temperature ramp presented in Figure 7.2. One part of the FTO was covered with glass, while the rest of the FTO, including the part that was chemically etched, remain exposed (Figure 7.3 (a)). When the FTO reached 500 °C, a compact TiO_2 blocking layer was deposited onto

the FTO by spray pyrolysis using an airbrush at a distance of 10 cm. The solution used in the spray pyrolysis was 0.2 M titanium isopropoxide, 2 M acetylacetone in isopropanol. 10 spray cycles were applied, one each 30 s (Figure 7.3).

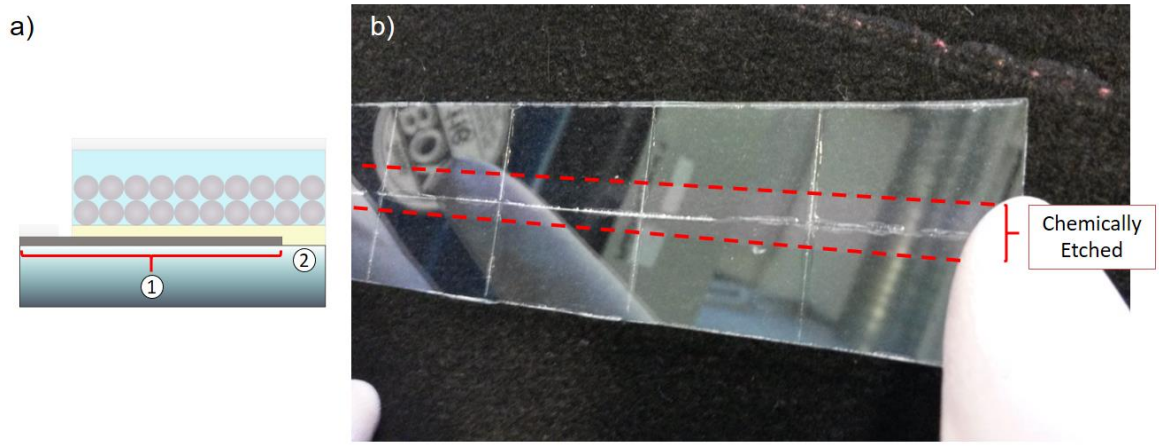

Figure 7.1. (**a**) Diagram of the chemically etched FTO in a ssDSC. Here, (1) represents the FTO and (2) the chemically etched part; the rest of the ssDSC is faded. (**b**) Picture of the chemically etched FTO.

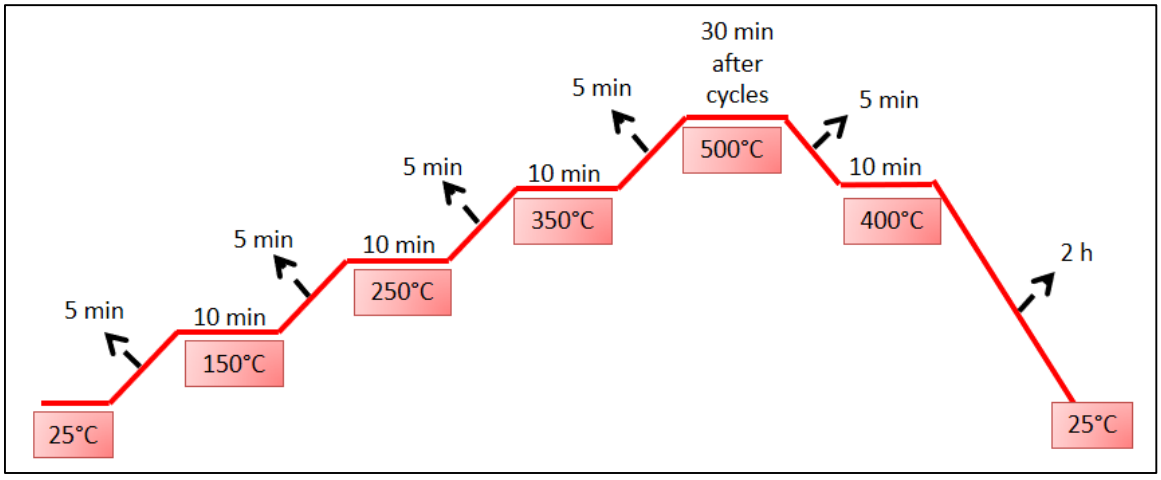

Figure 7.2. Temperature ramp for spray pyrolysis.

Once the cycles were finished, the FTO was kept at 500 °C for 30 min, then it was cooled to 400 °C for 10-15 min and then cooled to room temperature. A mesoporous TiO_2 film was deposited on the compact TiO_2 layer by spincoating (2500 rpm for 30 s) a colloidal TiO_2 paste (Dyesol DSL 18NR-T) diluted in terpineol in 41.7% weight ratio. It has been previously

reported that, under these conditions, an approximately 2 µm thick mesoporous film is obtained[68].

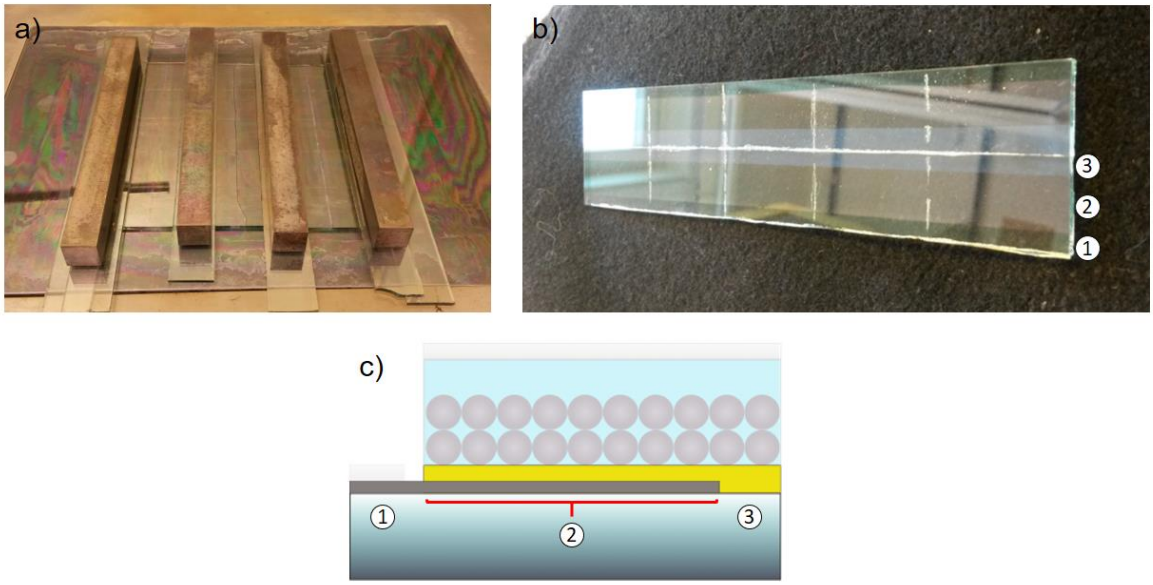

Figure 7.3. (**a**) The FTO is put over a hot plate and is partially covered, (**b**) Picture of the FTO after chemical etching and spray pirolysis and (**c**) representation of the partially etched ssDSC with a blocking layer, while the rest of the ssDSC is faded. In (**b**) and (**c**), (1) represents the FTO without blocking layer, (2) the region of the substrate with FTO and blocking layer and (3) the chemically etched part of the FTO with blocking layer.

The TiO_2 was sintered on a hotplate at 450 °C for 30 min, then cooled to room temperature and immersed in 0.02 M aqueous $TiCl_4$ solution at 70 °C for 30 min. The film was then rinsed with deionized water and annealed on a hotplate at 450 °C for 30 min. After cooling to 90 °C, the film was immersed in a 0.2 mM solution of LEG4 dye in an acetonitrile/*tert*-butanol (1:1 v/v) solution. The sensitized TiO_2 film is presented in Figure 7.4. A solution of 120 mM spiroOMeTAD (Merck) (170 mg/mL), 60 mM 4-tert-butylpyridine and 15 mM LiTFSI in chlorobenzene was applied to the film using a spin coater by leaving the solution to penetrate into it for 30 s before applying 2000 rpm for 30 s. A picture of the ssDSCs with the spiro film is showed in Figure 7.5.

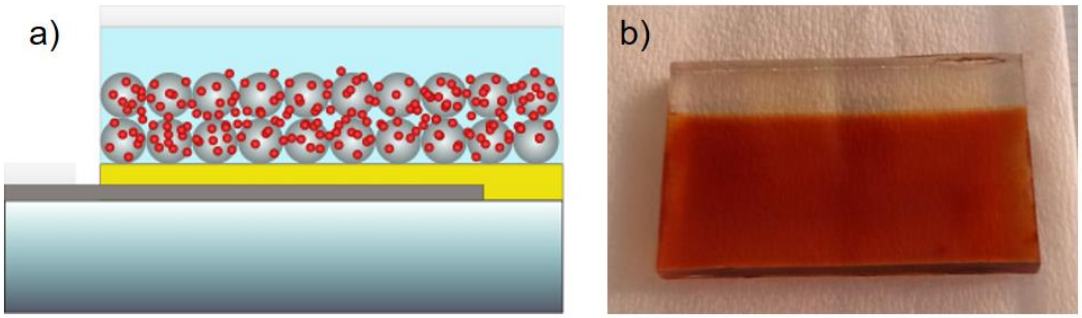

Figure 7.4. (**a**) Representation of the ssDSC after sensitization; the rest of the ssDSC is faded. (**b**) Picture of a ssDSC sensitized with LEG4.

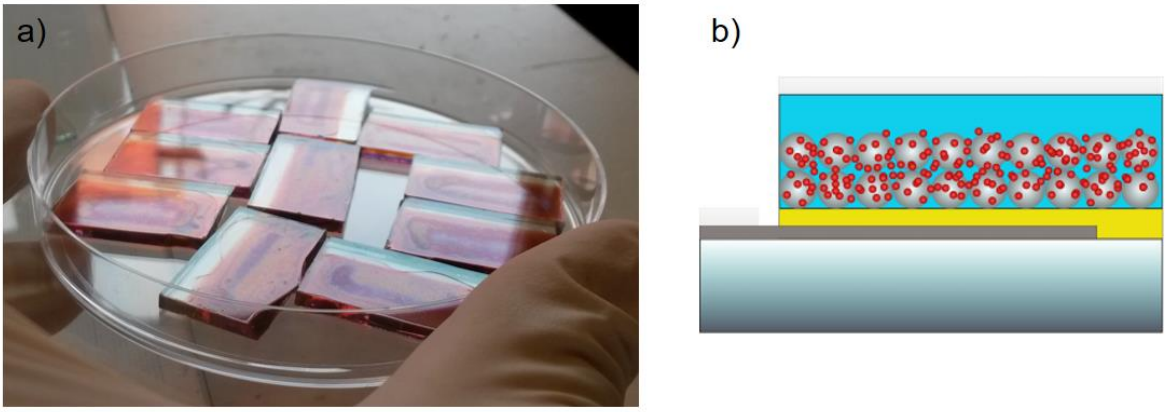

Figure 7.5. (**a**) Picture of the ssDSC with the spiro layer. (b) Representation of a ssDSC with spiroOMeTAD.

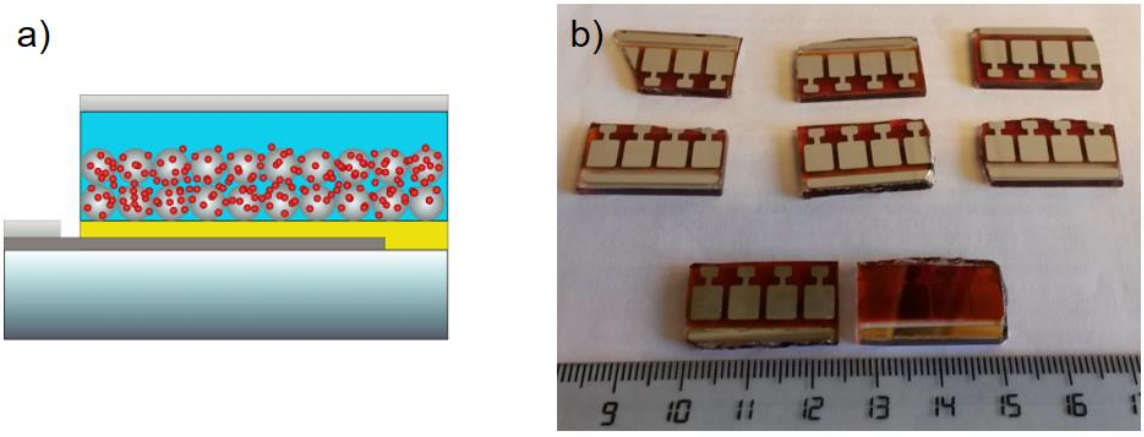

Figure 7.6. (**a**) Representation of the complete ssDSC and (**b**) picture of finished ssDSCs, where both sides of the ssDSC are displayed.

Finally, a 200 nm thick Ag contact was deposited onto the organic semiconductor by thermal evaporation in a vacuum chamber (Leica EM MED020) with a base pressure of about 5-10 mbar, to complete the cell (Figure 7.6).

Characterization

Current-voltage (IV) characteristics of the solar cells were obtained with a Keithley 2400 source/meter and a Newport solar simulator (model 91160). The light intensity was calibrated using a certified reference solar cell (Fraunhofer ISE) to an intensity of 100 mW/cm^2. For the J-V measurements, a black mask of 0.126 cm^2 was employed in order to avoid additional contributions of scattering light in the glass. Electrochemical impedance spectroscopy was performed using a computer controlled electrochemical instrument (AutoLab PGSTAT100) incorporating a frequency response analyzer. EIS measurements were made under dark conditions using an AC amplitude of 10 mV in the 0.1 Hz to 100 kHz frequency range. Cross sections of the solar cell devices were imaged by scanning electron microscopy (Zeiss LEO 1550 high resolution SEM). Samples were scribed on the substrate side and cracked prior to acquisition of SEM-images.

7.2. Results and discussion

An image of the profile of the ssDSC is presented in Figure 7.7. From Figure 7.7, it is observed that the TiO_2 blocking layer has a thickness of around 150 nm. In solid-state DSCs the blocking layer has to be thick enough to prevent high recombination between the hole conductor and the FTO, and the usual reported thickness of the blocking layer for these solar cells commonly oscillates between 100-200 nm[54,68,106]. A homogeneous layer comprised of sensitized mesoporous TiO_2 and the hole conductor indicates that the hole conductor

managed to completely penetrate in the mesoporous layer, which is a necessary condition in order to obtain high efficiency cells[20,54,68,81,106].

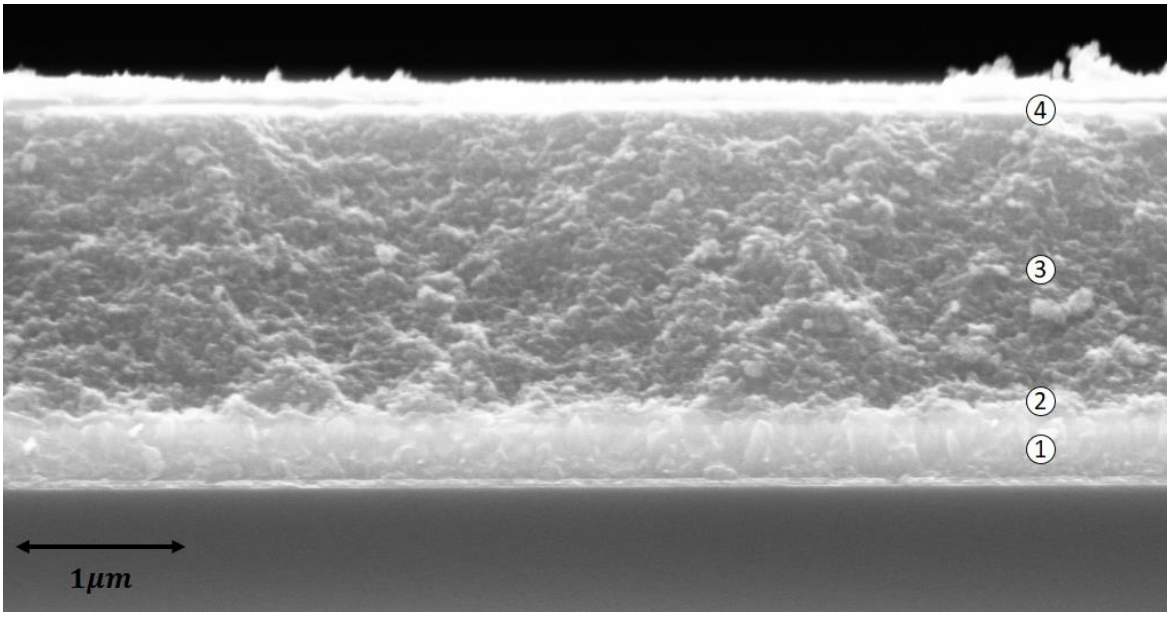

Figure 7.7. SEM profile of the ssDSC. (1) FTO film, (2) TiO_2 blocking layer, (3) Sensitized TiO_2 with spiroOMeTAD interpenetrated and (4) Siver counter electrode. The image was taken at a magnification of 50,000X.

In this work, 26 cells were prepared and measured and in Table 7.1, a summary of the results is presented. In Figure 7.8, a representative curve for the average values of ssDSC, along with the highest and lower performance ssDSC is displayed. The open circuit potential obtained for the ssDSC is above 0.85 V. One of the advantages of using spiroOMeTAD is that it possesses a more positive redox potential (located at a lower Fermi energy) than iodide/triiodide solar cells, which will lead to a higher attainable potential[20,54,79]. Although not properly measured, the thickness of the mesoporous layer and hole conductor is not higher than 3 μm, as can be observed from SEM profile measurements. In spite of this, the current density measured for the ssDSCs is around 10 mA/cm^2. This implies that LEG4 dye is capable of absorbing a large amount of light and, at the same time, generate large currents

in a thin mesoporous layer, which is one of the fundamental requirements in a ssDSC. It also implies that the penetration of the hole conductor into the mesoporous layer is good enough to sustain a high photocurrent.

Table 7.1. J-V parameters of the ssDSC. 26 cells were measured in the calculation of the average values. The standard deviation is also presented.

V_{oc} (V)	J_{sc} (mA/cm^2)	FF	Efficiency (%)
0.869 ± 0.078	10.1 ± 0.6	0.62 ± 0.10	5.4 ± 1.1

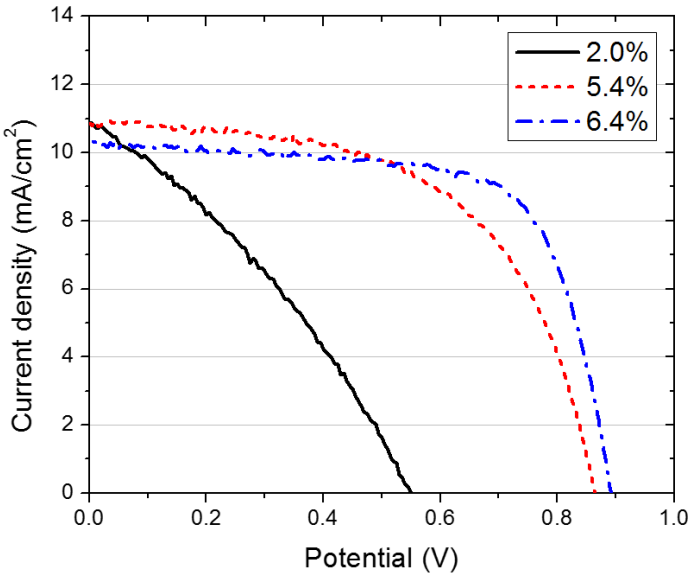

Figure 7.8. Representative J-V curves of the best, worst and average ssDSCs. Efficiency values are displayed.

Overall, the performance of the ssDSCs generated with the method reported by Yang *et al*[68] has proven to be adequate to reproduce high efficiency ssDSCs, since, to my knowledge, the highest efficiency reported for ssDSCs has been from Burschka *et al*[81] which reported an efficiency of 7.2%, while the cells reported in this chapter reached efficiencies as high as 6.4%, as can be observed in Figure 7.8. From this figure, some kind of shunting is observed

for the cells with lower efficiencies, which may be related to direct recombination between electrons in the mesoporous layer and the hole transport material in the ssDSC. It has been reported that recombination for solid-state DSCs is almost 100 times higher than for regular DSCs, which is one of the limitations of high performance ssDSCs so far[54,78,80]. EIS measurements in the dark were performed for the ssDSCs at different potentials, and representative Nyquist plots are presented in Figure 7.9.

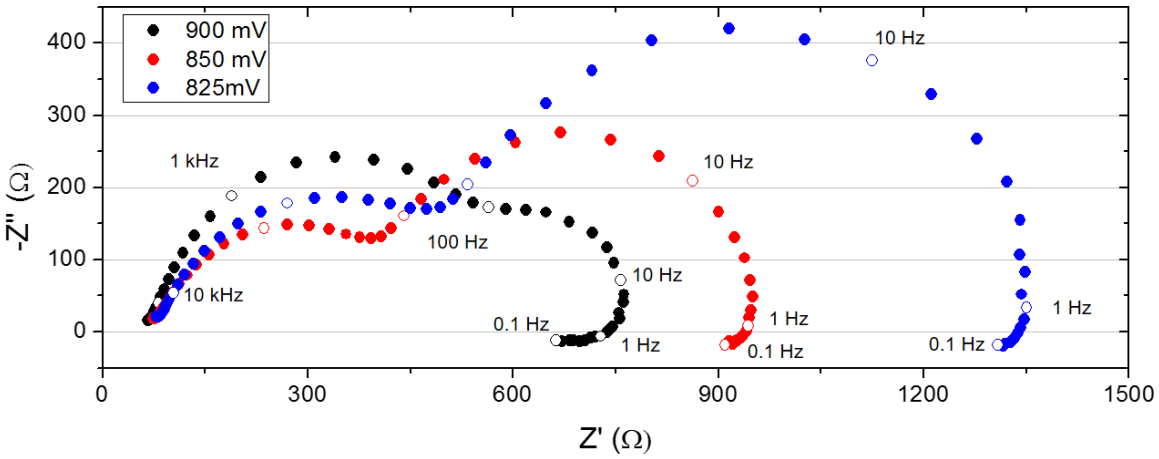

Figure 7.9. Nyquist plots of ssDSC obtained by EIS measurements in the dark at different voltages. Representative frequency points are highlighted.

The analysis of a Nyquist plot for a ssDSC is somewhat similar to that of regular DSCs, although differences arise due to the nature of the hole transport material and the kinetics of transport and recombination. It has been proposed that the semicircle at high frequencies is due to spiroOMeTAD transport resistance together with the effect of interface capacitances at the silver counter electrode and the TiO_2 blocking layer. The low frequency semicircle is associated with charge transfer resistance related with electron recombination at the interface, combined with the chemical capacitance of electrons in the TiO_2[106]. Since the spiroOMeTAD presents a higher transport resistance than the electrolyte solution in a regular DSC, an

additional resistance has to be added to the transmission line proposed by Bisquert[88,101,102] and presented in Figure 3.8. This additional resistance makes the analysis and interpretation of results even more challenging. However, interesting information can be extracted even by just analyzing the Nyquist plot presented in Figure 7.9. It is observed that the first semicircle, associated with transport resistance of the spiro is considerably large, which implies that its contribution to impedance cannot be overlooked. As the potential decreases, the second semicircle becomes bigger, associated with an increase in charge transfer resistance. This trend is the same as for regular DSCs: when the potential is high, the population of electrons in the mesoporous layer is large, increasing recombination events and reducing charge transfer resistance. Another interesting feature can be observed at low frequencies in the Nyquist plot: a negative capacitance appears. This negative capacitance, as previously discussed in Chapter 6, is an indication of some sort of additional recombination pathway, and it has been located at the interface between the mesoporous layer and the hole transport material[106]. Its presence in the Nyquist plot is an indication of ssDSCs with considerably recombination losses.

7.3.Summary

A description of the preparation of ssDSCs was presented. SEM images revealed a good penetration of the hole conductor in the mesoporous layer. J-V characterization of ssDSCs showed high performance devices elaborated according to a pre-established procedure. Differences in EIS with regular DSCs are noticeable and the presence of a negative capacitance at low frequencies was observed.

GENERAL CONCLUSIONS

According to international data, a transition to renewable energies is necessary in order to attenuate the effect of global warming. In this sense, Mexico has a great opportunity to make such a transition, due to its favorable geographical location and natural resources. Solar energy, in particular, is very promising, since all the territory seems to be suitable to exploit this source of energy and it potentially can produce enough energy to fulfill its demand. Dye solar cells are still, after 25 years, a very promising technology and several efforts have been made to improve efficiency and stability. When using alternative redox couples, however, the components of the DSC have to be properly selected since, as reported in chapter 4, an inadequate selection of the dye, for instance, leads to a poor performance of the device. Current-voltage characterizations showed important differences between DSC systems with iodide and cobalt complexes, using a ruthenium-based dye. This dye has proven to be suitable to work with iodide redox couples, but it is clear that in combination with cobalt redox couples it leads to high recombination and low performance in the DSC, as was also corroborated with EIS measurements. The thickness of the mesoporous layer in the DSCs plays an important role in the performance of the DSC and to obtain the optimal DSC configuration, the ideal thickness for each system has to be determined. The effective absorption coefficient has proven to be the factor that determines the ideal thickness of a DSC, as was demonstrated in chapter 5. The exchange current density in the dark does not determine the ideal thickness of the mesoporous layer, but plays an important role on the performance of the DSC, since a reduction on its value leads to an important improvement in the device's efficiency. Differences between the values of the exchange current in the dark

and under illumination describe the differences in recombination between both conditions, as determined with both steady-state and small perturbation techniques. DSCs with copper-based redox couples present mass transport limitations in the bulk solution at high illumination intensities. A reduction in the distance between electrodes helped to improve the device performance by reducing mass transport limitations and increasing the collection efficiency of electrons, which led to an increase in the attainable current and fill factor, and an overall better performance. A negative capacitance at low frequencies appeared for the proposed DSC configuration, associated with interaction of electrons in the mesoporous layer and the PEDOT counter electrode. An equivalent circuit was proposed to represent this interaction, and the fit properly reproduced the experimental data. When applying an extra ZrO_2 layer, the negative capacitance disappeared, proving the origin of this behavior. Solid state DSCs represent an interesting alternative to DSC, with a potentially better stability and high open circuit potential. The procedure presented in this work to fabricate ssDSCs has strong similarities with the process to make DSCs. However, ssDSCs require more specialized and expensive equipment and materials, making them somewhat harder to fabricate. Nevertheless, the efficiencies attained in this work represent competitive performance when compared with all the DSCs presented in previous chapters.

APPENDIX:

CHAPTER 5.

Figure A5.1 shows representative IMVS and IMPS results for the solar cells fabricated in this work. In the IMPS curves, the frequency at the apex of the semi-circles decreases with decreasing voltage; this frequency corresponds to the inverse of the electron lifetime, hence, the lifetime increases with decreasing voltage as expected. In the IMPS curves, the same trend is observed. The time constant associated with IMPS measurements is the transport time, which is inversely proportional to diffusion coefficient. This indicates that the electron diffusion coefficient decreases with decreasing voltage, as has been reported previously[25].

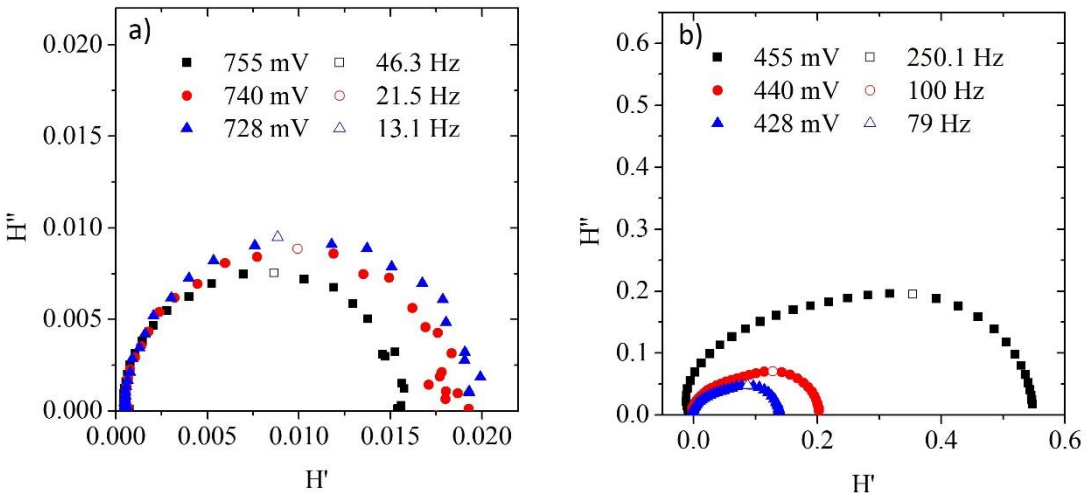

Figure A5.1. (**a**) IMVS and (**b**) IMPS plots for the 21.2 μm solar cell. The values of the frequency at maximum transfer function point are displayed. The voltages presented in the IMVS curves correspond to the open circuit photovoltage, while in the IMPS curves the voltages correspond to the position of the quasi-Fermi level in the TiO_2 film under short-circuit conditions; the voltages were modulated by changing the light intensity.

k_0 and n_0 Determination by IMVS and IMPS Techniques

IMVS measures the modulation of the photovoltage at open circuit in response to the modulation of the incident light intensity. For pseudo first-order kinetics, the decay of the open-circuit photovoltage is determined by a single time constant which corresponds to the lifetime, τ_n, for recombination of electrons with oxidized species, either the oxidized dye or the electron acceptor in the electrolyte[126]. The recombination constant, k, can be obtained as the inverse of the electron lifetime measured by EIS or IMVS[25,125,134]. From a semi logarithmic plot between electron lifetime and the photovoltage (Figure A5.2), the value of τ_0 and, consequently, of k_0 can be obtained. The mean electron concentration (n) within the TiO_2 can be found according to[122,129,130]:

$$n = \frac{J_{SC}\tau_r}{qd(1-\theta)} \qquad \text{(A5.1)}$$

where *Jsc* is the short circuit current density at the measurement conditions and θ is the porosity of the TiO_2 film. For our calculations, a θ value of 0.6 was assumed. Equation (5.8) gives a relationship between the mean electron concentration within the TiO_2 and the photovoltage. Using a semi logarithmic plot between Ln n against V a straight line is obtained and from the intercept with the y-axis the value of n_0 can be determined (Figure A5.2).

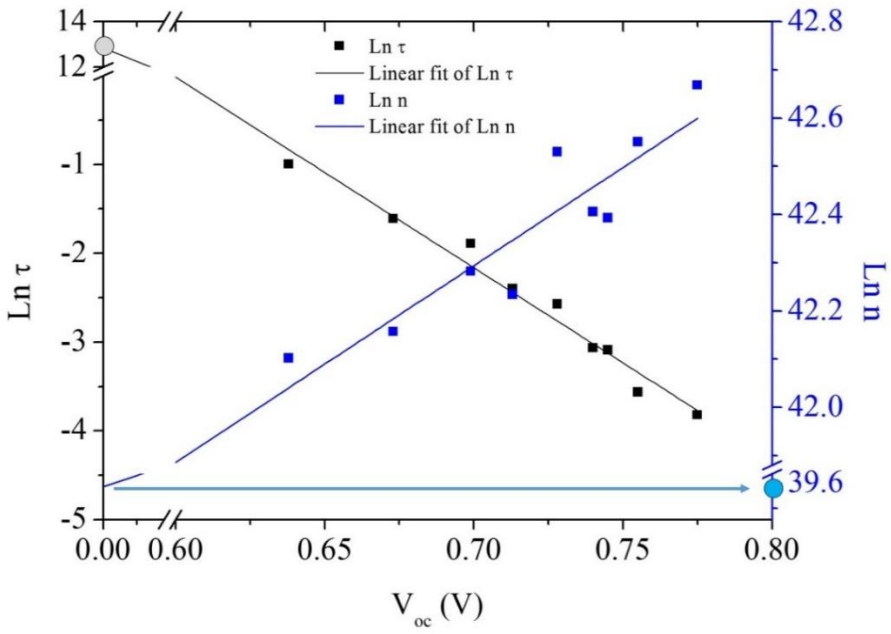

Figure A5.2. Determination of k_0 ($1/\tau_0$, black dots) and n_0 (blue dots) by extrapolation. The intercept at V_{oc} = 0 V is shown by a circle on the respective axis.

In Figure A5.3 SEM images of TiO_2 films of two different thickness are presented.

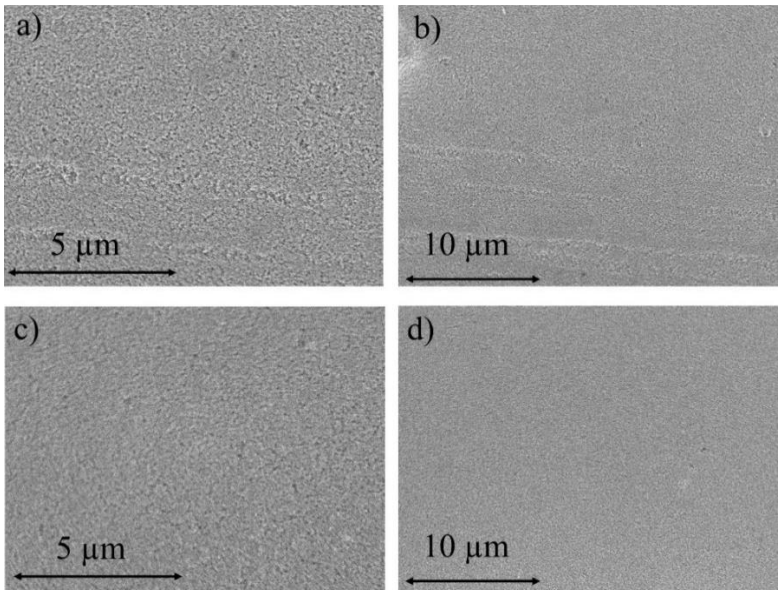

Figure A5.3. SEM images of TiO_2 films of different thicknesses: (**a**) 21.2 µm (magnification: 10,000X); (**b**) 21.2 µm (magnification: 5,000X); (**c**) 32.3 µm (magnification: 10,000X); and (**d**) 32.3 µm (magnification: 5,000X).

Table A5.1. J-V parameters of the dye solar cells as a function of film thickness.

Thickness (μm)	J_{sc} *(mA/cm^2)*	V_{oc} *(V)*	*FF*	*Efficiency (%)*
5.6	7.4	0.801	0.69	4.1
10.2	12.4	0.745	0.61	5.7
11.1	13	0.735	0.62	5.9
14.8	12.7	0.762	0.63	6.3
16.7	14.1	0.741	0.61	6.4
21.2	15	0.748	0.64	7.2
25.7	16	0.731	0.62	7.2
27.6	15.4	0.745	0.60	6.9
32.3	15.2	0.725	0.59	6.5

Table A5.2 Parameters of the DSCs as a function of film thickness.

Label	J_{00} *(A/cm^3)*	α *(cm^{-1})*	*m*	Φ *(cm^{-2}s^{-1})*	*T*	R_s *(Ω)*
A1	7.05×10^{-4}					
A2	7.05×10^{-5}		2			
A3	7.05×10^{-6}					
B1		3731.23	1.5	2.62×10^{17}		
B2			2		0.9	0
B3			2.5			
C1	7.05×10^{-5}	3167.28		2.35×10^{17}		
C2		3731.23	2	2.62×10^{17}		
C3		1029.7		3.14×10^{17}		

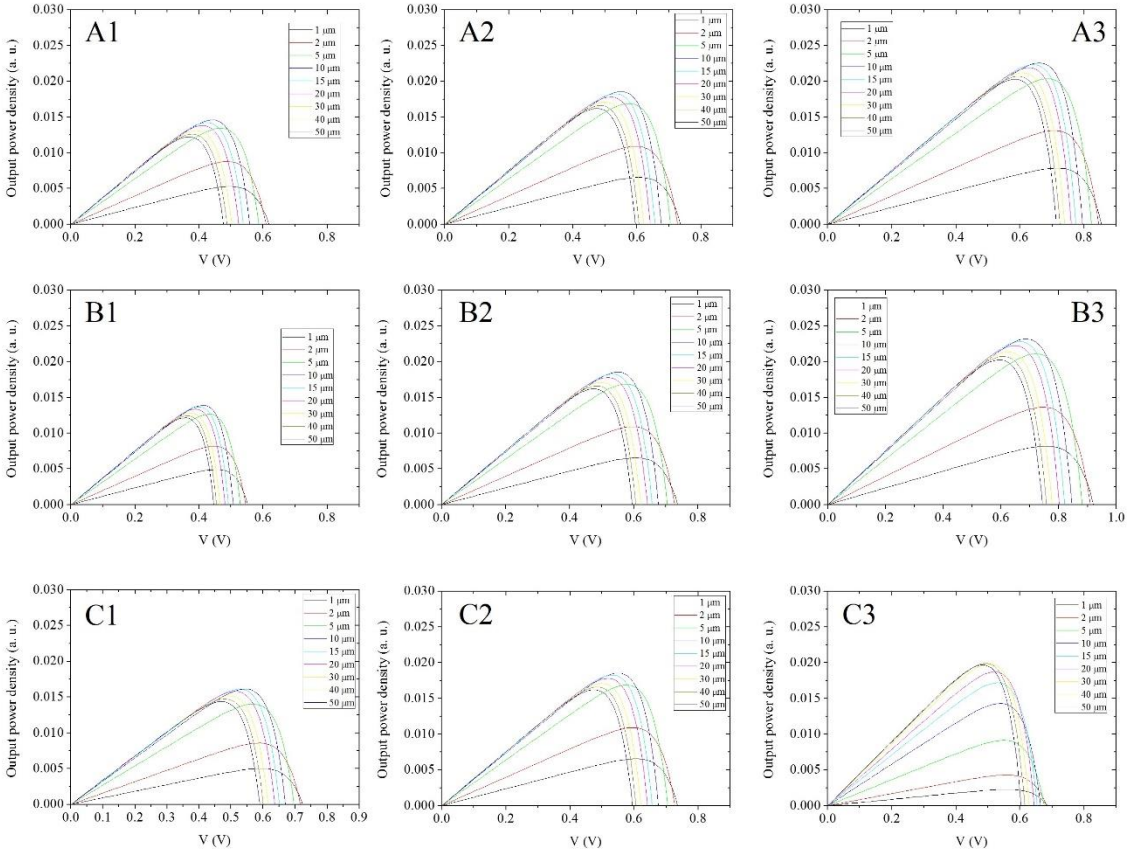

Figure A5.4. Power versus voltages plots for the A, B and C cells.

CHAPTER 6

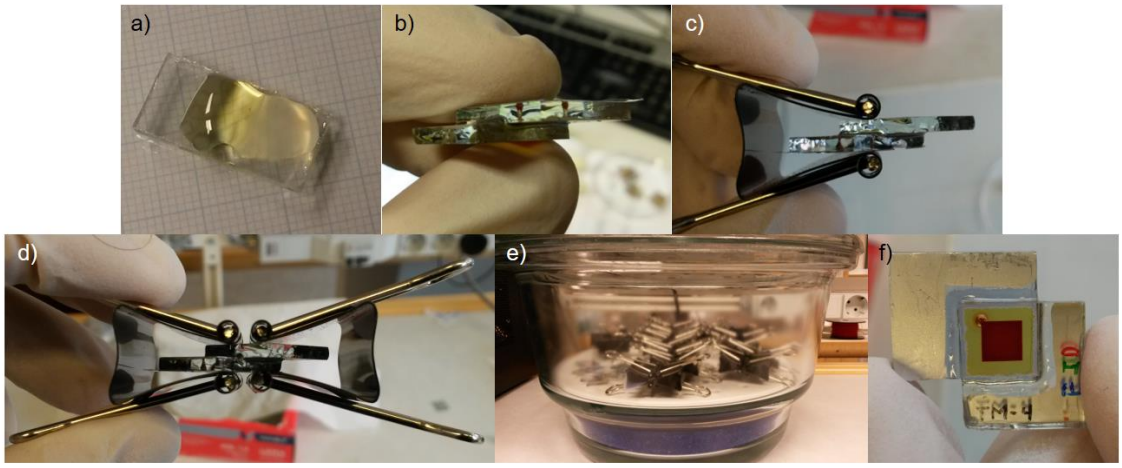

Figure A6.1. (**a**) Mixture 1:1 Solaronix Amosil 4R [Bisphenol-A-(epichlorhydrin) epoxy resin] and 4H (2,2'-iminodiethylamine). (**b**) Electrode and counter electrode pressed against each other. (**c**) Using paper clamps to keep together the electrodes, the epoxy glue is applied on the edges where the two electrodes meet. (**d**) and (**e**) Once the epoxy glue is applied, the cell is kept under the pressure of two paper clamps and they are put inside a desiccator in the dark and the epoxy resin cures overnight. (**f**) The cells are filled with the electrolyte solution and sealed.

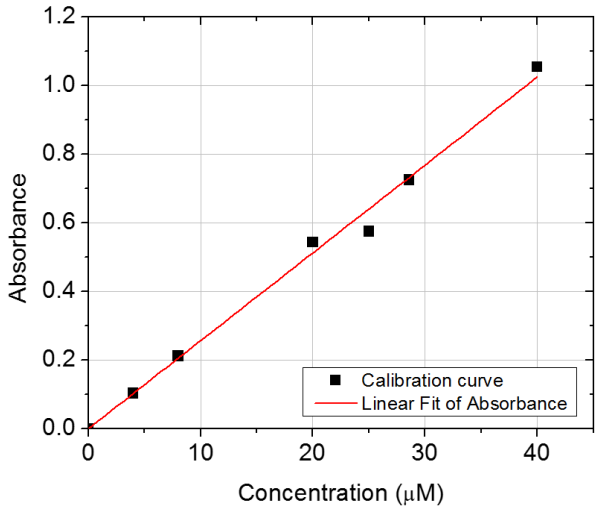

Figure A6.2. Calibration curve in dye desorption measurements. The values of absorbance were obtained at a wavelength of 480.75 nm.

Table A6.1. Concentration of dye adsorbed in the mesoporous electrodes obtained with dye desorption measurements.

Electrode	*Concentration in the film (mol/cm^2)*
5.3 µm TiO_2	(8.3 ± 0.9) x 10^{-8}
5.3 µm TiO_2 + 0.4 µm ZrO_2	(9.4 ± 0.9) x 10^{-8}

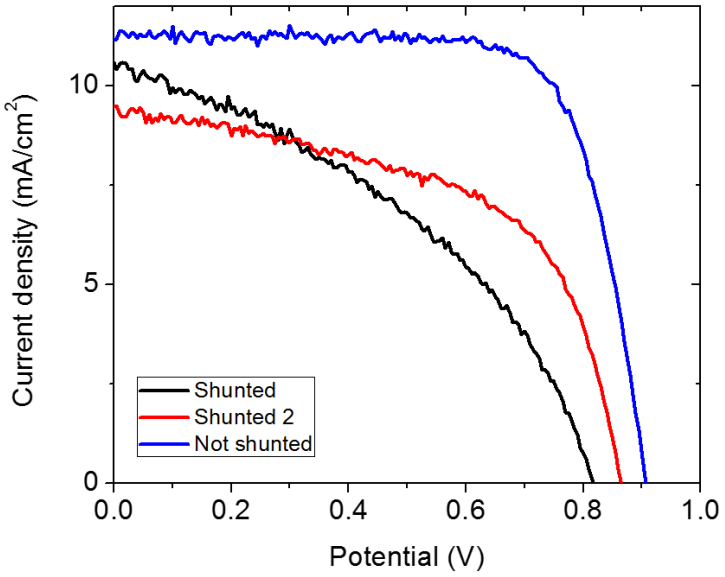

Figure A6.3. Representation of shunted and non-shunted epoxy-TiO_2 cells.

REFERENCES

(1) NASA http://climate.nasa.gov/ (accessed Jul 26, 2016).

(2) Edenhofer, O.; Pichs Madruga, R.; Sokona, Y.; Seyboth, K.; Matschoss, P.; Kadner, S.; Zwickel, T.; Eickemeier, P.; Hansen, G.; Schlomer, S.; Von Stechow, C. *Renewable Energy Sources and Climate Change Mitigation Special Report of the Intergovernmental Panel on Climate Change*; 2012; Vol. 6.

(3) World Wildlife Fund http://www.wwf.org.uk/ (accessed Jul 26, 2016).

(4) European Commission - Climate Action http://ec.europa.eu/clima/ (accessed Jul 26, 2016).

(5) The Nature Conservancy http://www.nature.org/ourinitiatives/urgentissues/global-warming-climate-change/threats-impacts/ (accessed Jul 26, 2016).

(6) Reddy, K. G.; Deepak, T. G.; Anjusree, G. S.; Thomas, S.; Vadukumpully, S.; Subramanian, K. R. V.; Nair, S. V.; Nair, A. S. On Global Energy Scenario, Dye-Sensitized Solar Cells and the Promise of Nanotechnology. *Phys. Chem. Chem. Phys.* **2014**, *16* (15), 6838.

(7) International Energy Agency http://www.iea.org/ (accessed Jul 27, 2016).

(8) Morocco unveils a massive solar power plant in the Sahara http://www.npr.org/sections/thetwo-way/2016/02/04/465568055/morocco-unveils-a-massive-solar-power-plant-in-the-sahara (accessed Jul 30, 2016).

(9) Renewable Energy Policy Network for the 21st Century (REN21) http://www.ren21.net/ (accessed Jul 27, 2016).

(10) International Renewable Energy Agency (IRENA) http://www.irena.org (accessed Jul 27, 2016).

(11) Hagfeldt, A.; Boschloo, G.; Sun, L.; Kloo, L.; Pettersson, H. Dye-Sensitized Solar Cells. *Chem. Rev.* **2010**, *110*, 6595–6663.

(12) Shockley, W.; Queisser, H. J. Detailed Balance Limit of Efficiency of P-N Junction Solar Cells. *J. Appl. Phys.* **1961**, *32* (3), 510–519.

(13) SENER | Sistema de Información Energética http://sie.energia.gob.mx/ (accessed Jul 20, 2016).

(14) U.S. Energy Information Administration (EIA) http://www.eia.gov/ (accessed Jul 20, 2016).

(15) Inventario Nacional de Energías Renovables (INERE) http://inere.energia.gob.mx/version4.5/ (accessed Jul 20, 2016).

(16) Carbon capture and storage - Wikipedia, the free encyclopedia https://en.wikipedia.org/wiki/Carbon_capture_and_storage (accessed Jul 20, 2016).

(17) What are CO2e and global warming potential (GWP)? | Environment | The Guardian https://www.theguardian.com/environment/2011/apr/27/co2e-global-warming-potential (accessed Jul 20, 2016).

(18) Global radiation — PIK Research Portal https://www.pik-potsdam.de/services/climate-weather-potsdam/climate-diagrams/global-radiation (accessed Jul 20, 2016).

(19) Life-cycle greenhouse-gas emissions of energy sources - Wikipedia, the free encyclopedia https://en.wikipedia.org/wiki/Life-cycle_greenhouse-gas_emissions_of_energy_sources (accessed Jul 20, 2016).

(20) Docampo, P.; Guldin, S.; Leijtens, T.; Noel, N. K.; Steiner, U.; Snaith, H. J. Lessons Learned: From Dye-Sensitized Solar Cells to All-Solid-State Hybrid Devices. *Adv. Mater.* **2014**, *26* (24), 4013–4030.

(21) O'Regan, B.; Gratzel, M. A Low-Cost, High-Efficiency Solar Cell Based on Dye-Sensitized Colloidal TiO2 Films. *Nature* **1991**, *353*, 737–740.

(22) Mathew, S.; Yella, A.; Gao, P.; Humphry-Baker, R.; Curchod, B. F. E.; Ashari-Astani, N.; Tavernelli, I.; Rothlisberger, U.; Nazeeruddin, M. K.; Grätzel, M. Dye-Sensitized Solar Cells with 13% Efficiency Achieved through the Molecular Engineering of Porphyrin Sensitizers. *Nat. Chem.* **2014**, *6* (3), 242–247.

(23) García-Rodríguez, R.; Villanueva-Cab, J.; Anta, J. A.; Oskam, G. A Critical Evaluation of the Influence of the Dark Exchange Current on the Performance of Dye-Sensitized Solar Cells. *Materials (Basel).* **2016**, *9* (33), 1–7.

(24) Escalante-Quijano, R.; García-Rodríguez, R.; Heredia-Cervera, B. E.; Aguilar-Frutis, M. A.; Gómez-Ortiz, N.; Villanueva-Cab, J.; Oskam, G. Influence of TiO 2 Film Thickness on the Performance of Dye-Sensitized Solar Cells: Relation Between Optimum Film Thickness and Electron Diffusion Length. *Energy Environ. Focus* **2014**, *2* (4), 1–7.

(25) Anta, J. a.; Idígoras, J.; Guillén, E.; Villanueva-Cab, J.; Mandujano-Ramírez, H. J.; Oskam, G.; Pellejà, L.; Palomares, E. A Continuity Equation for the Simulation of the Current–voltage Curve and the Time-Dependent Properties of Dye-Sensitized Solar Cells. *Phys. Chem. Chem. Phys.* **2012**, *14*

(29), 10285.

(26) Villanueva-Cab, J.; Oskam, G.; Anta, J. A. A Simple Numerical Model for the Charge Transport and Recombination Properties of Dye-Sensitized Solar Cells: A Comparison of Transport-Limited and Transfer-Limited Recombination. *Sol. Energy Mater. Sol. Cells* **2010**, *94* (1), 45–50.

(27) Green, M. A.; Emery, K.; Hishikawa, Y.; Warta, W.; Dunlop, E. D. Solar Cell Efficiency Tables (Version 47). *Prog. Photovolt Res. Appl.* **2016**, *24*, 3–11.

(28) Kakiage, K.; Aoyama, Y.; Yano, T.; Oya, K.; Fujisawa, J.; Hanaya, M. Highly-Efficient Dye-Sensitized Solar Cells with Collaborative Sensitization by Silyl-Anchor and Carboxy-Anchor Dyes. *Chem. Commun.* **2015**, *51* (88), 15894–15897.

(29) Ellis, H.; Eriksson, S. K.; Feldt, S. M.; Gabrielsson, E.; Lohse, P. W.; Lindblad, R.; Sun, L. Linker Unit Modi Fi Cation of Triphenylamine-Based Organic Dyes for. *J. Phys. Chem. C* **2013**, *117*, 21029–21036.

(30) Hao, Y.; Tian, H.; Cong, J.; Yang, W.; Bora, I.; Sun, L.; Boschloo, G.; Hagfeldt, A. Triphenylamine Groups Improve Blocking Behavior of Phenoxazine Dyes in Cobalt-Electrolyte-Based Dye-Sensitized Solar Cells. *ChemPhysChem* **2014**, *15* (16), 3476–3483.

(31) Fan, J.; Hao, Y.; Cabot, A.; Johansson, E. M. J.; Boschloo, G.; Hagfeldt, A. Cobalt(II/III) Redox Electrolyte in ZnO Nanowire-Based Dye-Sensitized Solar Cells. *ACS Appl. Mater. Interfaces* **2013**, *5* (6), 1902–1906.

(32) Feldt, S. M.; Gibson, E. A.; Gabrielsson, E.; Sun, L.; Boschloo, G.; Hagfeldt, A. Design of Organic Dyes and Cobalt Polypyridine Redox Mediators for High-Efficiency Dye-Sensitized Solar Cells. *J. Am. Chem. Soc.* **2010**, *132* (46), 16714–16724.

(33) Yella, a.; Lee, H.-W.; Tsao, H. N.; Yi, C.; Chandiran, a. K.; Nazeeruddin, M. K.; Diau, E. W.-G.; Yeh, C.-Y.; Zakeeruddin, S. M.; Gratzel, M. Porphyrin-Sensitized Solar Cells with Cobalt (II/III)-Based Redox Electrolyte Exceed 12 Percent Efficiency. *Science (80-.).* **2011**, *334* (6056), 629–634.

(34) Freitag, M.; Daniel, Q.; Pazoki, M.; Sveinbjörnsson, K.; Zhang, J.; Sun, L.; Hagfeldt, A.; Boschloo, G. High-Efficiency Dye-Sensitized Solar Cells with Molecular Copper Phenanthroline as Solid Hole Conductor. *Energy Environ. Sci.* **2015**, *8* (9), 2634–2637.

(35) Bai, Y.; Yu, Q.; Cai, N.; Wang, Y.; Zhang, M.; Wang, P. High-Efficiency Organic Dye-Sensitized

Mesoscopic Solar Cells with a Copper Redox Shuttle. *Chem. Commun.* **2011**, *47* (15), 4376.

(36) Cameron, P. J.; Peter, L. M.; Zakeeruddin, S. M.; Grätzel, M. Electrochemical Studies of the Co(III)/Co(II)(dbbip)2 Redox Couple as a Mediator for Dye-Sensitized Nanocrystalline Solar Cells. *Coord. Chem. Rev.* **2004**, *248* (13–14), 1447–1453.

(37) Hardin, B. E.; Snaith, J.; Mcgehee, M. D. The Renaissance of Dye-Sensitized Solar Cells. *Nat. Photonics* **2012**, *6* (February), 162–169.

(38) Hattori, S.; Wada, Y.; Yanagida, S.; Fukuzumi, S. Blue Copper Model Complexes with Distorted Tetragonal Geometry Acting as Effective Electron-Transfer Mediators in Dye-Sensitized Solar Cells. *J. Am. Chem. Soc.* **2005**, *127* (26), 9648–9654.

(39) Nechaev, M. S.; Paraschuk, D. Y. A Quantum-Chemistry Study of Novel Copper- and Cobalt-Complex Based Redox Mediators for Dye-Sensitized Solar Cells. *Moscow Univ. Phys. Bull.* **2013**, *67* (6), 532–535.

(40) Nusbaumer, H.; Moser, J.-E.; Zakeeruddin, S. M.; Nazeeruddin, M. K.; Grätzel, M. Co II (Dbbip) 22 + Complex Rivals Tri-Iodide / Iodide Redox Mediator in Dye-Sensitized Photovoltaic Cells. *J. Phys. Chem. B* **2001**, 10461–10464.

(41) Nusbaumer, H.; Zakeeruddin, S. M.; Moser, J. E.; Grätzel, M. An Alternative Efficient Redox Couple for the Dye-Sensitized Solar Cell System. *Chem. - A Eur. J.* **2003**, *9* (16), 3756–3763.

(42) Tsao, H. N.; Yi, C.; Moehl, T.; Yum, J. H.; Zakeeruddin, S. M.; Nazeeruddin, M. K.; Grätzel, M. Cyclopentadithiophene Bridged Donor-Acceptor Dyes Achieve High Power Conversion Efficiencies in Dye-Sensitized Solar Cells Based on the Tris-Cobalt Bipyridine Redox Couple. *ChemSusChem* **2011**, *4* (5), 591–594.

(43) Yum, J.-H.; Baranoff, E.; Kessler, F.; Moehl, T.; Ahmad, S.; Bessho, T.; Marchioro, A.; Ghadiri, E.; Moser, J.-E.; Yi, C.; Nazeeruddin, M. K.; Grätzel, M. A Cobalt Complex Redox Shuttle for Dye-Sensitized Solar Cells with High Open-Circuit Potentials. *Nat. Commun.* **2012**, *3*, 631–639.

(44) Suhaimi, S.; Shahimin, M. M.; Alahmed, Z. A.; Chysk??, J.; Reshak, A. H. Materials for Enhanced Dye-Sensitized Solar Cell Performance: Electrochemical Application. *Int. J. Electrochem. Sci.* **2015**, *10* (4), 2859–2871.

(45) Qian, D.; Li, Y.; Zhang, Q.; Shi, G.; Wang, H. Anatase TiO2 Sols Derived from Peroxotitanium Acid

and to Form Transparent TiO2 Compact Film for Dye-Sensitized Solar Cells. *J. Alloys Compd.* **2011**, *509* (41), 10121–10126.

(46) Liu, Q. Q.; Zhang, D. W.; Shen, J.; Li, Z. Q.; Shi, J. H.; Chen, Y. W.; Sun, Z.; Yang, Z.; Huang, S. M. Effects of RF and Pulsed DC Sputtered TiO2 Compact Layer on the Performance Dye-Sensitized Solar Cells. *Surf. Coatings Technol.* **2013**, *231*, 126–130.

(47) Kovash, C. S.; Hoefelmeyer, J. D.; Logue, B. A. TiO 2 Compact Layers Prepared by Low Temperature Colloidal Synthesis and Deposition for High Performance Dye-Sensitized Solar Cells. *Electrochim. Acta* **2012**, *67*, 18–23.

(48) Guai, G. H.; Song, Q. L.; Lu, Z. S.; Ng, C. M.; Li, C. M. Tailor and Functionalize TiO2 Compact Layer by Acid Treatment for High Performance Dye-Sensitized Solar Cell and Its Enhancement Mechanism. *Renew. Energy* **2013**, *51*, 29–35.

(49) Sangiorgi, A.; Bendoni, R.; Sangiorgi, N.; Sanson, A.; Ballarin, B. Optimized TiO2 Blocking Layer for Dye-Sensitized Solar Cells. *Ceram. Int.* **2014**, *40* (7 PART B), 10727–10735.

(50) Yu, H.; Zhang, S.; Zhao, H.; Will, G.; Liu, P. An Efficient and Low-Cost TiO2 Compact Layer for Performance Improvement of Dye-Sensitized Solar Cells. *Electrochim. Acta* **2009**, *54* (4), 1319–1324.

(51) Choi, H.; Nahm, C.; Kim, J.; Moon, J.; Nam, S.; Jung, D. R.; Park, B. The Effect of TiCl 4-Treated TiO 2 Compact Layer on the Performance of Dye-Sensitized Solar Cell. *Curr. Appl. Phys.* **2012**, *12* (3), 737–741.

(52) Abdullah, M. H.; Rusop, M. Multifunctional Graded Index TiO2 Compact Layer for Performance Enhancement in Dye Sensitized Solar Cell. *Appl. Surf. Sci.* **2013**, *284*, 278–284.

(53) Lim, S. P.; Huang, N. M.; Lim, H. N.; Mazhar, M. Aerosol Assisted Chemical Vapour Deposited (AACVD) of TiO2 Thin Film as Compact Layer for Dye-Sensitised Solar Cell. *Ceram. Int.* **2014**, *40* (6), 8045–8052.

(54) Fabregat-Santiago, F.; Bisquert, J.; Cevey, L.; Chen, P.; Wang, M.; Zakeeruddin, S. M.; Gr??tzel, M. Electron Transport and Recombination in Solid-State Dye Solar Cell with Spiro-OMeTAD as Hole Conductor. *J. Am. Chem. Soc.* **2009**, *131* (2), 558–562.

(55) Zhang, J.; Häggman, L.; Jouini, M.; Jarboui, A.; Boschloo, G.; Vlachopoulos, N.; Hagfeldt, A. Solid-

State Dye-Sensitized Solar Cells Based on poly(3,4-Ethylenedioxypyrrole) and Metal-Free Organic Dyes. *ChemPhysChem* **2014**, *746*, 1043–1047.

(56) Zaban, A.; Meier, A.; Gregg, B. . Electric Potential Distribution and Short Range Screening in Nanoporous TiO2 Electrodes. *J. Phys. Chem. B* **1997**, *101* (97), 7985–7990.

(57) Lizama-Tzec, F. I.; García-Rodríguez, R.; Rodríguez-Gattorno, G.; Canto-Aguilar, E. J.; Vega-Poot, A. G.; Heredia-Cervera, B. E.; Villanueva-Cab, J.; Morales-Flores, N.; Pal, U.; Oskam, G. Influence of Morphology on the Performance of ZnO-Based Dye-Sensitized Solar Cells. *RSC Adv.* **2016**, *6* (44), 37424–37433.

(58) Gómez-Ortíz, N. M.; Idígoras, J.; Guillén, E.; Hernández, A.; Sastre-Santos, A.; Fernández-Lázaro, F.; Anta, J. A.; Oskam, G. Influence of Dye Chemistry and Electrolyte Solution on Interfacial Processes at Nanostructured Zno in Dye-Sensitized Solar Cells. *J. Photochem. Photobiol. A Chem.* **2013**, *264*, 26–33.

(59) Guillén, E.; Peter, L. M.; Anta, J. A. Electron Transport and Recombination in ZnO-Based Dye-Sensitized Solar Cells. *J. Phys. Chem. C* **2011**, *115* (45), 22622–22632.

(60) Guillén, E.; Fernández-Lorenzo, C.; Alcántara, R.; Martín-Calleja, J.; Anta, J. A. Solvent-Free ZnO Dye-Sensitised Solar Cells. *Sol. Energy Mater. Sol. Cells* **2009**, *93* (10), 1846–1852.

(61) Kay, A.; Grätzel, M. Dye-Sensitized Core-Shell Nanocrystals: Improved Efficiency of Mesoporous Tin Oxide Electrodes Coated with a Thin Layer of an Insulating Oxide. *Chem. Mater.* **2002**, *14* (7), 2930–2935.

(62) Lenzmann, F.; Krueger, JessicaSurface Photovoltage Spectroscopy of Dye-Sensitized Solar Cells with TiO 2 , Nb 2 O 5, and S. 3 N. P. I. for E. I. from H. E. D. S.; Burnside, S.; Brooks, K.; Grätzel, M.; Gal, D.; Rühle, S.; Cahen, D.; Krueger, J.; Krueger, JessicaSurface Photovoltage Spectroscopy of Dye-Sensitized Solar Cells with TiO 2 , Nb 2 O 5, and S. 3 N. P. I. for E. I. from H. E. D. S.; Burnside, S.; Brooks, K.; Grätzel, M.; Gal, D.; Rühle, S.; Cahen, D. Surface Photovoltage Spectroscopy of Dye-Sensitized Solar Cells with TiO2,Nb2O5, and SrTiO3 Nanocrystalline Photoanodes: Indication for Electron Injection from Higher Excited Dye States. *J. Phys. Chem. B* **2001**, *105*, 6347–6352.

(63) Moser, J.-E.; Wolf, M.; Lenzmann, F.; Grätzel, M. Photoinduced Charge Injection from Vibronically

Hot Excited Molecules of a Dye Sensitizer into Acceptor States of Wide-Bandgap Oxide Semiconductors. *Zeitschrift fur Phys. Chemie* **1999**, *212* (1), 85–92.

(64) Oskam, G. Dye-Sensitized, Nanostructured Metal Oxide Photoelectrodes for Solar Energy Conversion. *Curr. Top. Electrochem.* **2004**, *10*, 141–162.

(65) Zhang, Q.; Myers, D.; Lan, J.; Jenekhe, S. a; Cao, G. Applications of Light Scattering in Dye-Sensitized Solar Cells. *Phys. Chem. Chem. Phys.* **2012**, *14* (43), 14982–14998.

(66) Ito, S.; Murakami, T. N.; Comte, P.; Liska, P.; Grätzel, C.; Nazeeruddin, M. K.; Grätzel, M. Fabrication of Thin Film Dye Sensitized Solar Cells with Solar to Electric Power Conversion Efficiency over 10%. *Thin Solid Films* **2008**, *516* (14), 4613–4619.

(67) Kalyanasundaram, K. *Dye-Sensitized Solar Cells*; Press, E., Ed.; 2010.

(68) Yang, L.; Cappel, U. B.; Unger, E. L.; Karlsson, M.; Karlsson, K. M.; Gabrielsson, E.; Sun, L.; Boschloo, G.; Hagfeldt, A.; Johansson, E. M. J. Comparing Spiro-OMeTAD and P3HT Hole Conductors in Efficient Solid State Dye-Sensitized Solar Cells. *Phys. Chem. Chem. Phys.* **2012**, *14* (2), 779.

(69) Chiba, Y.; Islam, A.; Watanabe, Y.; Komiya, R.; Koide, N.; Han, L. Dye-Sensitized Solar Cells with Conversion Efficiency of 11.1%. *Japanese J. Appl. Physics, Part 2 Lett.* **2006**, *45* (24–28), 9–12.

(70) Kambe, S.; Nakade, S.; Wada, Y.; Kitamura, T.; Yanagida, S. Effects of Crystal Structure, Size, Shape and Surface Structural Differences on Photo-Induced Electron Transport in TiO2 Mesoporous Electrodes. *J. Mater. Chem.* **2002**, *12* (3), 723–728.

(71) Nakade, S.; Makimoto, Y.; Kubo, W.; Kitamura, T.; Wada, Y.; Yanagida, S. Roles of Electrolytes on Charge Recombination in Dye-Sensitized TiO 2 Solar Cells (2): The Case of Solar Cells Using Cobalt Complex Redox Couples. *J. Phys. Chem. B* **2005**, *109* (8), 3488–3493.

(72) Fischer, A.; Pettersson, H.; Hagfeldt, A.; Boschloo, G.; Kloo, L.; Gorlov, M. Crystal Formation Involving 1-Methylbenzimidazole in Iodide/triiodide Electrolytes for Dye-Sensitized Solar Cells. *Sol. Energy Mater. Sol. Cells* **2007**, *91* (12), 1062–1065.

(73) Ellis, H.; Vlachopoulos, N.; Häggman, L.; Perruchot, C.; Jouini, M.; Boschloo, G.; Hagfeldt, A. PEDOT Counter Electrodes for Dye-Sensitized Solar Cells Prepared by Aqueous Micellar Electrodeposition. *Electrochim. Acta* **2013**, *107*, 45–51.

(74) Pringle, J. M.; Armel, V.; MacFarlane, D. R. Electrodeposited PEDOT-on-Plastic Cathodes for Dye-Sensitized Solar Cells. *Chem. Commun.* **2010**, *46* (29), 5367.

(75) Guldin, S.; Docampo, P.; Stefik, M.; Kamita, G.; Wiesner, U.; Snaith, H. J.; Steiner, U. Layer-by-Layer Formation of Block-Copolymer-Derived TiO 2 for Solid-State Dye-Sensitized Solar Cells. *Small* **2012**, *8* (3), 432–440.

(76) Zhang, W.; Cheng, Y.; Yin, X.; Liu, B. Solid-State Dye-Sensitized Solar Cells with Conjugated Polymers as Hole-Transporting Materials. *Macromol. Chem. Phys.* **2011**, *212* (1), 15–23.

(77) Nogueira, A. F.; Longo, C.; De Paoli, M. A. Polymers in Dye Sensitized Solar Cells: Overview and Perspectives. *Coord. Chem. Rev.* **2004**, *248* (13–14), 1455–1468.

(78) Li, B.; Wang, L.; Kang, B.; Wang, P.; Qiu, Y. Review of Recent Progress in Solid-State Dye-Sensitized Solar Cells. *Sol. Energy Mater. Sol. Cells* **2006**, *90* (5), 549–573.

(79) Docampo, P.; Guldin, S.; Steiner, U.; Snaith, H. J. Charge Transport Limitations in Self-Assembled TiO2 Photoanodes for Dye-Sensitized Solar Cells. *J. Phys. Chem. Lett.* **2013**, *4* (5), 698–703.

(80) Fabregat-Santiago, F.; Bisquert, J.; Palomares, E.; Haque, S. A.; Durrant, J. R. Impedance Spectroscopy Study of Dye-Sensitized Solar Cells with Undoped Spiro-OMeTAD as Hole Conductor. *J. Appl. Phys.* **2006**, *100* (3).

(81) Burschka, J.; Dualeh, A.; Kessler, F.; Baranoff, E.; Cevey-Ha, N.-L.; Yi, C.; Nazeeruddin, M. K.; Grätzel, M. Tris(2-(1H-Pyrazol-1-yl)pyridine)cobalt(III) as P-Type Dopant for Organic Semiconductors and Its Application in Highly Efficient Solid-State Dye-Sensitized Solar Cells. *J. Am. Chem. Soc.* **2011**, *133* (45), 18042–18045.

(82) Hsu, C.-Y.; Chen, Y.-C.; Lin, R. Y.-Y.; Ho, K.-C.; Lin, J. T. Solid-State Dye-Sensitized Solar Cells Based on Spirofluorene (Spiro-OMeTAD) and Arylamines as Hole Transporting Materials. *Phys. Chem. Chem. Phys.* **2012**, *14* (41), 14099–14109.

(83) Bach, U.; Lupo, D.; Comte, P.; Moser, J. E.; Weissörtel, F.; Salbeck, J.; Spreitzer, H.; Grätzel, M. Solid-State Dye-Sensitized Mesoporous TiO2 Solar Cells with High Photon-to-Electron Conversion Efficiencies. *Nature* **1998**, *395* (6702), 583–585.

(84) Yanagida, S.; Yu, Y.; Manseki, K. Iodine/iodide-Free Dye-Sensitized Solar Cells. *Acc. Chem. Res.* **2009**, *42* (11), 1827–1838.

(85) Sakmeche, N.; Aaron, J. J.; Fall, M.; Aeiyach, S.; Jouini, M.; Lacroix, J. C.; Lacaze, P. C. Anionic Micelles; a New Aqueous Medium for Electropolymerization of poly(3,4-Ethylenedioxythiophene) Films on Pt Electrodes. *Chem. Commun.* **1996**, 2723.

(86) Sakmeche, N.; Aeiyach, S.; Aaron, J.; Jouini, M.; Lacroix, J. C.; Lacaze, P. Improvement of the Electrosynthesis and Physicochemical Properties of Poly (3 , 4-Ethylenedioxythiophene) Using a Sodium Dodecyl Sulfate Micellar Aqueous Medium. **1999**, *1* (28), 2566–2574.

(87) Solar Spectra NREL http://rredc.nrel.gov/solar/spectra/ (accessed Jul 20, 2016).

(88) Fabregat-Santiago, F.; Garcia-Belmonte, G.; Mora-Sero, I.; Bisquert, J. Characterization of Nanostructured Hybrid and Organic Solar Cells by Impedance Spectroscopy. *Phys. Chem. Chem. Phys.* **2011**, *13* (20), 9083–9118.

(89) Halme, J.; Vahermaa, P.; Miettunen, K.; Lund, P. Device Physics of Dye Solar Cells. *Adv. Mater.* **2010**, *22* (35).

(90) Bard, A. J.; Faulkner, L. R. *Electrochemical Methods. Fundamentals and Applications.*, Second Edi.; John Wiley & Sons, Inc., 2001.

(91) Fabregat-Santiago, F.; Bisquert, J.; Palomares, E.; Otero, L.; Kuang, D.; Zakeeruddin, S. M.; Grätzel, M. Correlation between Photovoltaic Performance and Impedance Spectroscopy of Dye-Sensitized Solar Cells Based on Ionic Liquids. *J. Phys. Chem.* **2007**, *2*, 6550–6560.

(92) Vicent-Luna, J. M.; Idígoras, J.; Hamad, S.; Calero, S.; Anta, J. A. Ion Transport in Electrolytes for Dye-Sensitized Solar Cells: A Combined Experimental and Theoretical Study. *J. Phys. Chem. C* **2014**, *118* (49), 28448–28455.

(93) Nelson, J. J.; Amick, T. J.; Elliott, C. M. Mass Transport of Polypyridyl Cobalt Complexes in Dye-Sensitized Solar Cells with Mesoporous TiO 2 Photoanodes. *J. Phys. Chem. C* **2008**, *112*, 18255–18263.

(94) Kim, H.-S.; Ko, S.-B.; Jang, I.-H.; Park, N.-G. Improvement of Mass Transport of the [Co(bpy)3](II/III) Redox Couple by Controlling Nanostructure of TiO2 Films in Dye-Sensitized Solar Cells. *Chem. Commun. (Camb).* **2011**, *47* (47), 12637–12639.

(95) Klahr, B. M.; Hamann, T. W. Performance Enhancement and Limitations of Cobalt Bipyridyl Redox Shuttles in Dye-Sensitized Solar Cells. *J. Phys. Chem. C* **2009**, *113* (31), 14040–14045.

(96) Bailes, M.; Cameron, P. J.; Lobato, K.; Peter, L. M. Determination of the Density and Energetic Distribution of Electron Traps in Dye-Sensitized Nanocrystalline Solar Cells. *J. Phys. Chem. B* **2005**, *109* (32), 15429–15435.

(97) Zaban, A.; Greenshtein, M.; Bisquert, J. Determination of the Electron Lifetime in Nanocrystalline Dye Solar Cells by Open-Circuit Voltage Decay Measurements. *ChemPhysChem* **2003**, *4* (8), 859–864.

(98) Bisquert, J.; Zaban, A.; Greenshtein, M.; Mora-Serot, I. Determination of Rate Constants for Charge Transfer and the Distribution of Semiconductor and Electrolyte Electronic Energy Levels in Dye-Sensitized Solar Cells by Open-Circuit... *J. Am. Chem. Soc.* **2004**, *126* (41), 13550–13559.

(99) Duffy, N. W.; Peter, L. M.; Rajapakse, R. M. G.; Wijayantha, K. G. U. A Novel Charge Extraction Method for the Study of Electron Transport and Interfacial Transfer in Dye Sensitised Nanocrystalline Solar Cells. *Electrochem. commun.* **2000**, *2* (9), 658–662.

(100) Basics of EIS: Electrochemical Research-Impedance http://www.gamry.com/application-notes/EIS/basics-of-electrochemical-impedance-spectroscopy/ (accessed Jul 20, 2016).

(101) Fabregat-Santiago, F.; Bisquert, J.; Garcia-Belmonte, G.; Boschloo, G.; Hagfeldt, A. Influence of Electrolyte in Transport and Recombination in Dye-Sensitized Solar Cells Studied by Impedance Spectroscopy. *Sol. Energy Mater. Sol. Cells* **2005**, *87* (1–4), 117–131.

(102) Bisquert, J.; Garcia-Belmonte, G.; Fabregat-Santiago, F.; Ferriols, N. S.; Bogdanoff, P.; Pereira, E. C. Doubling Exponent Models for the Analysis of Porous Film Electrodes by Impedance. Relaxation of TiO 2 Nanoporous in Aqueous Solution. *J. Phys. Chem. B* **2000**, *104* (10), 2287–2298.

(103) Mora-Seró, I.; Bisquert, J.; Fabregat-Santiago, F.; Garcia-Belmonte, G.; Zoppi, G.; Durose, K.; Proskuryakov, Y.; Oja, I.; Belaidi, A.; Dittrich, T.; Tena-Zaera, R.; Katty, A.; Lévy-Clément, C.; Barrioz, V.; Irvine, S. J. C. Implications of the Negative Capacitance Observed at Forward Bias in Nanocomposite and Polycrystalline Solar Cells. **2006**.

(104) Wu, X.; Yang, E. S.; Evans, H. L. Negative Capacitance at Metal-Semiconductor Interfaces. *J. Appl. Phys.* **1990**, *68* (6), 2845–2848.

(105) Bisquert, J. Theory of the Impedance of Charge Transfer via Surface States in Dye-Sensitized Solar Cells. *J. Electroanal. Chem.* **2010**, *646* (1–2), 43–51.

(106) Li, T. C.; Góes, M. S.; Fabregat-Santiago, F.; Bisquert, J.; Bueno, P. R.; Prasittichai, C.; Hupp, J. T.; Marks, T. J. Surface Passivation of Nanoporous TiO 2 via Atomic Layer Deposition of ZrO 2 for Solid-State Dye-Sensitized Solar Cell Applications. *J. Phys. Chem. C* **2009**, *113* (42), 18385–18390.

(107) Kron, G.; Egerter, T.; Werner, J. H.; Rau, U. Electronic Transport in Dye-Sensitized Nanoporous TiO2 Solar Cells - Comparison of Electrolyte and Solid-State Devices. *J. Phys. Chem. B* **2003**, *107* (15), 3556–3564.

(108) Bisquert, J. A Variable Series Resistance Mechanism to Explain the Negative Capacitance Observed in Impedance Spectroscopy Measurements of Nanostructured Solar Cells. *Phys. Chem. Chem. Phys.* **2011**, *13* (10), 4679–4685.

(109) Dye Solar Cells - IMPS/IMVS Measurements http://www.gamry.com/application-notes/physechem/dye-solar-cells-imps-imvs/ (accessed Jul 20, 2016).

(110) Guillén Rodriguez, E. Photoelectrochemical Characterization of Dye Solar Cells Based on Nanostructured Zinc Oxide Substrates, Pablo de Olavide, 2011.

(111) Mosconi, E.; Yum, J.-H. H.; Kessler, F.; Gomez Garcia, C. J.; Zuccaccia, C.; Cinti, A.; Nazeeruddin, M. K.; Graetzel, M.; De Angelis, F.; Garcia, C. J. G.; Zuccaccia, C.; Cinti, A.; Nazeeruddin, M. K.; Gratzel, M.; De Angelis, F.; Gomez Garcia, C. J.; Zuccaccia, C.; Cinti, A.; Nazeeruddin, M. K.; Graetzel, M.; De Angelis, F. Cobalt Electrolyte/Dye Interactions in Dye-Sensitized Solar Cells: A Combined Computational and Experimental Study. *J. Am. Chem. Soc.* **2012**, *134* (47), 19438–19453.

(112) Liu, Y.; Jennings, J. R.; Huang, Y.; Wang, Q.; Zakeeruddin, S. M.; Gr??tze, M. Cobalt Redox Mediators for Ruthenium-Based Dye-Sensitized Solar Cells: A Combined Impedance Spectroscopy and near-IR Transmittance Study. *J. Phys. Chem. C* **2011**, *115* (38), 18847–18855.

(113) Hsu, C. P.; Lee, K. M.; Huang, J. T. W.; Lin, C. Y.; Lee, C. H.; Wang, L. P.; Tsai, S. Y.; Ho, K. C. EIS Analysis on Low Temperature Fabrication of TiO2 Porous Films for Dye-Sensitized Solar Cells. *Electrochim. Acta* **2008**, *53* (25), 7514–7522.

(114) Huang, C. Y.; Hsu, Y. C.; Chen, J. G.; Suryanarayanan, V.; Lee, K. M.; Ho, K. C. The Effects of Hydrothermal Temperature and Thickness of TiO2 Film on the Performance of a Dye-Sensitized Solar Cell. *Sol. Energy Mater. Sol. Cells* **2006**, *90* (15), 2391–2397.

(115) Zhang, H.; Wang, W.; Liu, H.; Wang, R.; Chen, Y.; Wang, Z. Effects of TiO2 Film Thickness on

Photovoltaic Properties of Dye-Sensitized Solar Cell and Its Enhanced Performance by Graphene Combination. *Mater. Res. Bull.* **2014**, *49* (1), 126–131.

(116) Kao, M. C.; Chen, H. Z.; Young, S. L.; Kung, C. Y.; Lin, C. C. The Effects of the Thickness of TiO2 Films on the Performance of Dye-Sensitized Solar Cells. *Thin Solid Films* **2009**, *517* (17), 5096–5099.

(117) Shin, I.; Seo, H.; Son, M.-K.; Kim, J.-K.; Prabakar, K.; Kim, H.-J. Analysis of TiO2 Thickness Effect on Characteristic of a Dye-Sensitized Solar Cell by Using Electrochemical Impedance Spectroscopy. *Curr. Appl. Phys.* **2010**, *10* (3), S422–S424.

(118) Park, K. H.; Kim, T. Y.; Kim, J. H.; Kim, H. J.; Hong, C. K.; Lee, J. W. Adsorption and Electrochemical Properties of Photoelectrodes Depending on TiO2 Film Thickness for Dye-Sensitized Solar Cells. *J. Electroanal. Chem.* **2013**, *708*, 39–45.

(119) Wang, Z. S.; Kawauchi, H.; Kashima, T.; Arakawa, H. Significant Influence of TiO2 Photoelectrode Morphology on the Energy Conversion Efficiency of N719 Dye-Sensitized Solar Cell. *Coord. Chem. Rev.* **2004**, *248* (13–14), 1381–1389.

(120) Zhu, K.; Jang, S. R.; Frank, A. J. Impact of High Charge-Collection Efficiencies and Dark Energy-Loss Processes on Transport, Recombination, and Photovoltaic Properties of Dye-Sensitized Solar Cells. *J. Phys. Chem. Lett.* **2011**, *2* (9), 1070–1076.

(121) Ito, S.; Liska, P.; Comte, P.; Charvet, R.; Péchy, P.; Bach, U.; Schmidt-Mende, L.; Zakeeruddin, S. M.; Kay, A.; Nazeeruddin, M. K.; Grätzel, M. Control of Dark Current in Photoelectrochemical (TiO2/I--I3-)) and Dye-Sensitized Solar Cells. *Chem. Commun. (Camb).* **2005**, No. 34, 4351–4353.

(122) Shi, Y.; Dong, X. Coupled Analysis of Steady-State and Dynamic Characteristics of Dye-Sensitized Solar Cells for Determination of Conduction Band Movement and Recombination Parameters. *Phys. Chem. Chem. Phys.* **2012**, 299–306.

(123) Gonzalez-Vazquez, J. P.; Oskam, G.; Anta, J. A. Origin of Nonlinear Recombination in Dye-Sensitized Solar Cells: Interplay between Charge Transport and Charge Transfer. *J. Phys. Chem. C* **2012**, *116* (43), 22687–22697.

(124) Nelson, J. *The Physics of Solar Cells*; Published by Imperial College Press and distributed by World Scientific Publishing Co., 2003.

(125) Bisquert, J.; Fabregat-Santiago, F.; Mora-Seró, I.; Garcia-Belmonte, G.; Giménez, S. Electron Lifetime in Dye-Sensitized Solar Cells: Theory and Interpretation of Measurements. *J. Phys. Chem. C* **2009**, *113* (40), 17278–17290.

(126) Frank, A. J.; Kopidakis, N.; Lagemaat, J. Van De. Electrons in Nanostructured TiO2 Solar Cells: Transport, Recombination and Photovoltaic Properties. *Coord. Chem. Rev.* **2004**, *248* (13–14), 1165–1179.

(127) Bisquert, J.; Mora-Seró, I. Simulation of Steady-State Characteristics of Dye-Sensitized Solar Cells and the Interpretation of the Diffusion Length. *J. Phys. Chem. Lett.* **2010**, *1* (1), 450–456.

(128) Hegedus, S. S.; Shafarman, W. N. Thin-Film Solar Cells: Device Measurements and Analysis. *Prog. Photovoltaics Res. Appl.* **2004**, *12* (2–3), 155–176.

(129) Barnes, P. R. F.; Anderson, A. Y.; Juozapavicius, M.; Liu, L.; Li, X.; Palomares, E.; Forneli, A.; O'Regan, B. C. Factors Controlling Charge Recombination under Dark and Light Conditions in Dye Sensitised Solar Cells. *Phys. Chem. Chem. Phys.* **2011**, *13* (8), 3547–3558.

(130) Zhu, K.; Kopidakis, N.; Neale, N. R.; van de Lagemaat, J.; Frank, A. J.; Cells, S.; Zhu, K.; Kopidakis, N.; Neale, N. R.; Lagemaat, J. Van De; Frank, A. J. Influence of Surface Area on Charge Transport and Recombination in Dye-Sensitized TiO2 Solar Cells. *J. Phys. Chem. B* **2006**, *110* (50), 25174–25180.

(131) Li, F.; Jennings, J. R.; Wang, Q. Determination of Sensitizer Regeneration Efficiency in Dye-Sensitized Solar Cells. **2013**, No. 9, 8233–8242.

(132) Jennings, J. R.; Liu, Y.; Wang, Q. Efficiency Limitations in Dye-Sensitized Solar Cells Caused by Inefficient Sensitizer Regeneration. *J. Phys. Chem. C* **2011**, *115* (30), 15109–15120.

(133) Jennings, J. R.; Liu, Y.; Safari-Alamuti, F.; Wang, Q. Dependence of Dye-Sensitized Solar Cell Impedance on Photoelectrode Thickness. *J. Phys. Chem. C* **2012**, *116* (1), 1556–1562.

(134) Barnes, P. R. F.; Anderson, A. Y.; Durrant, J. R.; O'Regan, B. C. Simulation and Measurement of Complete Dye Sensitised Solar Cells: Including the Influence of Trapping, Electrolyte, Oxidised Dyes and Light Intensity on Steady State and Transient Device Behaviour. *Phys. Chem. Chem. Phys.* **2011**, *13* (13), 5798–5816.

(135) Gonzalez-Vazquez, J. P.; Morales-Flórez, V.; Anta, J. A. How Important Is Working with an Ordered

Electrode to Improve the Charge Collection Efficiency in Nanostructured Solar Cells? *J. Phys. Chem. Lett.* **2012**, *3*, 386–393.

(136) Liu, W.; Hu, L.; Dai, S.; Guo, L.; Jiang, N.; Kou, D. The Effect of the Series Resistance in Dye-Sensitized Solar Cells Explored by Electron Transport and Back Reaction Using Electrical and Optical Modulation Techniques. *Electrochim. Acta* **2010**, *55* (7), 2338–2343.

(137) Yang, W.; Söderberg, M.; Eriksson, A. I. K.; Boschloo, G. Efficient Aqueous Dye-Sensitized Solar Cell Electrolytes Based on a TEMPO/TEMPO + Redox Couple. *RSC Adv.* **2015**, *5* (34), 26706–26709.

(138) Idígoras, J.; Pelleja, L.; Palomares, E.; Anta, J. A. The Redox Pair Chemical Environment In Fl Uence on the Recombination Loss in Dye-Sensitized Solar Cells Jesu S. *J. Phys. Chem. C* **2014**, *118*, 3878–3889.